Observing the Unobservable by Inverting Solar Energetic Particle Events

JT Stevens

orcid.org 0000-0001-6120-7740

Dissertation accepted in partial fulfilment of the requirements for the degree *Master of Science in Astrophysical Sciences* at the North-West University

Supervisor: Prof RDT Strauss

Graduation : December 2023

"... when you are a Bear of Very Little Brain, and you Think of Things, you find sometimes that a Thing which seemed very Thingish inside you is quite different when it gets out into the open and has other people looking at it."

–Winnie the Pooh

The House at Pooh Corner by A.A. Milne, 1928

This dissertation is dedicated to my most significant other, Brad Lang, for his unfailing support from the very beginning.

Abstract

The mechanisms behind solar energetic particle (SEP) transport have been investigated for decades in the development of accurate and predictive space weather models. This dissertation investigates certain potential influences on the transport parameters that the SEPs experience within the inner heliosphere (< 1 AU). Inverting SEP events involves overlaying model simulations to existing observational data to an accurate fit; this process provides the transport parameters from the model as a result. To introduce the process of fitting model simulations to observational data, synthetic data are created and the best-fit results are found using the coefficient of determination (CoD) goodness-of-fit statistic. The one-dimensional (1D) transport model utilised in this project requires that observations of SEP events be recorded by instruments on magnetically well-connected spacecraft. By modelling the GLE#73 event of 28 October 2021, this process of finding observations for magnetically well-connected instruments is introduced. The final transport parameters are then investigated to find potential trends as well as compare them to previously determined estimates. It was found that the results presented in this project compared well with already defined trends, such as those presented by Dröge (2000), Engelbrecht and Moloto (2021), and Teufel and Schlickeiser (2002).

Keywords: solar energetic particles; focused transport equation; mean free path

Opsomming

Die prosesse wat die transport van energieke sondeeltjies (ESD's) beskryf is reeds vir dekades in die ontwikkeling van akkurate ruimteweervoorspellings bestudeer. In hierdie verhandeling word die potensiële invloed op die transportparameters van die ESD's in die binneste heliosfeer (< 1 AU) bestudeer. Die transportparameters van die model word bepaal deur modelsimulasies met bestaande ESD-waarnemings te vergelyk. Om hierdie proses te verduidelik word die bepalingskoëffisiënt-toets (BK) toegepas op sintetiese data om die beste-passingsresultate te vind. Die eendimensionele (1D) transportmodel wat in hierdie verhandeling gebruik word, benodig ESD-waarnemings van ruimtetuiginstrumente wat magneties goed gekoppel is. Hierdie proses word geillustreer deur die GLE#73-gebeurtenis van 28 Oktober 2021 te modelleer. Die finale transportparameters word dan ondersoek om moontlike tendense te vind, asook om dit met voorheen bepaalde beramings te vergelyk. Die resultate van hierdie verhandeling stem goed ooreen met die van Dröge (2000), Engelbrecht en Moloto (2021) en Teufel en Schlickeiser (2002).

Sleutelwoorde: energieke sondeeltjies; gefokusde transportvergelyking; vryeweglengte

Contents

Table of abbreviations

A list of abbreviations used in the text. When an abbreviation occurs for the first time in the text it is written out in full with the abbreviation given in brackets.

1D	One-Dimensional
AU	Astronomical Units
CME	Coronal Mass Ejection
CoD	Coefficient of Determination
DT	Damping Turbulence
FTE	Focused Transport Equation
GCR	Galactic Cosmic Ray
GLE	Ground Level Enhancement
GOES	Geostationary Operational Environmental Satellite
HMF	Heliospheric Magnetic Field
MFP	Mean Free Path
MeV	Mega electron Volts
MV	Mega Volts
NASA	National Aeronautics and Space Administration
NM	Neutron Monitor
NOAA	National Oceanic and Atmospheric Administration
PFU	Particle Flux Units
PSP	Parker Solar Probe
RS	Random Sweeping
SDO	Solar Dynamics Observatory
SEP	Solar Energetic Particle
SOHO	Solar and Heliospheric Observatory
Solar-MACH	Solar-MAgnetic Connection Haus
SolO	Solar Orbiter
STEREO	Solar TErrestrial RElations Observatory
SW	Solar Wind
UTC	Coordinated Universal Time
WIND	Global Geospace Science Wind Satellite

Chapter 1

Introduction

The inversion of solar energetic particle (SEP) events to obtain the so-called unobservable parameters for the event has been a topic of research for over half a century. Using the Roelof (1969) transport equation as a foundation for SEP transport models, this dissertation forms a guide to inverting SEP events by utilising a one-dimensional (1D) SEP propagation model and exploring any trends in the model parameter results.

Chapter 2 introduces the nature of SEPs and their transport through the inner heliosphere. It starts with a brief overview of the environment that SEPs propagate through and moves to the fundamental processes that occur. The chapter concludes with a brief discussion of the parameters involved in particle transport as well as the focused transport equation (FTE).

Chapter 3 presents the 1D SEP transport model by van den Berg et al. (2020) that utilises the FTE, as well as the Reid-Axford temporal profile as a source function. Using the coefficient of determination (CoD) goodness-of-fit statistic, this chapter guides the reader through the process of fitting the model to observational data using synthetic data.

Chapter 4 describes the procedure of finding relevant observational data that satisfy the requirements of the model as well as interpreting the outcome of the resulting best-fit parameter values. This procedure includes the use of JHelioviewer and Solar-MACH as tools to find information on the solar flare and the instruments in orbit at the time of the event.

Chapter 5 uses the results from fitting the model to more than a dozen events to probe multiple possible comparisons and connections of the best-fit free parameters. There is a focus on the rigidity dependence on the parallel MFP that is compared to previous historical and analytical estimates from Dröge (2000), Palmer (1982), and Teufel and Schlickeiser (2002).

Results from this work were presented at the South African Institute of Physics (SAIP) 67th annual conference and the SHINE 2023 Workshop[1].

---

[1] https://helioshine.org/

Chapter 2

Solar Energetic Particles

2.1 Introduction

In order to understand the nature of **s**olar **e**nergetic **p**articles (SEPs) and their transport, an understanding of their source and environment is necessary. This chapter first discusses the Sun and the heliosphere and focuses on the **h**eliospheric **m**agnetic **f**ield (HMF) that is generated by the Sun and extends to over 100 AU to the edge of the heliosphere. Section 2.3 provides a brief background of the history and variation of the different cosmic ray groups. A major differing factor between cosmic ray species is their acceleration mechanism. For SEPs this is then explored in Section 2.3.1 with a focus on solar flares.

The details involved in particle transport are then discussed in Section 2.4. Section 2.5 explores the transport equation for the model used in this project.

2.2 The Inner Heliosphere

At the centre of our solar system, the point around which the local neighbourhood of planets revolves, is the Sun. The Sun is a natural source of energy that sustains life on Earth and generates a protective bubble of solar plasma around the solar system (Prinsloo, 2016). This solar plasma forms a boundary when it interacts with interstellar plasma; within the boundary is the heliosphere (Strauss, 2013; Prinsloo, 2016) The heliosphere is a region of space defined by the Sun's magnetic field extent (Prinsloo, 2016; Wolmarans, 2021), more formally known as the Parker HMF.

The HMF reach extends over 15×10^9 km (122 AU), whereas Pluto, at the edge of the solar system, is only 6×10^9 km (40 AU) from the Sun. The preferred unit of measurement used in this project is the **a**stronomical **u**nit (AU) where 1 AU is the average distance between the Earth and the Sun (approximately 150×10^6 km). This project is only considering particle transport within the inner heliosphere, up to ~ 1 AU.

2.2.1 The Sun

By combining the total mass of the solar system, including the planets, moons, and asteroids, it is found that more than 99% of this mass is attributed to the Sun (Hanslmeier, 2002). This massive ball of plasma spins a full revolution on its own axis every ~ 24 days at the solar equator (Steyn, 2022). This increases to ~ 26 days when observing the time taken for one sunspot to rotate around the Sun before it reaches the same position as seen by an observer at Earth; this is called the synodic period (Steyn, 2022).

Sunspots are the most common indicator of solar activity, dating back to Carrington in the late 1800s, who first discovered that the Sun undergoes a somewhat routine rise and fall of solar activity every 11 years called the solar cycle (Steyn, 2022). This increased activity impacts properties such as the magnitude of the HMF, the solar wind speed, and the frequency of solar events (Engelbrecht and Moloto, 2021).

2.2.2 Solar Wind

The **s**olar **w**ind (SW) is a plasma that flows radially out from the Sun (Steyn, 2022). Due to its high electrical conductivity, it is the mechanism responsible for carrying the HMF into the heliosphere (Bruno and Carbone, 2016; Gurnett and Bhattacharjee, 2017). The SW speed (V_{sw}) is latitudinally dependent during solar minimum conditions where the speed at the solar equatorial belt is slow ($V_{sw} \approx 400$ km.s^{-1}), but from $\pm 30°$ to the poles, there is a drastic change in speed to much higher values ($V_{sw} \approx 800$ km.s^{-1}; McComas et al., 1998).

2.2.3 Parker Heliospheric Magnetic Field

The HMF originates at the Sun as the coronal magnetic field that gets dragged into the heliosphere, and, due to the rotation of the Sun, forms archimedean spirals (Steyn, 2022). The HMF, first modelled by Parker (1958a), is given in van den Berg et al. (2020) as

$$\mathbf{B}_{\mathrm{HMF}} = A\, B_0 \left(\frac{r_0}{r}\right)^2 \left(\hat{\mathbf{r}} - \tan\psi\, \hat{\boldsymbol{\phi}}\right), \tag{2.1}$$

where $A = \pm 1$ is the magnetic field polarity, r is the radial distance, B_0 is a normalisation constant (which is often given as the HMF magnitude at Earth, $B_\oplus = 5$ nT, at $r_0 = 1$ AU), ψ is the winding angle, and the unit vectors $\hat{\mathbf{r}}$ and $\hat{\boldsymbol{\phi}}$ label the radial and azimuthal directions, respectively.

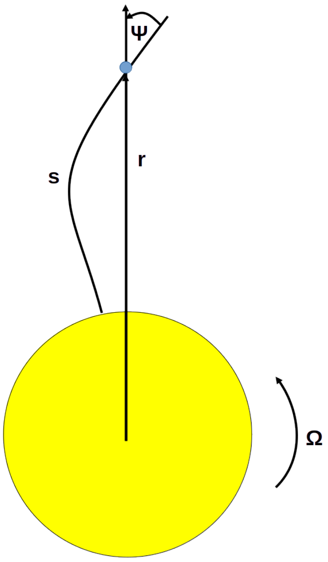

Figure 2.1: A diagram of the inner heliosphere looking from the north pole of the Sun, where the yellow circle indicates the Sun, to illustrate the winding angle ψ between the magnetic field vector and radial vector. Note that the solar equatorial rotation Ω shows in which direction the Sun is spinning on its axis.

The winding angle is seen in Figure 2.1 as the angle between the magnetic field vector and the radial vector. The equation for this is given in Steyn (2022) as

$$\psi(r) = \arctan\left(-\frac{B_\phi}{B_r}\right) \approx \arctan\left(\frac{\Omega\, r}{V_{sw}}\right), \tag{2.2}$$

where $\Omega = 10.3 \times 10^{-3}$ rad.hr^{-1} is the solar equatorial rotation rate, and the V_{sw} is assumed to be 400 km.s^{-1} or 9.6×10^{-3} AU.hr^{-1} on average. The first panel in Figure 2.2 displays how the winding angle changes as a function of increasing radial distance from the Sun for a range of solar wind speed values.

2.2.3.1 Parker Length

The distance from the Sun can be defined as either the radial distance or as the arc length along the Parker spiral (s), seen in Figure 2.1. The calculation for the Parker length s is given in van den Berg et al. (2020) as

$$s = \int \sqrt{1 + \tan^2 \psi}\, \mathrm{d}r. \tag{2.3}$$

When calculating 1D particle transport in the heliosphere, transport along the Parker spiral is used. To gauge the difference between the radial distance and the Parker length, the distance from the Sun to Earth along the spiral is $s = 1.2$ AU for an average value of $V_{sw} = 400$ km.s^{-1}. The third panel in Figure 2.2 shows how s increases as a function of the radial distance.

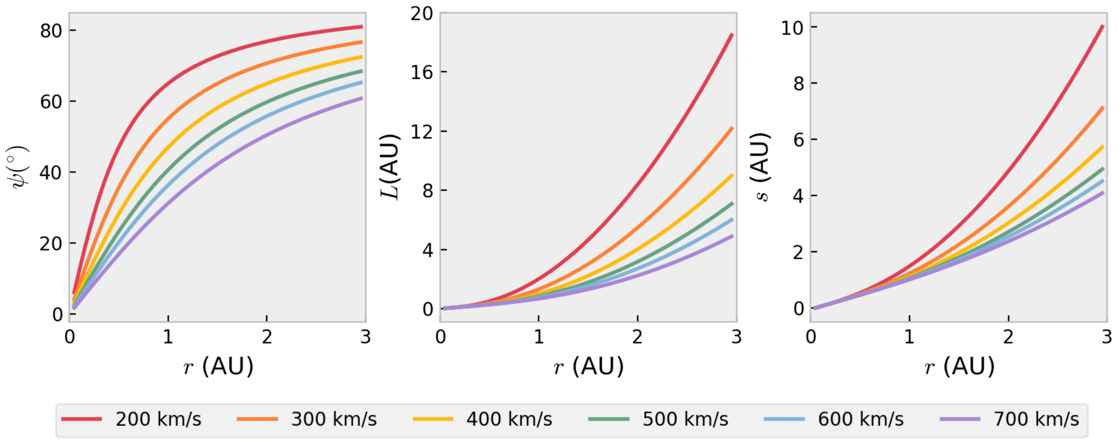

Figure 2.2: Winding angle (ψ), magnetic focusing length (L), and Parker length (s) as a function of increasing radial distance, with different solar wind speeds to illustrate their effects.

2.3 Solar Cosmic Rays

Solar **e**nergetic **p**articles (SEPs) were initially called solar cosmic rays alongside their cosmic ray siblings: **g**alactic **c**osmic **r**ays (GCRs) and **a**nomalous **c**osmic **r**ays (ACRs). Cosmic rays are grouped by defining characteristics such as their origin or acceleration mechanism (Steyn, 2022). GCRs have galactic origins from outside the heliosphere, ACRs are accelerated at the termination shock, and SEPs are accelerated by solar events at the Sun (Steyn, 2022).

Solar particles were first discovered by Forbush (1946) when studying cosmic ray intensities on Earth's surface. Forbush recorded three sudden, distinct increases in cosmic ray intensity that aligned to similar times for solar events. This form of radiation can be highly volatile in large enough doses. The Earth's magnetosphere offers some protection, redirecting most of the energy to the poles where the aurora is formed as a result (Cravens, 2004). However, the closer to ground level the more protection is offered, leading to aviation workers such as aircraft pilots to also be referred to as radiation workers due to the increased radiation experienced at higher altitudes (Mosotho et al., 2021).

2.3.1 Solar Events

Parker (1958b) states that SEPs are only ever emitted by the Sun if there is a **c**oronal **m**ass **e**jection (CME) or solar flare. These particles can be studied through direct measurements by remote instruments such as X-ray telescopes, radio imagery, and particle detectors (Dröge, 1996). SEP events are described as either gradual or impulsive, where gradual events are said to be accelerated by CMEs and impulsive events by solar flares (Reames, 1999; Strauss et al., 2020). The terms impulsive and gradual describe the length of time for particle observations to reach the maximum flux. However, they originally describe the time scales of the X-ray observations (Reames, 1999). Gradual events imply that there is a continuous particle acceleration (Reames, 1999), while impulsive events are described as an injection of particles into the inner heliosphere. This project works with SEPs accelerated exclusively by impulsive solar events.

2.3.1.1 Solar Flares

Solar flares are produced in active regions or sunspots which occur on the layer of the Sun called the chromosphere. This layer is only visible to the naked eye on Earth during a solar eclipse (Sakurai, 1974). Flares occur when the magnetic field on the surface of the Sun has stored large amounts of energy and is released when the field lines break and reconnect to different field lines instantaneously leading to the process of magnetic reconnection (Steinacker et al., 1988).

2.3.1.2 Active Regions and Sunspots

Sunspots are cool, dark regions located within 30° of the solar equator and occur within bright active regions (Steyn, 2022). The darkness of the sunspots is attributed to the much higher magnetic flux compared to its surrounding regions (Steyn, 2022), which increases in intensity until the solar flare releases the trapped energy. The solar cycle was discovered in the 1800s when studying the trend of sunspot numbers over time; this trend is seen in the figures of Section 5.2.

2.3.2 Ground Level Enhancements

A **g**round **l**evel **e**nhancement (GLE) event occurs when a solar event erupts with enough energy that the particles can travel to Earth, through the Earth's atmosphere, and reach the ground-level instruments distributed across the planet known as **n**eutron **m**onitors (NMs). The minimum energy required for this process is, in terms of rigidity (see Equation 2.5), called the cut-off rigidity. At the Earth's equator, this value is P_c = 17 GV and at the Earth's poles, it is P_c = 1 GV (Moraal, 2013). Once the particles reach the atmosphere they start to break down into more fundamental particles, such as neutrinos and bosons, this is a process called a cosmic-ray shower. GLE events are so rare that there are only 73 recorded at the time of writing, the most recent event at the time of writing occurred on 28 October 2021 and is discussed in Chapter 4.

2.4 Solar Particle Transport

2.4.1 Particle Velocity

To calculate the particle speed in terms of the rest mass energy, the equation from Steyn (2022) can be rewritten such that

$$v = \frac{P\,c}{E_k + E_0}, \tag{2.4}$$

where $c = 7.2$ AU.hr^{-1} is the speed of light, E_k is the particle's kinetic energy in MeV, E_0 is the particle's rest mass energy ($E_{0,e} = 0.51$ MeV for electrons and $E_{0,p} = 938$ MeV for protons), and P is the particle rigidity in MV.

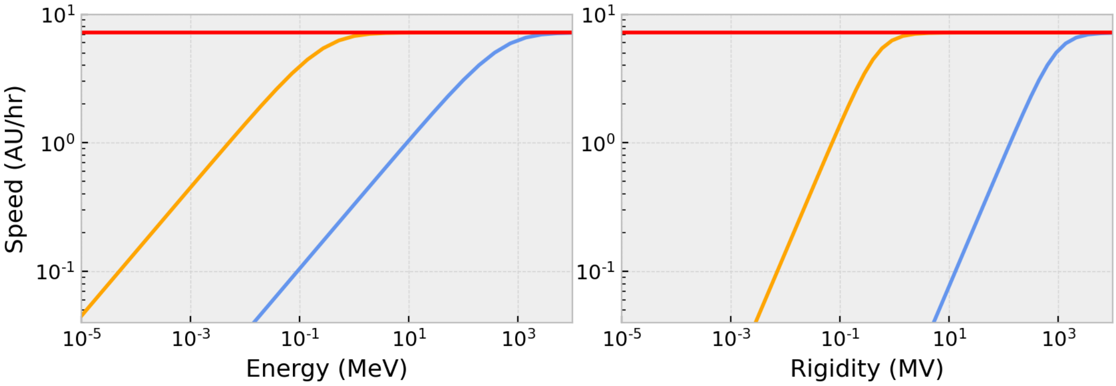

Figure 2.3: The speed of electrons (orange) and protons (blue) over a range of energies (left panel) and rigidities (right panel) compared to the speed of light. This graph was plotted using equation 2.4. This shows that electrons are faster at lower energy and rigidity values compared to heavy protons. The speed of light is indicated by the horizontal red line. This figure is recreated from Steyn (2022) and changed to a log scaling on both axes.

SEPs are grouped into electrons and protons when studying their transport due to the differences in their rest mass energy and thus their speed. The first panel of Figure 2.3 shows that as the energy increases for electrons (orange line), they quickly become relativistic by moving close to the speed of light (red line) before their energy reaches 10 MeV, while the protons (blue line) only become relativistic after 10000 MeV. The particle rigidity is a preferred means of considering energy-like comparisons for both electrons and protons as, at the same rigidity, both particles have the same Larmor radius. The relation for particle rigidity in terms of the kinetic and rest mass energy is

$$P \approx \sqrt{E_k(E_k + 2E_0)}. \tag{2.5}$$

The second panel in Figure 2.3 shows the particle speed with increasing rigidity values. The same trend for each particle species is seen where the speed of electrons increases and reaches relativistic speeds first, and then the protons increase. The comparison between energy and rigidity in Figure 2.3 shows that there are minor differences when converting to rigidity.

2.4.2 Pitch-Angle

A particle moving through a magnetic field will gyrate around its guiding centre, which indicates the average direction of motion of the particle. The guiding centre should follow the path of the magnetic field line. The angle between the guiding centre's direction of motion and the magnetic field direction is the pitch-angle, the relation for which is given in van den Berg et al. (2020) as

$$\alpha = \arctan\left(\frac{\mathbf{v}\cdot\mathbf{B_0}}{vB_0}\right), \tag{2.6}$$

where $\mu = \cos\alpha$ is the pitch-cosine. Particles propagating away from the Sun will have $\mu \approx 1$ and towards the Sun will have $\mu \approx -1$ (Strauss et al., 2020). The change in pitch-cosine due to diverging or contracting field lines (i.e. focusing or mirroring) is further defined by van den Berg et al. (2020) as

$$\frac{\mathrm{d}\mu}{\mathrm{d}t} = \frac{(1-\mu^2)v}{2L(s)}, \tag{2.7}$$

where

$$\frac{1}{L(s)} = -\frac{1}{B(s)}\frac{\mathrm{d}B(s)}{\mathrm{d}s} \tag{2.8}$$

denotes the magnetic focusing length in one **d**imension (1D) as a function of the magnetic field gradient. This can be rewritten in terms of the winding angle as

$$L = \frac{r\left(1+\tan^2\psi\right)^{3/2}}{2+\tan^2\psi}. \tag{2.9}$$

To understand how L changes with increasing rigidity, the second panel of Figure 2.2 displays how it remains similar for a range of solar wind values up to 1 AU whereafter it starts increasing exponentially.

2.4.3 Mean Free Path

The **m**ean **f**ree **p**ath (MFP) of a particle is described by van den Berg et al. (2020) as the average distance moved by a particle in between collisions or interactions. Following the transport of SEPs along the HMF line requires a focus on the parallel propagating MFP in particular. This is further defined by van den Berg et al. (2020) and Hasselmann and Wibberenz (1968) to be the distance travelled by a particle in a turbulent plasma before the velocity is no longer determined by its initial velocity from interactions with pitch-angle scattering. This is a measure of the scattering strength for SEP transport. The parallel MFP is derived by Hasselmann and Wibberenz (1968) and given in Kallenrode (1995) as a function of changing pitch-angle,

$$\lambda_{\parallel} = \frac{3}{8} v \int_{-1}^{+1} \frac{(1-\mu^2)^2}{D_{\mu\mu}(\mu)} \mathrm{d}\mu, \tag{2.10}$$

where $D_{\mu\mu}$ is the pitch-angle diffusion coefficient. The MFP is not a quantity that can be observed or measured, it can be studied theoretically or found through inverting SEP event observations with transport models to find the best MFP value to fit the observation profile. This is the first unobservable parameter that is studied in this project.

2.5 Focused Transport Equation

The SEP transport model used in this project utilises a **f**ocused **t**ransport **e**quation (FTE) to model 1D particle propagation. SEP transport is influenced by many mechanisms and processes in the inner heliosphere that Ruffolo (1995) compacted into a comprehensive 1D transport equation using the Fokker-Planck equation. This comprehensive equation is broken down such that

$$\begin{aligned}
\frac{\partial f}{\partial t} = &- \frac{\partial}{\partial s}\mu v f && \text{(streaming)} \\
&- \frac{\partial}{\partial s}\left(1 - \mu^2 \frac{v^2}{c^2}\right) V_{sw} \sec\psi f && \text{(convection)} \\
&- \frac{\partial}{\partial \mu}\frac{v}{2L(s)}\left[1 + \mu\frac{V_{sw}}{v}\sec\psi - \mu\frac{V_{sw}\, v}{c^2}\sec\psi\right](1-\mu^2) f && \text{(focusing)} \\
&+ \frac{\partial}{\partial \mu} V_{sw}\left(\cos\psi \frac{\mathrm{d}}{\mathrm{d}r}\sec\psi\right)\mu(1-\mu^2) f && \text{(differential convection)} \\
&+ \frac{\partial}{\partial \mu} D_{\mu\mu}\frac{\partial}{\partial \mu}\left(1 - \mu\frac{V_{sw}\, v}{c^2}\sec\psi\right) f && \text{(scattering)} \\
&+ \frac{\partial}{\partial p} p\, V_{sw}\left[\frac{\sec\psi}{2L(s)}(1-\mu^2) + \cos\psi\frac{\mathrm{d}}{\mathrm{d}r}(\sec\psi)\mu^2\right] f, && \text{(deceleration)}
\end{aligned}$$

where $f = f(t, \mu, s, p)$ is the distribution function and t is the time. It is assumed that SEPs have a high enough velocity ($v \gg V_{sw}$) due to their high energies that the solar wind speed can be made redundant in terms of calculating the FTE (Heita, 2019). After neglecting any terms with V_{sw}, the equation now becomes that which was derived by Roelof (1969), which no longer includes advection or energy loss (van den Berg et al., 2020),

$$\frac{\partial f}{\partial t} + \frac{\partial}{\partial s}(\mu v f) + \frac{\partial}{\partial \mu}\left(\frac{(1-\mu^2)\, v}{2L(s)} f\right) = \frac{\partial}{\partial \mu}\left(D_{\mu\mu}\frac{\partial f}{\partial \mu}\right). \tag{2.11}$$

The focusing length seen in the third term still requires V_{sw} to compute so this is set to an average of $V_{sw} = 400$ km.s^{-1}.

2.5.1 Omni-directional Intensity

Using the distribution function f from Equation 2.11, the omni-directional distribution function can be found using

$$F(s,t) = \frac{\int_{-1}^{+1} f(s,\mu,t)\mathrm{d}\mu}{\int_{-1}^{+1} \mathrm{d}\mu} = \frac{1}{2}\int_{-1}^{+1} f(s,\mu,t)\mathrm{d}\mu, \tag{2.12}$$

where F is the omni-directional distribution function. This function is then directly proportional to the particle intensity at a fixed energy. Observed particle intensities are measured in **p**article **f**lux **u**nits (PFU) which is the number of particles/(sr.cm^2.s.MeV)$^{-1}$ as seen in Chapters 3 and 4 (Strauss et al., 2022).

2.5.2 Anisotropy

Isotropy is when there is uniformity in all directions; thus anisotropy is either when there is uniformity in only one direction or when there is no uniformity at all. For example, a nett streaming of particles along the HMF. Diffusion in SEPs was first noticed to be anisotropic during the 1960s when Reid (1964) described that solar particles are anisotropic at the early stages of SEP events but not as the event evolves back down to an isotropic state due to a system involving a tube of force, seen in Figure 2.4.

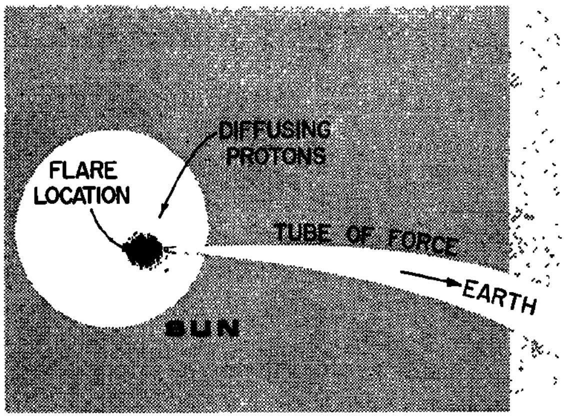

Figure 2.4: Configuration of the tube of force described and taken from Reid (1964). The tube follows the path of the magnetic field line from the flare on the surface of the Sun to Earth.

This high anisotropy in the early stage of SEP events is due to the observer (being some distance away and along the magnetic field) only being able to observe particles travelling from the Sun. After particles have travelled past the observer, some can be scattered back towards the Sun. The observer would now detect particles moving in both directions (towards and away from the Sun). This would indicate a more isotropic phase of the event.

The anisotropy can be calculated over time using the formal definition,

$$An(r,\phi,t) = 3\frac{\int_{-1}^{+1}\mu f(s,\mu,t)\mathrm{d}\mu}{\int_{-1}^{+1} f(s,\mu,t)\mathrm{d}\mu}, \tag{2.13}$$

which falls within −3 and +3 (Strauss et al., 2022). This is the first-order anisotropy, which indicates if the particles are travelling in the direction of the Sun (negative) or away from the Sun (positive). When $An \approx 0$ then the particle's transport has become isotropic again.

2.6 Summary and Conclusion

Chapter 2 introduces a brief understanding of the characteristics of SEPs and their transport as well as the environment they travel through. It starts with a discussion regarding the inner heliosphere and how it is formed by the magnetic field generated by the Sun, before exploring what solar cosmic rays are and how they are accelerated. Focusing on the particles themselves, Section 2.4 describes the equations necessary for modelling their transport through the heliosphere. The chapter concludes with the FTE that is used in the 1D particle propagator model for this dissertation.

Chapter 3

Solar Energetic Particle Transport Model

3.1 Introduction

This chapter introduces the focused transport model by van den Berg et al. (2020), which will be compared to SEP observations, and the goodness-of-fit test that is necessary to determine if the model fits the observations, before creating synthetic data to test the method against. Section 3.2 explores solutions of the 1D SEP transport model using the input parameters discussed in Chapter 2, including the injection function originally derived by Reid (1964) that provides the initial particle flux. The next section will then discuss the model assumptions and the three free parameters that the model utilises. These free parameters adjust the shape of the flux profile to fit the observations. A goodness-of-fit test is then required to quantify that the model fits the data accurately. Section 3.4 will delve into the **c**oefficient **o**f **d**etermination (CoD) test and how it is used. Thereafter, synthetic data are created in Section 3.5 to test the process of finding the best-fit values and interpreting the results.

3.2 One-Dimensional Transport Model

Section 2.5 introduces the FTE, derived by Roelof (1969), which is the foundation for the numerical model used in this project. The 'SEP Propagator'[1] is a 1D SEP transport model that is designed using Fortran90. The transport being modelled in only one spatial dimension restricts the observations to only well-connected measurements, assuming that SEPs follow the Parker magnetic field lines discussed in Section 2.2.3.

---

[1] https://github.com/RDStrauss/SEP_propagator

The model reads in a set of event parameters as well as free parameters, discussed in Section 3.3.1, which are the unobservable characteristics that can not be measured for a SEP event. The event parameters are gathered from the observational data that is being compared to, including the particle's kinetic energy (in MeV), which species (either electrons or protons) is considered, the radial position (in AU) that the instrument is from the Sun, the total time (in hours) the simulation is computed for, the solar wind speed (in km.s^{-1}), and the 'injection switch'. There are two options for the injection function, namely the delta function and Reid-Axford injections; this project only utilised the latter.

A few adjustments are made to the publically available version of the model; they are to the minute counter, the background flux intensity, and the spatial dependence of the parallel mean free path. The minute counter that prints out the decimal time of the simulation each minute, is updated such that the time does not reset to zero after every output is printed; instead it reduces the printed time by a minute value with up to 25 decimals to be accurate. Before this adjustment is made, a very slight difference in the model outcome is noticed concerning the number of data points that are returned, the impact is small but significant due to numerical truncation in the model.

The background flux intensity, originally set to $F = 1{\times}10^{-4}$ PFU, is changed to $F = 1{\times}10^{-12}$ PFU because some of the data sets (specifically from the WIND-3DP instrument) provided flux intensities as low as $F = 1 \times 10^{-11}$ PFU. By making sure the model background flux is always lower than the observed values, it makes it possible to renormalise the model data without impacting the profile.

The Fortran code is set to find the radial MFP λ_r, which is related to the parallel MFP through the winding angle. Dröge et al. (1997) defines the relation as

$$\lambda_r = \lambda_{\parallel} \cos^2 \psi, \tag{3.1}$$

where either the radial or parallel component of the MFP is kept spatially constant.

To avoid this extra step, the $\cos^2 \psi$ term, seen in Equation 3.1, is removed from the $D_{\mu\mu}$ calculation in the code and the parallel MFP is assumed to be spatially constant.

3.2.1 Reid-Axford Temporal Profile

To account for the early stage of SEP events being highly anisotropic and then gradually reducing back to an isotropic state, time-dependent injection functions are derived that explain the anisotropy while also explaining the flux time profiles (Reid, 1964). The injection function used in this project is the Reid-Axford temporal profile originally derived by Reid (1964) and built on by Axford (1965). It is used as the time-dependent boundary condition, specified at the model's inner boundary. The Reid-Axford profile is given by

Dröge (2000) as

$$f_0(s = s_0, t) = \frac{C}{t} \exp\left[-\frac{\tau_a}{t} - \frac{t}{\tau_e}\right], \tag{3.2}$$

where the distribution function f_0 is a function of time t at the inner boundary where $s = s_0$, τ_a and τ_e are the acceleration and escape times of the particles, and C is a constant used to normalise the profile (van den Berg et al., 2020; Dröge, 2000; Reid, 1964; Axford, 1965).

The acceleration and escape times are denoted by Dröge (2003) as rise and decay timescales and originally described the diffusion of particles from the flare to the tube of force (discussed in Section 2.5.2) and escaping out of the tube later. The current mathematical definition for the time-dependent injection is understood to be a more generic injection process that shows the steep increase to the peak and then a monotonic decay (Dröge, 2003).

For more information on the physics involved in this time profile, Burlaga (1967) breaks down the models from both Reid (1964) and Axford (1965) to understand why they are merged into one. The original temporal profile from Reid (1964) is given as

$$U = \frac{N}{4\pi a^2 t} \exp\left\{\frac{-\rho^2}{4a^2 t} - kt\right\}, \tag{3.3}$$

where U is the surface density of particles on the Sun at a distance ρ from the flare, N is the number of particles, $a^2 = \frac{1}{3}v\lambda$ is a diffusion constant that is dependent on the particle velocity and MFP, and k is the fraction of particles lost over time. The loss term k relates to the escape time τ_e but the acceleration time appears to be a combination of the particle's velocity and an initial MFP with respect to the distance from the flare that the magnetic footprint of the instrument lies on. From the original relation to the version commonly used now, variables have been reduced without any clear explanation of where those variables went; the belief must be that they are simplified to be contained within both τ_a and C.

3.3 Model Assumptions

The model is only able to simulate SEP transport along Parker HMF lines, thus neglecting cross-field transport. Observations that follow this restriction that the flare must be magnetically well-connected to the receiving instrument, are discussed in Section 4.2.1. This project assumes a constant average solar wind speed of $V_{sw} = 400$ km.s^{-1} for all model results and calculations.

3.3.1 Free Model Parameters

The model is run using parameters that are determined by the event and need to be found beforehand, such as the kinetic energy of the particles and the radial distance of the instrument under consideration. However, some parameters cannot be measured or observed; these are the unobservable values or unobservables. The unobservables still pertain to the event and describe the particle transport. These are found by simulating enough combinations of free parameter values. The best-fit values should be the values describing that specific event or the environment in which the event occurs. Chapter 5 discusses some insights into these results and how they could potentially describe the event or environment around them.

To understand the impact that each free parameter has on the flux time profile, Figures 3.1 and 3.2 are designed using a baseline set of parameter values; $\lambda_{\parallel}$ = 0.5 AU, τ_a = 0.1 hrs, and τ_e = 1.0 hrs for both electrons and protons. Simulations are shown at a radial distance of 1.0 AU, kinetic energy of E_k = 0.1 MeV for electrons and E_k = 10.0 MeV for protons.

The first panel in the electron parameter guideline shows an unchanging flux profile at the Sun due to the MFP not having any involvement in the injection of particles (seen in Equation 3.2). However, panel two in the top row illustrates that changing the acceleration time adjusts the height and sharpness of the distribution at the peak and the slope of the onset, while panel three mostly demonstrates a change in the declining slope for the changing escape time.

This impact for τ_a appears to carry through into the row below where the magnitude of the peak and slope of the onset are the major changing factors, where lower values of τ_a lead to a sharper peak and higher intensity. Changing the value of τ_e at 1.0 AU leads to a change in the distribution around the peak where lower escape time values create a sharper peak. This almost indicates that the injection at the Sun defines the profile up to a point around the peak in terms of the escape time.

The changing $\lambda_{\parallel}$ values indicate that smaller values lead to a smaller profile decay slope. This panel also shows that there are limitations to the model such that it is unable to produce simulation values when using the lowest and highest MFP values ($\lambda_{\parallel}$ = 0.01 and 7.0 AU). This is even seen for the anisotropy in the bottom row; this plot should always show a sharp peak with an exponential function decreasing to zero. For the four extreme values it is not plotted at all after a certain point or never approaching zero.

The proton simulations need to run for a longer period compared to electrons because protons are heavier and slower at the energies considered. The same profile will be seen with protons just more stretched out over time than electrons.

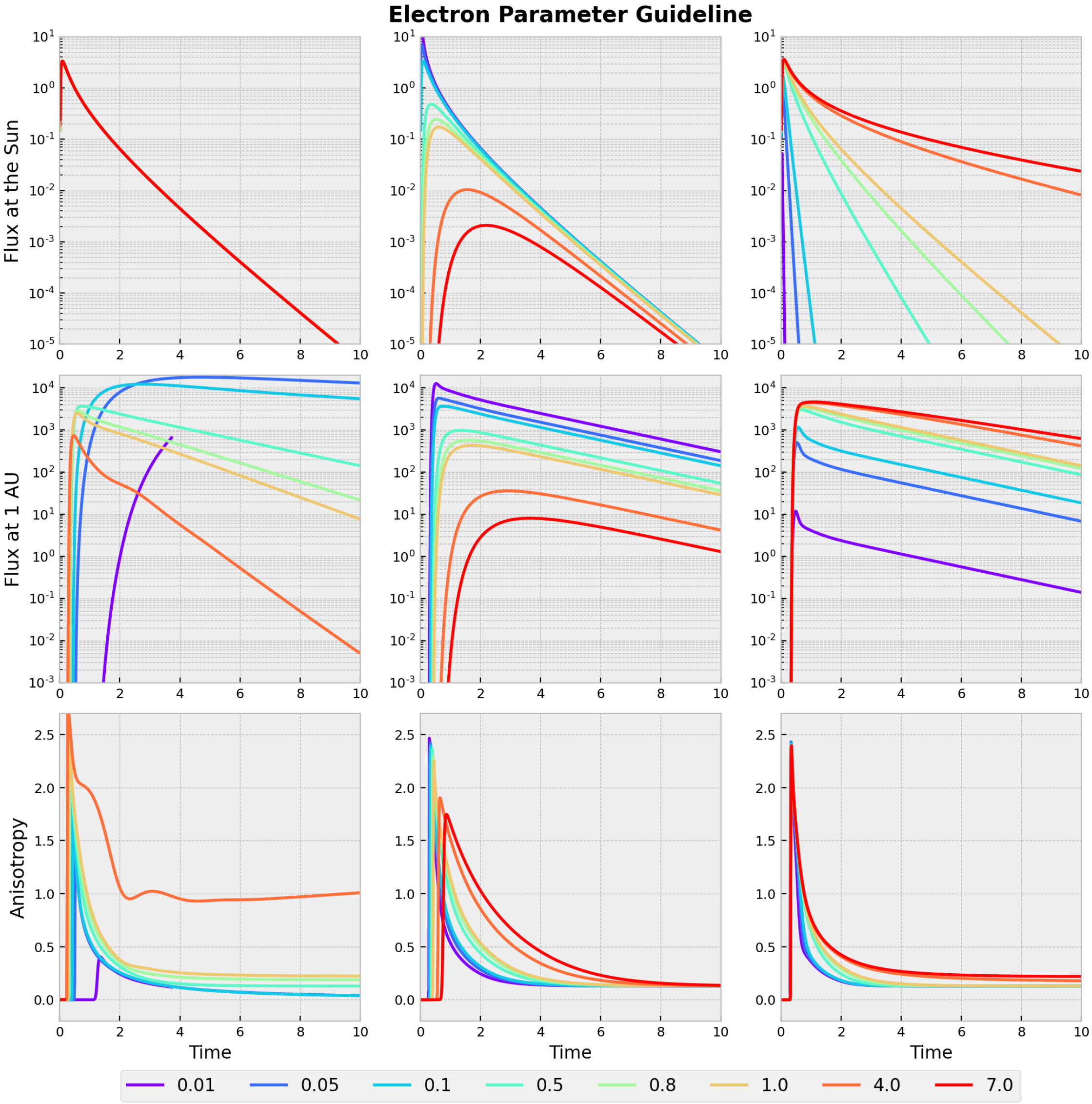

Figure 3.1: The electron free parameter guide shows how the time profile reacts to changing the values for the parallel MFP (left column), acceleration time (centre column), and escape time (right column). To show how the model changes when changing each parameter, the other two (unchanging parameters) are kept at the following values: $\lambda_\parallel = 0.5$ AU; $\tau_a = 0.1$ hrs, and $\tau_e = 1.0$ hrs. The legend below the figure indicates the array of values tried for all three parameters, where the units for $\lambda_\parallel$, τ_a and τ_e are AU, hours, and hours, respectively. The top row displays the intensity at the Sun in arbitrary units, calculated using the Reid-Axford time profile in equation 3.2. The middle row displays the flux intensity in arbitrary units at 1.0 AU from the model and the bottom row displays the anisotropy at 1.0 AU from the model output.

There are some similarities between the electron and proton parameter guides; the most notable difference being the onset time for protons is much later.

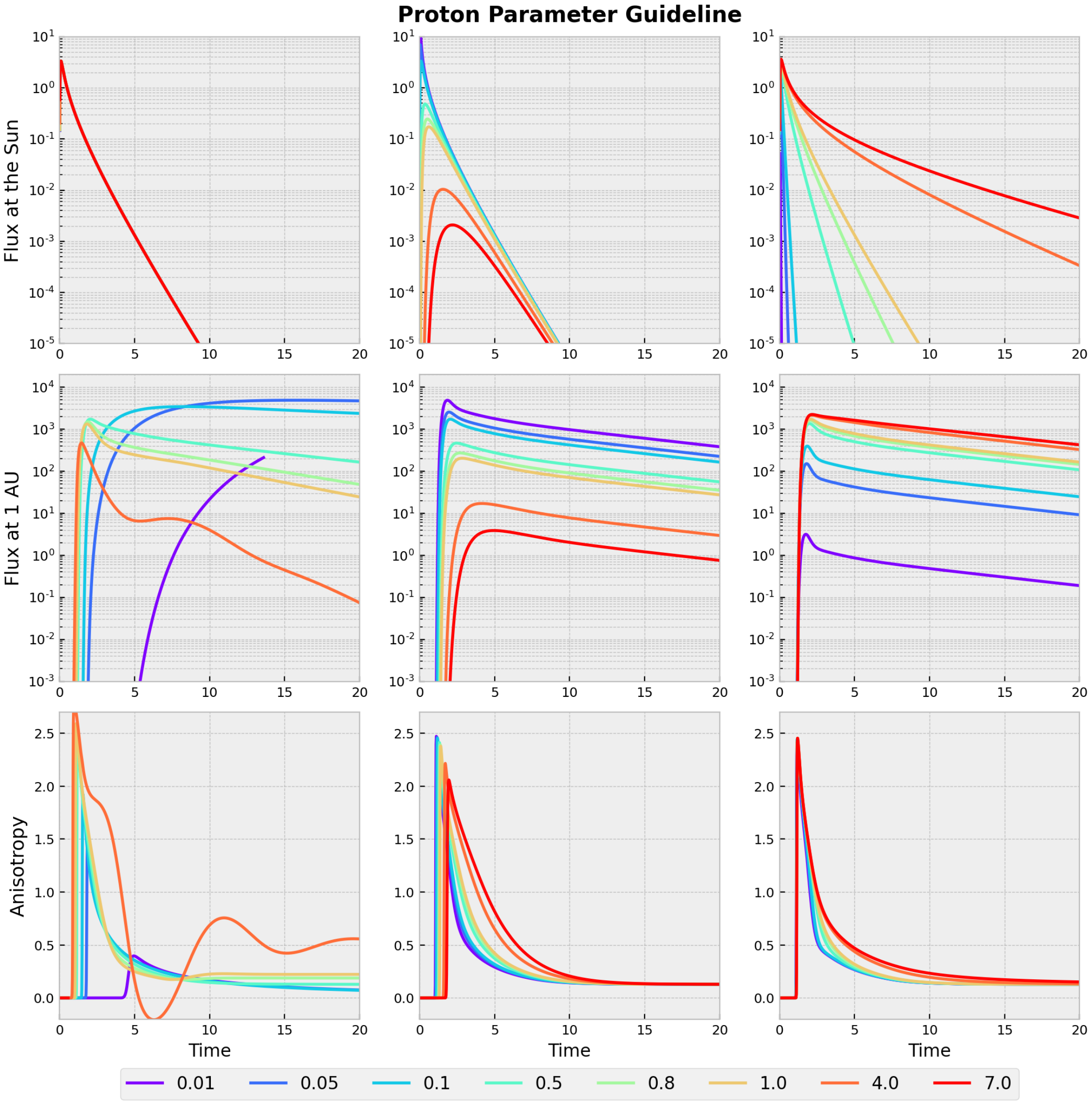

Figure 3.2: Proton free parameter guide showing how the time profile reacts to changing the free model parameters. The figure follows the same layout and structure as Figure 3.1.

The results related to the extreme values of the MFP are again in the proton guideline displaying limits to the values with which it can produce simulations where the profile for 0.01 AU is cut off early and 7.0 AU is not displayed at all; bordering these limits is 4.0 AU which displays an irregular shape for the flux and anisotropy. The Reid-Axford parameters display the same changes as seen in the electron parameter guide.

These guides are a useful tool when fitting events to aid the user to find the best values faster, i.e. if the slope needs to be steeper than the model is currently outputting, then it is easy to see that the mean free path needs to be increased.

3.3.2 Normalisation

The fourth free value that can be openly adjusted, yet is not formally defined to have any physical meaning outside of being a simple scaling factor, is the normalisation constant C in the Reid-Axford model. This value allows the model's output intensity to be directly shifted up or down without impacting any profile or physical understanding. This is simply done by finding the average peak height of the observation and dividing it by the average peak height of the model to get C. The normalised model is then calculated by multiplying the model output by C.

3.4 Goodness-of-Fit Testing

Achen (1982) poses the question "How can a good fit be recognized?". A statistic, first mentioned by Wright (1921) when trying to predict the weight of guinea pigs, is the R^2 goodness-of-fit statistic, formally known as the **c**oefficient **o**f **d**etermination (CoD). This is a regression analysis tool that is used when trying to confirm if a predictive model compares well to observations.

3.4.1 Coefficient of Determination

The CoD statistic is simply defined by Achen (1982) as the fraction of explained variance over the total variance. This is defined by Berry and Feldman (1985) to be

$$R^2 = 1 - \left(\frac{\sum_{j=1}^{n} \left(Y_j - \hat{Y}_j \right)^2}{\sum_{j=1}^{n} \left(Y_j - \bar{Y} \right)^2} \right), \tag{3.4}$$

where the observations are denoted by Y_j for j number of observations, $\hat{Y}_j$ is the estimated or predicted values, and $\bar{Y}$ is the average value of the observations. The resulting value for a good fit for R^2 should lie between 0.0 and 1.0. If it is negative then it implies that the two sets are completely mismatched. If the model can include all the potential impacts of the SEPs' transport, then the CoD must equal 1.0 or unity (Wright, 1921). However, the real world is far from ideal and there will always be unaccounted-for disturbances, which is why Achen (1982) describes it as "the percentage of variance explained". This statistic will come in use later in Sections 3.5.3 and 4.3.3 where the remainder of the variance that is unexplained will be hypothesised.

3.4.2 Implementation

To better understand how this analysis is used in this project, Equation 3.4 is broken up into three parts. The most crucial part is the sum of squares of the residuals,

$$SS_{res} = \sum_{j=1}^{n} \left(Y_j - \hat{Y}_j\right)^2, \tag{3.5}$$

because if $Y_j - \hat{Y}_j = 0$ for all the items j, then the two sets of data are perfectly in sync (Berry and Feldman, 1985). To bring Equation 3.5 into a relative space that can be compared more generally, it must be divided by the total sum of squares

$$SS_{tot} = \sum_{j=1}^{n} \left(Y_j - \bar{Y}\right)^2. \tag{3.6}$$

Lastly, by subtracting this value from one, the CoD is found as

$$R^2 = 1 - \frac{SS_{res}}{SS_{tot}}, \tag{3.7}$$

to turn the fraction of the two equations into a "rhetorical" percentage, as Achen (1982) calls it and provides a route to find the best possible fitting simulation for the model.

Fortunately, there exists a Python module called `scikit-learn` (Pedregosa et al., 2011) that includes the `r2_score(obs, mod)` function that performs this calculation when it is supplied with the observation (`obs`) and model (`mod`) data sets. For the function to work both sets must be of equal length and (in the version used in this project) no values can be `NaN` or infinite.

3.5 Synthetic Data Testing

To understand how the model functions and to show how the model will be compared to observations, a single set of synthetic data is generated and, using the goodness-of-fit test alongside the free parameter guideline, the synthetic data is thereafter fitted and analysed.

3.5.1 Generating Synthetic Data

Using the Fortran code with the changes mentioned in Section 3.2 a single instance is run for an electron event with a kinetic energy of 0.1 MeV, set to a distance 1.0 AU radially away from the Sun, using a time-dependent injection, with the free parameters set to $\lambda_{\parallel}$ = 0.5 AU, τ_a = 0.1 hrs, and τ_e = 0.8 hrs. The model values are then adjusted by adding 0.1 PFU to every flux value so that the background data are not at the very low value of $F = 1 \times 10^{-11}$ PFU, making it more reasonable and relatable to real observed data.

3.5.2 Introducing Noise

The synthetic data still look like a single continuous line, which is unrealistic, so noise is required as a final step in creating the data set. To do this the `random.gauss(x, sigma)` Python function (Van Rossum, 2020) is utilised where `x` is a single flux value and `sigma` is the maximum standard deviation σ that it will adjust the values by. This function creates pseudo-random values using $x' = x + x\sigma$, where x' is the randomly adjusted value, x is the original value, and σ is the maximum standard deviation.

For this data set the flux deviation is set to $\sigma_{\text{flux}} = 0.35$ and the anisotropy deviation is $\sigma_{\text{anisotropy}} = 0.2$. The original and final synthetic data sets are shown in Figure 3.3 in orange and black, respectively.

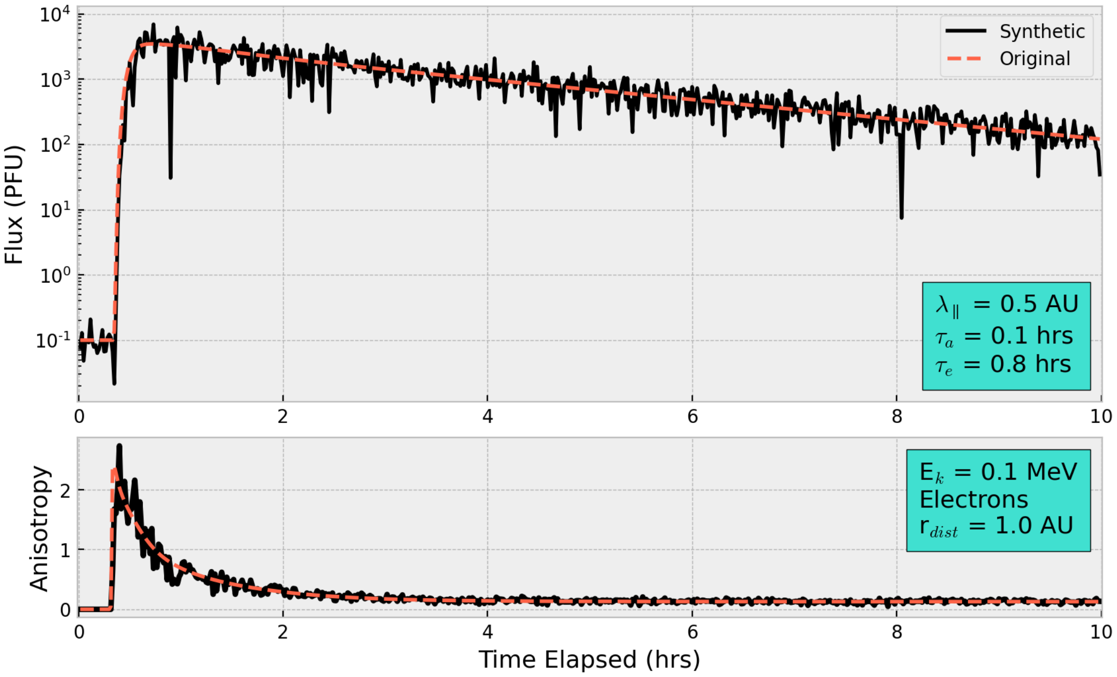

Figure 3.3: Synthetic data created from the 1D SEP transport model. The orange dashed line indicates the original values drawn from the model which are then adjusted to get the black noisy synthetic data.

The resulting synthetic data still clearly follow the original time profile with the noise skewing the profile downwards around the first and eighth hours. Due to the logarithmic scaling that this is plotted in, the distribution is always more likely to shift the profile down.

To anticipate the resulting parameters Figure 3.3 can be compared to the parameter guideline in Figure 3.1, which shows that skewing the profile down could shift the acceleration time down and provide a sharper peak to pivot at. It could also shift the escape time when trying to correct itself back to the original intensity profile (as though the two numbers are oscillating about the equilibrium). The guide also shows a slower decay phase for lower MFP values, while drastically changing the profile (sloping downwards and forming a 'cone' at the peak) at higher values so there is little anticipation for change in the $\lambda_\parallel$ value.

3.5.3 Numerical Modeling of Synthetic Data

Fitting this data set should be straightforward as the best-fit values ought to be approximately what the original model values are ($\lambda_\parallel = 0.5$ AU; $\tau_a = 0.1$ hrs; and $\tau_e = 0.8$ hrs), potentially shifted slightly downward to adapt to the noise added in Section 3.5.2. Figure 3.4 displays the best fitting results for the synthetic data; the panels on the right outline what the R^2 results are for each final parameter value.

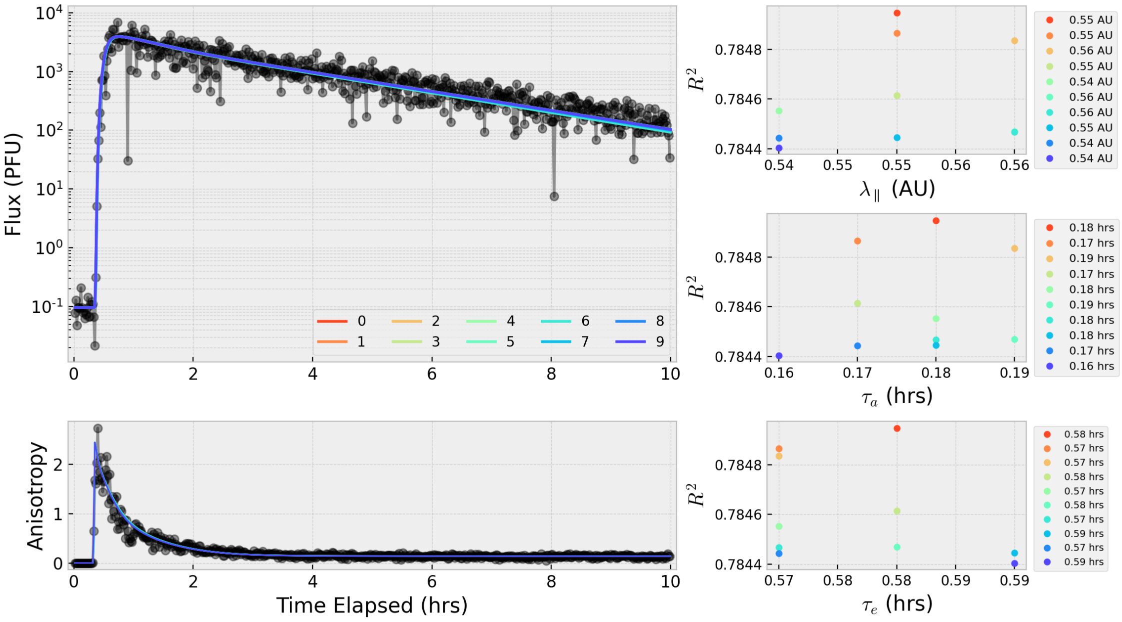

Figure 3.4: The grid result when fitting the synthetic data. The top left panel shows the particle flux result in PFU for the top 10 results (in order from best fit to worst fit), and the bottom-left panel shows the anisotropy for those same results. The right panels show the R^2 results for each of the free parameters.

Considering the goodness-of-fit graphs from Figure 3.4 (right panels), it can be seen that as the model fit improves the scatter points converge to the best fit and are not arbitrarily distributed. The flux and anisotropy for the top 10 best fits are plotted on the left panels where it is clear that there is very little difference between sets. In terms of the R^2 values, the top two values are $R^2 = 0.78495$ and $R^2 = 0.78487$, with a difference of only 8×10^{-5} between them.

3.5.4 Interpretation of Synthetic Fit

The best possible fit for the free parameters (up to 2 decimal places), with an R^2 = 0.78, is seen in Figure 3.5, where the resulting free parameter values are $\lambda_\parallel$ = 0.55 AU, τ_a = 0.18 hrs, and τ_e = 0.58 hrs.

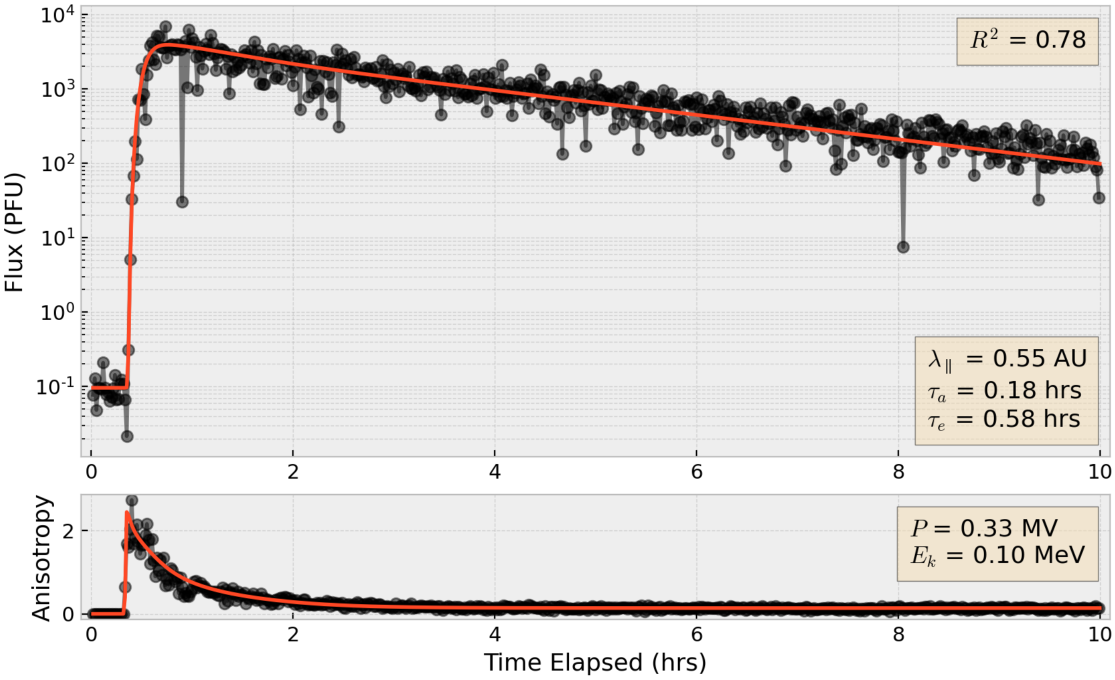

Figure 3.5: The best-fit result (where R^2 = 0.78) of fitting the synthetic data created using $\lambda_\parallel = 0.5$ AU, $\tau_a = 0.1$ hrs, and $\tau_e = 0.8$ hrs. The particle flux in arbitrary units is in the upper panel and the anisotropy is in the lower panel.

While the derived value of $\lambda_\parallel$ is not substantially different from the original value, a quick calculation can be done to quantify the difference. The MFP has a final best-fit value of 0.55 AU; this is only 0.05 AU or 10% different to the original value that the synthetic data is created with. Based on the free parameter guideline, this further indicates that the majority of the profile is defined using the $\lambda_\parallel$ variable.

Applying the same comparison with the acceleration time shows a much bigger difference where the best fitting value is 0.08 hrs different to the original value of 0.10 hrs. This is a difference of 80% after fitting the data. Considering the free parameter guideline, this parameter mostly influences how sharp the peak is and the vertical onset. It could be argued that the incorporation of noise disrupted this profile by making the distribution around the peak blunt enough that the acceleration time is directly impacted, resulting in a value that is almost double that of the original.

Lastly, the difference in escape time after fitting the data is 27.5% lower (with 0.22 hrs) than the original value of 0.80 hrs. This is a much smaller change in terms of the total percentage difference. While adjustments in the escape time mostly influence the distribution around the peak, which experiences slight changes to its slope from τ_e = 0.5 to 7.0 hrs (as seen in Figure 3.1). This explains why the distribution around the peak influences the acceleration time so much more than the escape time, and how this value has a much smaller difference in terms of the percentage when compared to τ_a.

3.6 Summary and Conclusion

This chapter introduces the 1D SEP transport model, developed by van den Berg et al. (2020), and all the parameters and assumptions required to run it, including the Reid-Axford injection model (Reid, 1964; Axford, 1965). The chapter then explores the CoD goodness-of-fit test, denoted using R^2, which guides the model simulations towards the best fitting parameters as seen in Figure 3.4. To understand how the model and R^2 test work, synthetic data are created with the use of Python functions to add somewhat realistic noise. The synthetic data are tested against numerous simulations until the best possible fit is found, shown in Figure 3.5.

With the aid of the free parameter guides, a better understanding of the impact that the flux and anisotropy time profiles experience due to each free parameter is gained. Figure 3.5, however, indicates how open the parameters are to interpretation. Without further insight, many assumptions can be made about the injection parameters.

While the free parameter guides can be useful, they are not holistic in describing every energy's results, and consulting these figures is not meant to provide definite conclusions. Despite the indication of parameter boundaries seen in the free parameter guides, there are also values for which the model becomes unstable and is unable to produce intensity (and thus anisotropy) values for arbitrary combinations of parameters. This is something that is considered throughout Chapters 4 and 5.

This chapter lays a foundation for the understanding of how to model observations and a start on how to interpret the results.

Chapter 4

Numerical Modelling of Observational Data

4.1 Introduction

The aim of Chapter 4 is to introduce the procedure of finding appropriate SEP events that satisfy all requirements for the model and illustrate the outcome of finding the best fit. The process of fitting observational data with the focused transport model, discussed in Chapter 3, is only applied to fit synthetic data in a hypothetical scenario. When working with real-world data it is vital to recall any restrictions that the model or data processing puts in place. The model only considers 1D transport and therefore requires a good magnetic connection from the observing instrument to the flare site; Section 4.2.1 explains how this can be found. Understanding this restriction, observations can then be found by surveying various solar event archives to find appropriately large particle events that have the potential to be recorded by a magnetically well-connected instrument.

Having found events to model, Sections 4.2.2 and 4.2.3 explain how the JHelioviewer program and Solar **MA**gnetic **C**onnection **H**aus (Solar-MACH) tool are used to confirm the location, size, and time of the eruption, and corroborate that the instruments are magnetically connected. A key aim of this project is to remove as much subjective input as possible, using scientific reasoning and calculations to make most of the decisions; this restriction is mostly seen when the data is initially compiled and the judgement to use that specific set comes down to the time onset normalisation procedure set up in Section 4.2.4.

Note that any times mentioned in the following chapters are in reference to the Coordinated Universal Time (UTC).

4.2 Observations

In order to find large SEP events there are a multitude of archived lists for solar flares, including the Space Climate Groups Catalog[1], NASA's list of Major SEP Events[2], and SpaceWeatherLive.com's archive for solar flares[3].

Solar flares are classified under five different labels using a logarithmic scale based on the soft X-ray peak flux magnitudes (Ursi et al., 2023), evidenced by Figure 4.1. Using this scale, the flares are defined as the corresponding letter and float value.

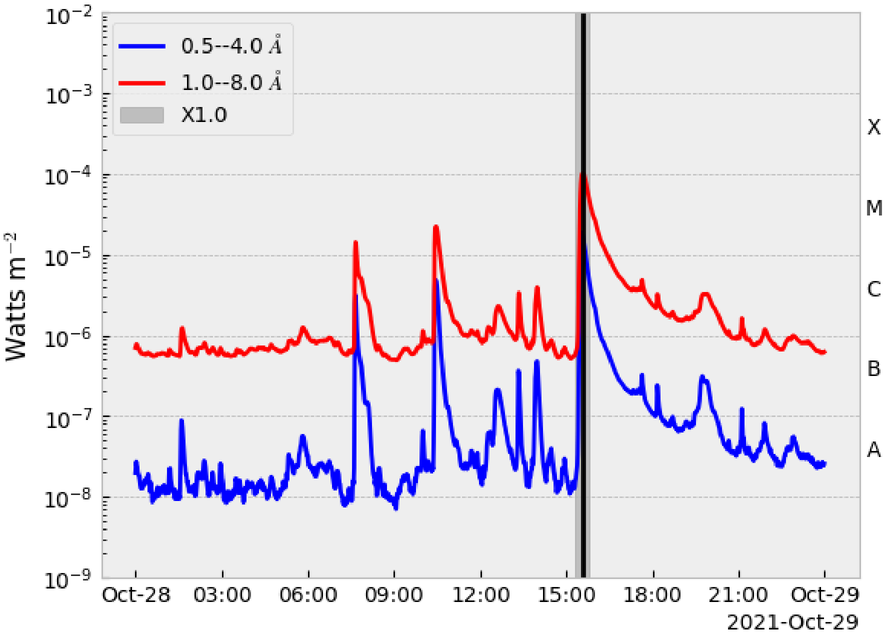

Figure 4.1: The classification of solar flares based on their peak flux magnitudes in the 1.0 – 8.0 Å wavelength band. This figure is created using the SunPy Python package (The SunPy Community et al., 2020). Focus is put on the 1.0 – 8.0 Å wavelength band which corresponds to approximately a 1.5 – 12.5 keV energy range (Ursi et al., 2023). This graph is plotted over the full 24 hours of 28 October 2021.

In the case given in Figure 4.1, the highlighted flare is shown to be of magnitude 1.0×10^{-4} W.m^{-2} which corresponds to a value of X1.0. Each letter corresponds to the opposing units scale such that 'A' is $n \times 10^{-8}$ W.m^{-2}, 'B' is $n \times 10^{-7}$ W.m^{-2}, 'C' is $n \times 10^{-6}$ W.m^{-2}, 'M' is $n \times 10^{-5}$ W.m^{-2}, and 'X' is $n \times 10^{-4}$ W.m^{-2} (where n is the float value from 1.0 to 9.9). X-class flares however do exceed this n range and have been recorded to go as high as X28.0 (Kaufmann et al., 2012).

Background activity is predominantly measured to be within the B-class (between $1.0{\times}10^{-7}$

---

[1] http://www.stil.bas.bg/SEPcatalog/homeind_new.html

[2] https://cdaw.gsfc.nasa.gov/CME_list/sepe/

[3] https://www.spaceweatherlive.com/en/solar-activity/top-50-solar-flares/year/2023.html

and 1.0×10^{-6} W.m^{-2}), therefore this project mostly considered flares in the M- or X-classes to ensure that the background activity is minimally intrusive.

4.2.1 Magnetic Connectivity

Given that the model, discussed in Section 3.2, is 1D, it only describes particle transport along a single magnetic field line. As discussed in Section 2.4, the guiding centre of the charged particle will therefore only follow the Parker HMF line away from the Sun (Roelof, 1969; van den Berg et al., 2020). Using this Parker line as the axis in which the motion of the particle is confined, the model restrictions will be satisfied.

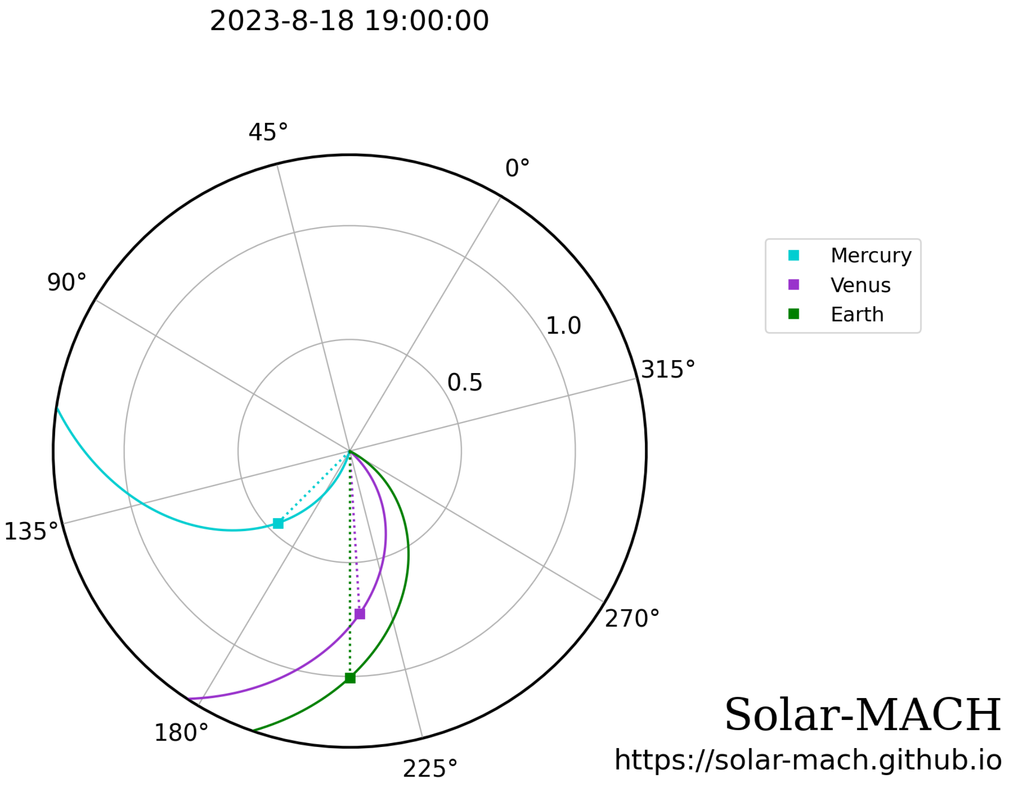

Figure 4.2: Figure generated using the Solar-MACH tool displaying the three closest planets to the Sun and their Parker Magnetic Spirals using V_{sw} = 400 km.s^{-1} (Gieseler et al., 2023).

Using Figure 4.2 as a guide, where the Sun is at the origin, the particles would therefore be required to traverse one of the coloured spirals to reach the respective coloured circles for that planet to be magnetically connected. To find an instrument measuring SEPs on a field line originating from the flare site would make it a magnetically connected event measurement.

Roelof (2015) notes that the recording instrument's magnetic footprint must lie within 30° of the flare site for it to be considered magnetically well-connected. The limit on the distance used for this project is set to a maximum of 27° from the flare site. With this knowledge in hand, Jhelioviewer is used to get the location of the flare and Solar-MACH can confirm if there are any instruments that were connected at the time.

4.2.2 JHelioviewer

Using the dates and times for the largest registered solar flares, JHelioviewer is utilised to locate a more definite time and position for the flare's eruption. This visualisation tool, forming part of the ESA/NASA Helioviewer Project, is an open-source desktop and web application allowing anyone with access to a computer and internet connection to explore the Sun and inner heliosphere (Müller et al., 2017).

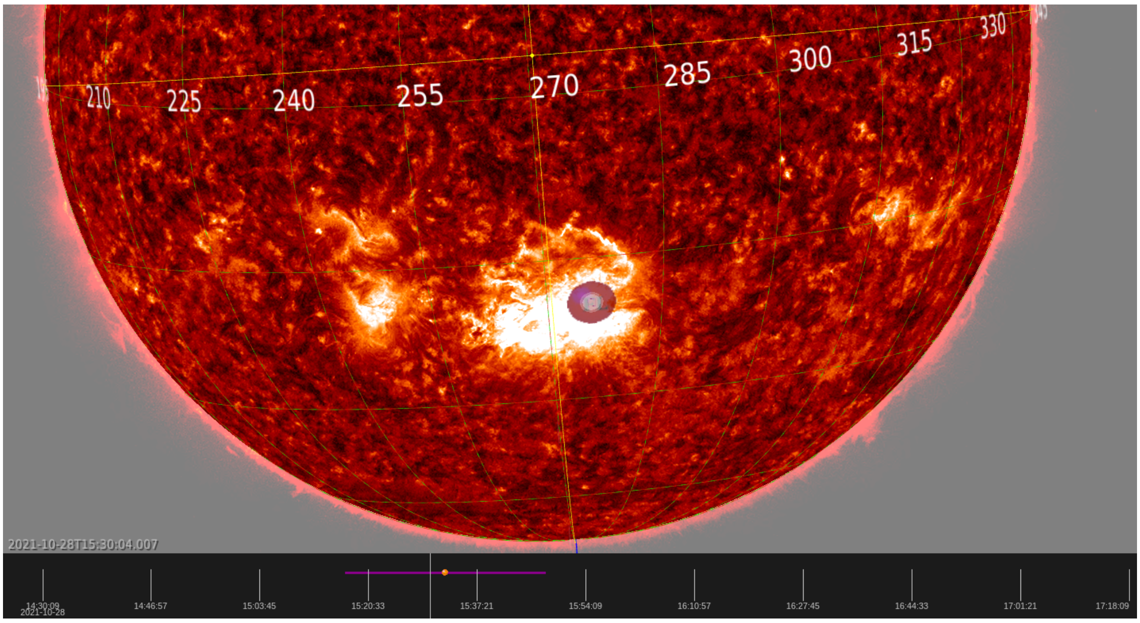

Figure 4.3: Snapshot from JHelioviewer using the SDO AIA 304 Å images for the flare at 15:30 associated with GLE#73 on 28 October 2021, located at the red circle which is approximately (270°, −29°) in Carrington coordinates (Müller et al., 2017).

According to Müller et al. (2009, 2017), JHelioviewer provides images and stop-motion movies using footage captured through telescopes on board various spacecraft, such as the **S**olar **D**ynamics **O**bservatory (SDO, Pesnell et al., 2012) and the **S**olar **TE**rrestrial **RE**lations **O**bservatory (STEREO-A, Kaiser et al., 2008).

There are a variety of telescopes imaging the Sun in various fields of view across the spacecraft currently in orbit (Müller et al., 2017; Hurlburt et al., 2012). As an example of the many instruments capturing the Sun, there are the twin STEREO spacecraft that have the **S**un-**E**arth **C**onnection **C**oronal and **H**eliospheric **I**nvestigation (SECCHI) instrument on board which consists of five telescopes: the **E**xtreme **U**ltraviolet **I**mager (EUVI), two Coronagraphs (COR1 and COR2), and two **H**eliospheric **I**magers (HI1 and

HI2); for more information on this instrument suite see Howard et al. (2008). Of these five telescopes: the EUVI and HIs image the low corona at different radial distances, and the coronagraphs image the inner and outer corona (Howard et al., 2008). These cameras use a variety of filters to be able to capture as many solar phenomena as possible (Howard et al., 2008). Figure 4.3 is an image taken from the JHelioviewer desktop application of the GLE#73 event with the SDO AIA instrument measuring with the 304 Å ultraviolet passband (Müller et al., 2009, 2017).

The main features of JHelioviewer include being able to efficiently browse through repositories to find events or regions, overlaying multiple images or filters, and adjusting layer transparency levels to better observe certain features on the Sun. The bottom panel of Figure 4.3 is a timeline of solar flare events from the **H**eliophysics **E**vents **K**nowledgebase (HEK, Hurlburt et al., 2012), archived into the **S**pace **W**eather **E**vents **K**nowledgebase (SWEK) built specifically for the Helioviewer Project (Müller et al., 2017). To get the starting time for the flare in Figure 4.3 eight minutes must be subtracted from the observed start of the instruments to account for the photon travel time, thus the resulting flare start is estimated to be 15:07.

Setting the grid in the program to Carrington coordinates and hovering the mouse over the still-image of the flare site provides an approximate location in longitude and latitude, which can then be compared to the potential receiving instruments to note their magnitude of magnetic connection. According to Bhatnagar and Livingston (2005), Carrington coordinates are defined in such a manner that the heliographic latitude is measured from the Sun's South pole to the North Pole as −90° to 90°, and the longitude is measured as a full rotation starting from the meridian, called the Carrington Central Meridian, heading West from 0° to 360°. This central meridian is internationally agreed to be the apparent centre of the disk as of 1 January 1854 at 12:00 (Bhatnagar and Livingston, 2005).

4.2.3 Solar-MACH

The date, time, and location of the solar flare are then inserted into the Solar-MACH tool created by the **S**olar **E**ne**R**getic **P**articl**E** a**N**alysis pla**T**form for the **IN**ner h**E**liosphere (SERPENTINE) group in Turku, Finland (Gieseler et al., 2023), with examples shown in Figures 4.2 and 4.4. Each coloured circle indicates a planet or spacecraft actively in orbit around the Sun at the time of the event, with the radial distance from the centre providing the scaled radial distance in AU that they are from the Sun. The lines that connect the spacecraft to the Sun are the Parker HMF spirals, calculated using the average solar wind speed of $V_{sw} = 400$ km.s^{-1}. The straight black line with the arrow indicates the position of the flare and the direction that it erupted towards, while the dashed spiral denotes the Parker spiral connected to the flare site.

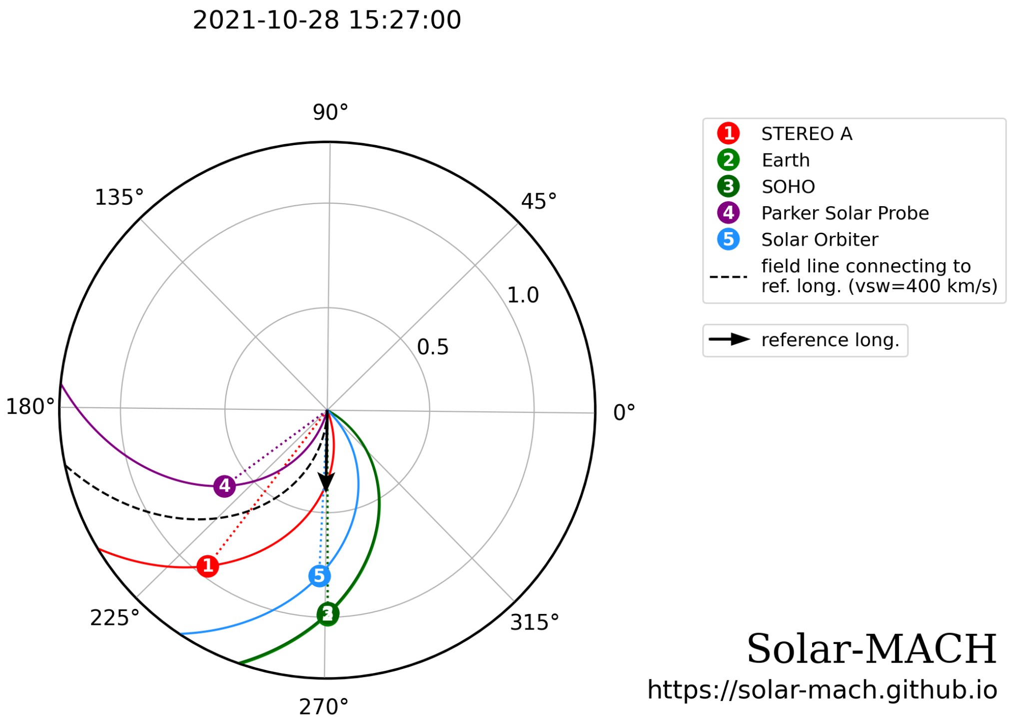

Figure 4.4: Figure provided from the Solar-MACH tool, created by the SERPENTINE group, provides the Parker spirals of the flare and the instruments actively in orbit during that time period (Gieseler et al., 2023). This figure specifically shows the spacecraft, Earth, and the flare for the event on 28 October 2021 (GLE#73) with the peak intensity of the flare occurring at 15:07 and peaking at 15:27 at Carrington coordinates (270°; −29°).

From this diagram, it can be deduced that the STEREO-A and **P**arker **S**olar **P**robe (PSP Fox et al., 2016) instruments are closest to the flare's Parker Spiral, and from the data output that the tool has provided (seen in Table 4.1), they are approximately 22° and 15° away, respectively.

Included in Table 4.1 is the connection of the Earth, which is indicative of spacecraft in orbit around or near the planet or instruments at ground level, such as NMs, that could potentially be measuring SEP data. The most common spacecraft represented by Earth in the Solar-MACH tool for the purposes of this project are from the **G**eostationary **O**perational **E**nvironmental **S**atellite (GOES[4]) and Comprehensive Solar Wind Laboratory for Long-Term Solar Wind Measurements (WIND[5]) missions.

---

[4] https://www.nasa.gov/content/goes-overview/

[5] https://wind.nasa.gov/

	Earth	**PSP**	**SOHO**	**Solar Orbiter**	**STEREO-A**
Magnetic Connection (°)	62	-15	62	48	22
Radial Distance (AU)	0.99	0.62	0.98	0.80	0.96

Table 4.1: Earth and multiple spacecraft positions from the flare for GLE#73 on 28 October 2021 in which the flare started at approximately 15:07 at (270°; −29°). Values are provided using the Solar-MACH tool (Gieseler et al., 2023).

4.2.4 Time Onset Normalisation

The flare is now found along with the instruments that are magnetically well-connected, but this still does not imply that the data will be good enough to fit. Chapter 2 discussed all the different influences that exist in the inner heliosphere that could have an impact on what the instrument measures.

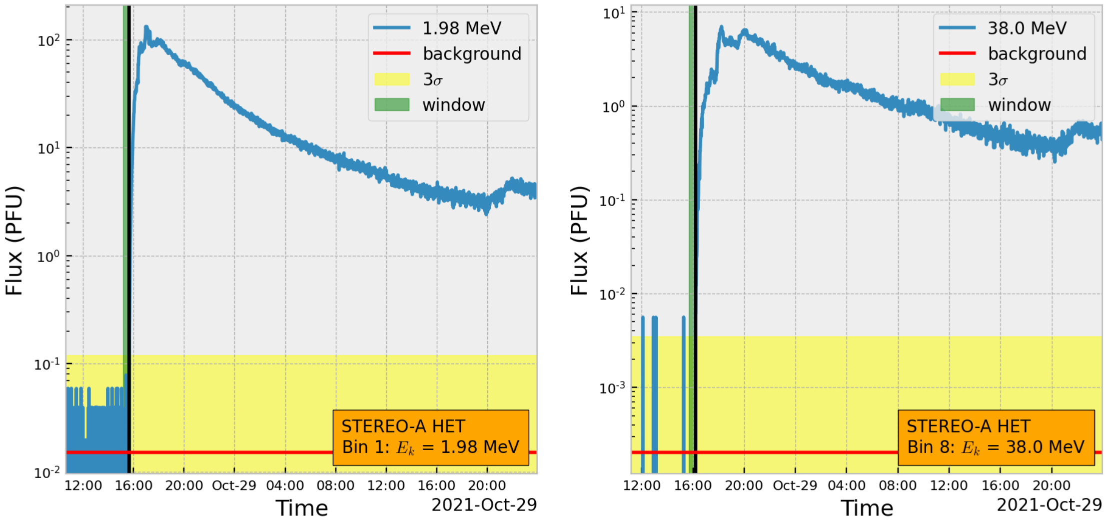

Figure 4.5: STEREO-A **H**igh **E**nergy **T**elescope (HET) electron (left) and proton (right) bins for energies of $E_{k,e}$ = 1.98 MeV and $E_{k,p}$ = 38.0 MeV, for the 28-29 October 2021 GLE event.

Looking at Figure 4.5, it can be viewed as a subjective choice to fit an energy bin (a set of data that is measured within a specific energy range). Using another tool created by the SERPENTINE group, but rewriting it slightly, the choice to use an energy bin mostly comes down to whether or not the data displayed an acceptable onset time. When an instrument starts observing SEPs from a flare at a higher level than the background, it is called the onset and for impulsive SEP events it is seen as a flux increase in the form of a steep vertical line, as seen in Figure 4.5 at approximately 16:00 on 28 October 2021. The same sharp increase is also seen in the anisotropy before sloping back to zero again soon after.

To calculate the onset time, the implemented tool uses a 3-σ method outlined below:

1. Define a window period that is made up entirely of the pre-event background; this is the green vertical bar in Figure 4.5 that takes up approximately 30 minutes.
2. Calculate the particle intensity mean ($\bar{x}_B$, the red horizontal line) and standard deviation (σ_B, the yellow shaded area around the mean) of this window interval.
3. Compare the next intensity value following this window (x_1) to the background interval, testing if it agrees with the expression: $x_1 > \bar{x}_B + 3\sigma_B$.
    (a) If it is greater than the expression then check the next point: $x_2 > \bar{x}_B + 3\sigma_B$.
    (b) If this is also true then the onset is found at the time where x_1 occurred.
4. If the expression is false then shift the window period forward by one timestep and repeat steps two and three until the time onset is found.

Figure 4.5 displays the range in which the window is calculated as the green highlighted region, what the mean value is from the horizontal red line, where the σ range falls in the highlighted yellow region, and the onset time as the vertical black line. An upside to calculating the onset is that a **V**elocity **D**ispersion **A**nalysis (VDA) can be calculated without relying on a by-eye method. A downside is that due to the Sun's activity, this time onset can be influenced by other flares and interruptions.

4.3 GLE#73: 28 October 2021

Section 2.3.2 introduces GLEs as SEP events which are detected at ground level by NMs. Only 73 GLEs have been recorded since the 1940s and they occur with a frequency of about 0.9 per year (Papaioannou et al., 2022). The previous solar cycle (Solar Cycle 24 or SC24) included the fewest GLE reports per cycle with the only one occurring on 17 May 2012 (also fitted in Appendix Section A.2). Some insights into why SC24 was so inactive were covered in Vainio et al. (2017).

The most recent GLE event recorded at the time of writing occurred on 28 October 2021, which is the first and currently the only GLE for the current solar cycle (Solar Cycle 25 or SC25) (Papaioannou et al., 2022; Martucci et al., 2023). NMs and spacecraft, such as SOHO and STEREO-A, are reported to have observed the onset of particles at approximately 16:00 (Mishev et al., 2022; Papaioannou et al., 2022; Martucci et al., 2023).

4.3.1 The Observation

Multiple large (M-class or higher) flares were recorded by GOES on 28 October 2021 shown in Figure 4.1. SEPs from the last flare, occurring just after 15:00, were measured on Earth, thus making this event a GLE (Papaioannou et al., 2022). From this same figure, it can be seen that the flare had a magnitude of 10^{-4} W.m^{-2} which implies that it is an X1.0 flare. The active region causing all three large flares is NOAA AR12887 (Papaioannou et al., 2022; Martucci et al., 2023).

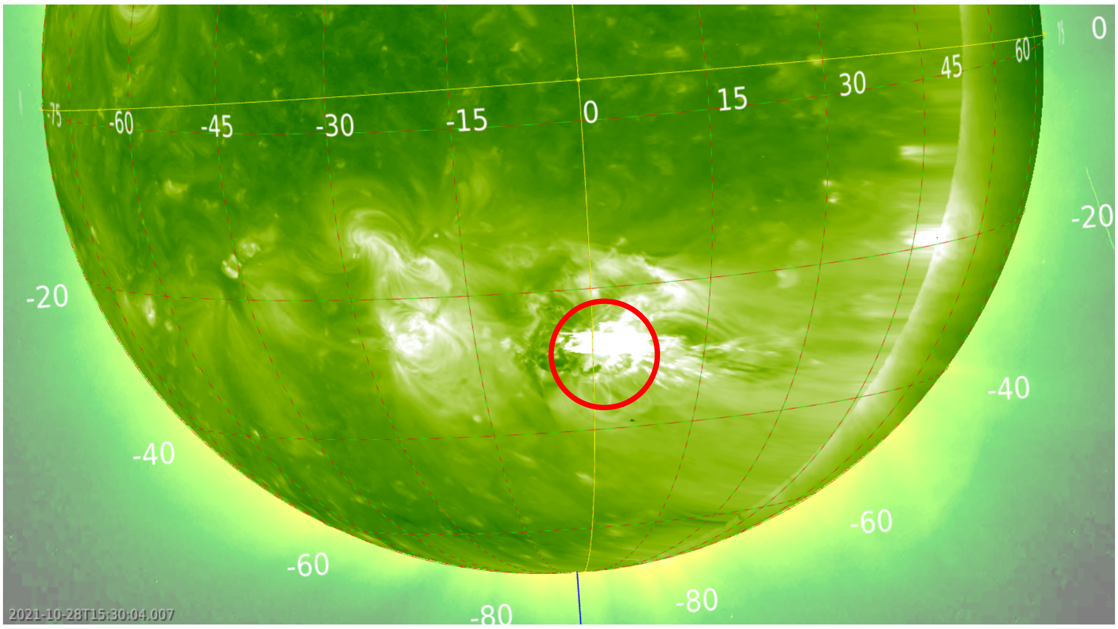

Figure 4.6: Snapshot from JHelioviewer using STEREO-A EUVI 195 Å images for the flare at 15:30 associated with GLE#73 (28 October 2021), located at approximately W02S26 in Stonyhurst coordinates. (Müller et al., 2017).

The solar flare associated with this event, seen in Figures 4.3 and 4.6, erupted at approximately 15:07 at the Carrington Coordinates (270°, −29°) and W02S26 in Stonyhurst Coordinates. These values correlate to the results seen in Papaioannou et al. (2022) and Martucci et al. (2023). Stonyhurst Coordinates use the intersection of the central meridian on the Sun as seen from Earth and the solar equator as the central point of the coordinate system (Thompson, 2005). This is the more commonly found coordinate system within scientific articles. The position is provided in terms of **N**orth or **S**outh (from 0 – 90°), and **E**ast or **W**est (0 – 180°). Note that the Solar West limb is increasing to the right while the East increases to the left.

For this event, the best magnetic connection, seen in Figure 4.4 and using Table 4.1, is to PSP, with its magnetic footprint at 15° away from the flare; the only other notable connection being STEREO-A at 22°. This means that this event can potentially be fitted at two radial distances, 0.62 AU and 0.96 AU, respectively.

4.3.2 Validating the Data

The time onset graphs shown in Figures 4.5 and 4.7, demonstrate that the event has the potential to be fitted to an array of electron and proton data. The STEREO-A data in Figure 4.5 shows a well-defined time profile with little deviation in its form.

Both the example bins for electrons and protons illustrate the flux increasing by almost four orders of magnitude from the averaged pre-event background intensity. There are some visible fluctuations, the most visible being at the peaks, that will need to be taken into consideration when applying the goodness-of-fit test as the model will create a smooth profile around any such fluctuations. The PSP data in Figure 4.7 show similar intensity increases at the onset when compared to the STEREO-A data.

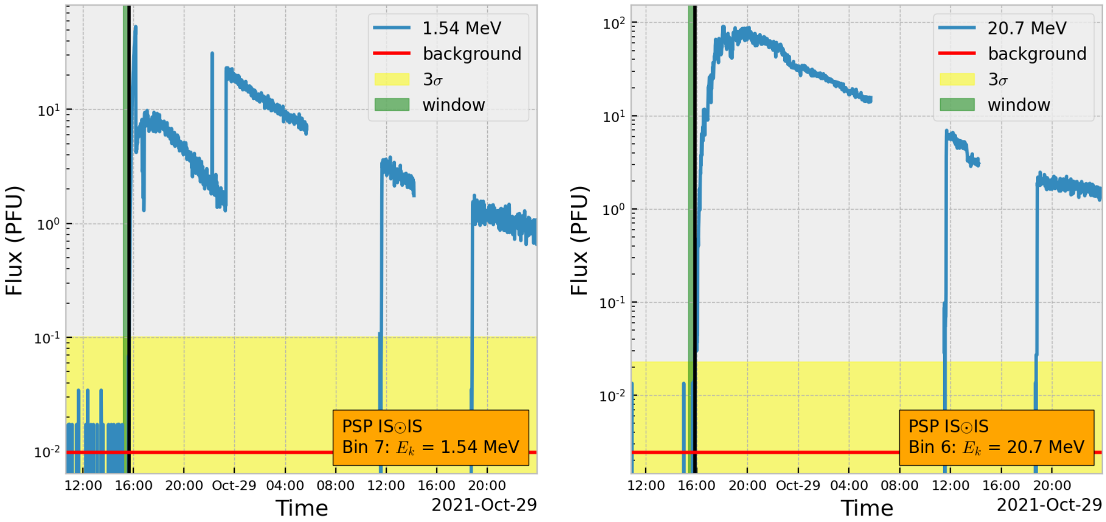

Figure 4.7: PSP **I**ntegrated **S**cience **I**nvestigation of the **S**un (IS⊙IS) electron (left) and proton (right) bins with energies of $E_{k,e}$ = 1.54 MeV and $E_{k,p}$ = 20.7 MeV for the 28-29 October 2021 event.

From the aforementioned figure, there are observable gaps in the PSP data from approximately 06:00 to 12:00 and 14:00 to 19:00 on 29 October 2021, and the PSP electron data peaks experience a stepwise decrease due to an instrument issue that occurred early in the mission from about 16:00 to 00:00 on 28 October 2021. Some discontinuities can be accounted for during the fitting process; however, the PSP electron data are not a data gap that can be worked around. When modelling electron transport, only the first 10 hours after the eruption are compared (20 hours for protons), but the shifted data account for eight of those hours, so the model will try to fit the shifted values as well as the main time profile. The PSP electron data are not utilised due to the stepwise decrease in the time profile after the peak skewing the parallel MFP results.

Taking into account the discontinuities mentioned in this Section, the full set of results for fitting the model to the observations are summarised in Table 4.2 and one of the final best-fit results for each instrument is displayed in Figures 4.8 and 4.9. Note that the fitting process limits all the free parameter values to the range 0.01 to 9.99.

4.3.3 Fitting Results

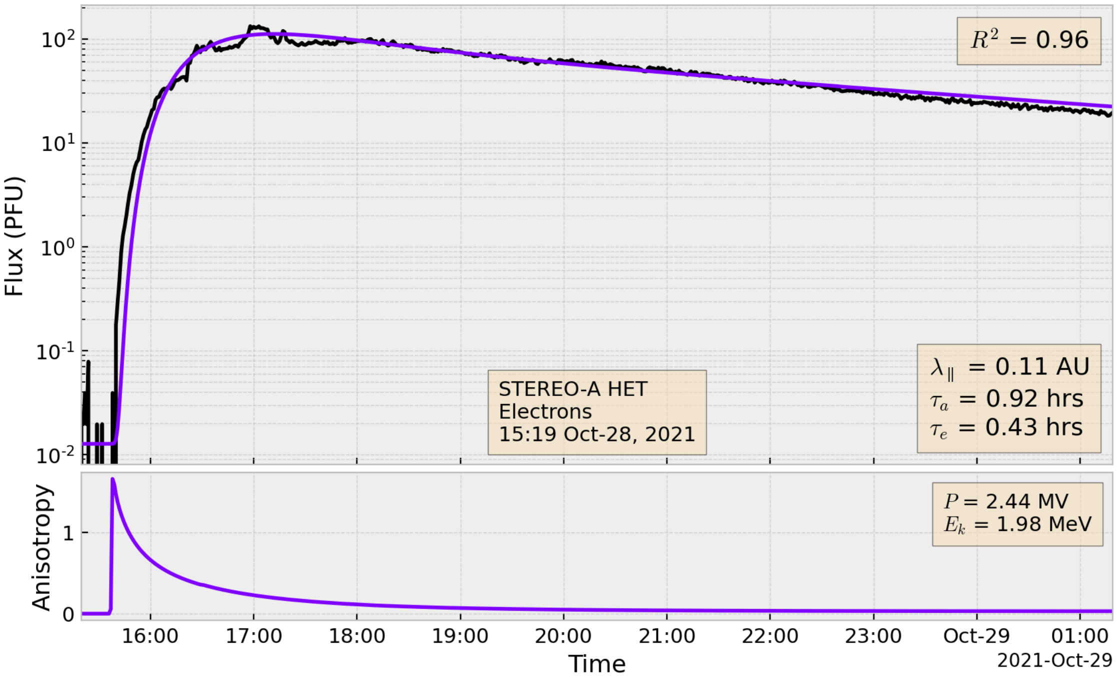

Figure 4.8: The result for the first STEREO-A electron bin that has a goodness-of-fit of $R^2 = 0.96$. The mean energy for this bin is $E_k = 1.98$ MeV, that corresponds to a rigidity of $P = 2.44$ MV, and the corresponding parameter best-fit are $\lambda_\parallel = 0.11$ AU, $\tau_a = 0.92$ hrs, and $\tau_e = 0.43$ hrs.

Figure 4.8 shows a best-fit model-data comparison that compares well with the observational data, including around the onset peak where the data appear to fluctuate slightly. However, the model gives a steeper increase compared to the observations which show a more gradual increase than what is normally expected. The anisotropy in the panel below indicates a smooth time profile where the particles become isotropic just after 18:00, three hours after the flare initially erupted. The isotropic decay phase of the event is what impacts the MFP the most, as seen in the free parameter guide from Section 3.3.1. Thus, due to the fit of the declining slopes being so unambiguous, the $\lambda_\parallel$ result can be trusted. However, the calculated onset is an imperfect comparison during the increasing phase, which implies that the acceleration and escape times are less trustworthy.

The gaps in the PSP data discussed earlier in Section 4.3.2 are visible again in Figure 4.9. However, the remaining data are still sufficient such that the model can fit the onset and tail, allowing the reader to build faith in the result. The proton PSP data for the

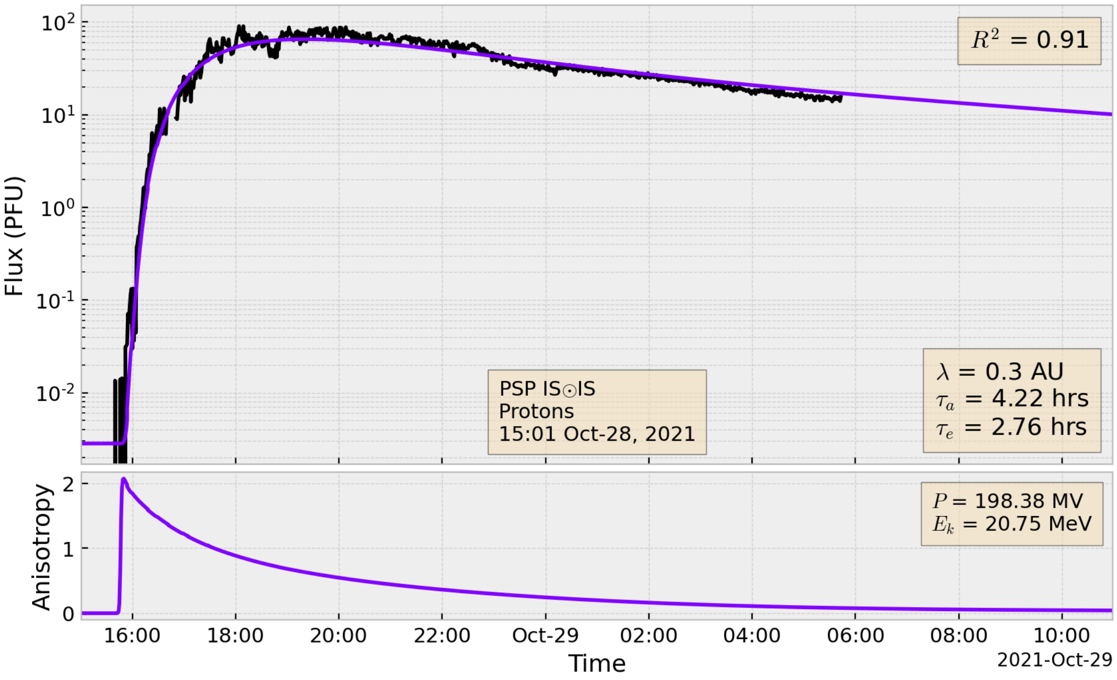

Figure 4.9: The result for the sixth PSP IS⊙IS proton bin that has a goodness-of-fit of $R^2 = 0.91$. The mean energy for this bin is $E_k = 20.75$ MeV which corresponds to a rigidity of $P = 198.38$ MV, and the free parameter results are $\lambda_\parallel = 0.30$ AU, $\tau_a = 4.22$ hrs, and $\tau_e = 2.76$ hrs.

bin with energy $E_k = 20.75$ MeV show a more gradual onset corresponding to the high acceleration and escape times. The fluctuating peak provides a smooth enough shape to fit which is why the goodness-of-fit can be as high as $R^2 = 0.91$. The profile beyond the peak, where the MFP is most defined, deviates slightly from the best-fit model from 02:00 on 29 October 2021 which would imply that the MFP is not as close as it should be. The anisotropy in the lower panel of Figure 4.9 shows the particles only becoming isotropic from approximately 00:00, eight hours after the onset is recorded.

The far-right column of Table 4.2 displays the R^2 goodness-of-fit result (as discussed in Section 3.4) where the average goodness-of-fit value for the whole event comes to approximately $R^2 = 0.89$ in agreement with the fit.

By aligning the onset time of the model and observations, the time given by the first data point in the model data is taken to be the calculated start time of the event according to that energy bin. Considering the start time of the event that is recorded using JHelioviewer in Section 4.2.2 to start at approximately 15:07 on 28 October 2021, this can be compared to the calculated start times in column four of Table 4.2. The average time calculated for the start time for all the data sets comes to 15:01 which is only six minutes earlier than the recorded time. The difference between the times could be due to a multitude of reasons, including other activity at the Sun that is causing an influx earlier than anticipated, or the

Instrument	**Species**	**Bin**	**Event Start**	**Energy (MeV)**	**Rigidity (MV)**	$\lambda_{\parallel}$ **(AU)**	τ_a **(hrs)**	τ_e **(hrs)**	**Peak Flux**	R^2
STEREO-A (HET)	Electrons	0	15:19	0.99	1.41	0.13	1.38	0.47	227.95	0.95
		1	15:20	1.98	2.44	0.11	0.92	0.43	132.32	0.96
		2	15:15	3.35	3.83	0.14	1.70	0.37	46.62	0.95
	Protons	0	14:49	14.30	164.44	0.31	9.99	1.02	20.554	0.72
		1	14:59	16.00	174.02	0.30	9.99	0.89	18.932	0.78
		2	14:58	18.10	185.19	0.33	9.99	0.92	16.435	0.79
		3	14:57	22.20	205.31	0.37	9.99	0.93	13.654	0.83
		4	14:59	25.10	218.48	0.35	9.99	0.84	11.104	0.88
		5	14:57	27.90	230.51	0.34	8.29	0.93	10.096	0.91
		6	15:13	31.40	244.77	0.35	4.71	1.28	9.1884	0.94
		7	15:09	34.60	257.15	0.35	5.68	1.02	8.3272	0.93
		8	15:03	38.00	269.73	0.35	7.48	0.79	7.0200	0.93
		9	14:55	49.00	307.17	0.36	9.97	0.55	5.3876	0.92
		10	14:55	77.50	389.16	0.36	9.98	0.44	2.7621	0.95
PSP (IS⊙IS)	Protons	1	14:47	8.72	128.23	3.00	9.99	2.50	720.89	0.75
		2	14:18	10.37	139.90	0.08	9.69	0.82	230.41	0.78
		3	14:38	12.34	152.64	0.07	7.15	0.78	196.51	0.92
		4	14:49	14.67	166.55	0.06	3.83	0.72	146.80	0.87
		5	14:59	17.45	181.76	0.16	3.69	2.12	105.77	0.90
		6	15:01	20.75	198.38	0.30	4.22	2.76	90.425	0.91
		7	14:59	24.68	216.56	0.29	5.50	1.68	81.715	0.93
		8	15:04	29.34	236.45	0.63	5.72	1.91	63.600	0.94
		9	14:55	34.90	258.23	0.30	6.58	1.15	54.155	0.94
		10	15:11	41.50	282.09	0.60	4.46	1.79	40.060	0.93
		11	15:09	49.35	308.25	0.23	4.49	0.97	30.568	0.92

Table 4.2: Final fitting values for the 28 October 2021 event using measurements from STEREO-A HET and PSP IS⊙IS, where the observed peak flux is in terms of PFU. The columns include the event start time (calculated from the time onset), the energy provided for each bin, the calculated rigidity, the best-fit free parameters, the observed flux peak, and the goodness-of-fit result.

onset could be skewed due to the variations in the background data in the measurements.

No clear pattern is seen in the $\lambda_{\parallel}$ results for the PSP protons, with the STEREO-A electrons being confined to $0.11 - 0.14$ AU, and the STEREO-A protons are then found to be much higher with values of $0.30 - 0.37$ AU. The results should show a difference between the two proton results due to their different radial distances from the Sun, especially given that the rigidities overlap from $\approx 165 - 308$ MV.

Acceleration time values commonly reach much higher values in some bins than anticipated, taking a minimum acceptable goodness-of-fit value as $R^2 = 0.80$. The corresponding R^2 values for these high acceleration times indicate that many of the final model fits are not acceptable in terms of the observations. These τ_a times are most likely as high as they are due to the slope/curve at the onset not being comparable to the model within the limitations. The full set of results is found in Appendix Section A.3.

Finally, the escape times (usually disregarded and left to be $\tau_e = 1.0$ hrs in other scientific research) are all within $0.3 - 3.0$ hrs. During the process of fitting, it is found that the two Reid-Axford times are influenced by each other. The procedure often starts with the MFP found first, then the escape time, and then the acceleration time (with minor adjustments to the escape time). This implies that most of the shape is determined by the MFP, followed by the escape time, and finished with minor details from the acceleration time. However, the acceleration time being so large for some bins could imply more time required to find the final fitting values; most fitting grids start with (0.10, 0.50, 0.90) for all three parameters, so it might be different if the initial grid started with much higher values.

Chapter 5 explores the potential trends that have been detected from fitting various events. All the results for the events fitted in this project are found in Appendix A which includes the observational data as well as all the fitting results.

4.4 Summary and Conclusion

This chapter introduces the process of finding SEP events that correspond with the restrictions from the model and show examples of fitting these observations.

Information about the GLE#73 event on 28 October 2021 is found using JHelioviewer and Solar-MACH. This confirms where and when the solar flare erupted and which instruments were magnetically well-connected through their Parker spirals to the eruption site. The time onset normalisation then assisted in determining which observational data are objectively suitable for the fitting process where unreliable data sets are also manually discarded due to certain discontinuities. Thereafter, the chapter explored the final results for fitting the event with different species and at varying energy levels.

The information gathered about the event through the use of JHelioviewer and Solar-MACH corresponds to that of Papaioannou et al. (2022) and Martucci et al. (2023) which confirms the procedure and use of both tools in this process. While the time onset calculations can be a good initial tool to decide on which data can be fitted, examples like the PSP electron bin expose why more input is necessary to fully accept the data sets.

Scrutinizing the final results from the fitting procedure assisted in fully breaking down which parts of the time profile are responsible for determining each free parameter and how much influence they have in the final shape. There is potentially a radial influence on the proton MFP values as seen from some of the results at $r = 0.62$ AU and $r = 0.96$ AU.

In terms of obstacles faced in this chapter, the model runtime has a complementary connection to the magnitude of $\lambda_{\parallel}$ as a smaller MFP leads to a longer runtime. Having small MFP values for most of the bins does prove to be time-consuming.

The next chapter will explore any patterns or trends that may arise from the results of fitting this and the other events that are summarised in Appendix A.

Chapter 5

Unobservable Results

5.1 Introduction

By fitting the 1D SEP transport model to numerous observations, Chapter 5 aims to compare the free parameter results in various ways to find potential trends in these unobservable results. Chapter 3 defines the fitting process using the CoD goodness-of-fit test, while Chapter 4 outlines how to find observations that are within the constraints of the model's restrictions. Appendix A details the observations and fitting results for over a dozen events recorded at various distances at multiple energies for both electrons and protons.

A possible solar cycle dependence on the free parameters is investigated in Section 5.2, where both the 11- and 22-year solar cycles are considered. Section 5.3 discusses the energy spectrum at the particle source and at the observers at 1.0 AU. The Reid-Axford acceleration and escape times, measured at various distances and different levels of magnetic connection to the flare site, are explored in Sections 5.4 and 5.5. Section 5.6 briefly discusses a rigidity dependence on all three parameters, with the focus on the parallel MFP.

This rigidity-dependent MFP result is then compared to trends in historical observations by Dröge (2000) and Palmer (1982) in Section 5.7. Bieber et al. (1994) discusses an analytical theory considering these same trends. Section 5.8 breaks down this analysis and discusses how well it compares to the derived parameters.

All results presented in Chapter 5 have a goodness-of-fit that is greater than or equal to $R^2 = 0.80$. Table 5.1 defines the markers used in the upcoming figures unless otherwise stated.

Instrument Markers	
SOHO	□
WIND	○
STEREO-A	★
PSP	◇
GOES	⬡
SolO	△

Date Colours				
Orange	22 November 1998		**Gold**	11 June 1999
Moss Green	19 October 2001		**Pine Green**	20 February 2002
Green-Blue	1 November 2004		**Midnight Green**	14 August 2010
Prussian Blue	17 May 2012		**Medium Blue**	20 September 2015
Steel Blue	9 October 2021		**Marian Blue**	28 October 2021
Purple	18 January 2022		**Dark Magenta**	20 January 2022
Purple-Red	21 March 2022		**Red**	2 April 2022

Table 5.1: Markers and colours, representing different spacecraft and events, used for all the figures in Chapter 5. The results for electrons will have an open-faced marker, while the proton results marker face will be coloured in unless otherwise indicated.

5.2 Solar Cycle Dependence

Every 11 years the Sun experiences a full solar cycle, rising from minimal solar activity to solar maximum and back down to solar minimum (Hathaway, 2015). Solar activity changes are mostly visible in the number of sunspots recorded, as seen in Figures 5.1, 5.2 and 5.3 for Solar Cycles 23 (SC23; 1995-2009), 24 (sc24; 2009-2020) and 25 (sc25; 2020-). Figure 1 in Engelbrecht and Moloto (2021) shows the solar cycle to correlate with properties such as the Sun's tilt angle α_s, the HMF magnitude B, and the magnetic variance at Earth δB^2. From these properties, other values are impacted such as the solar wind speed, the Alfvén speed V_A, and focusing length.

In addition to these changes over the 11-year cycle, at the end of the 11 years, there is a polarity change in the magnetic field. The polarity is seen in Equation 2.1 as the sign of A. When $A > 0$ the magnetic field lines point outwards in the northern hemisphere of the Sun and inwards in the southern hemisphere. When $A < 0$ the reverse is true. This 22-year cycle is referred to as the dynamo model or Babcock cycle (Babcock, 1961).

Figure 2 in Engelbrecht and Moloto (2021) shows that the parallel MFP remains mostly constant in time for increasing rigidity up to $P \approx 2$ GV; thereafter the solar minima $\lambda_\parallel$ values are higher. This implies that any solar cycle dependence for $\lambda_\parallel$ is only expected at extremely high rigidities, while the highest rigidity utilised in the results presented here is 0.92 GV.

The $\lambda_\parallel$ results compared to the yearly sunspot number are seen in Figure 5.1. Unfortunately, derived values of $\lambda_\parallel$ are extremely sparse, and it is difficult to find a full trend, especially, during the solar minimum phases. However, the rise and decay of SC23 indicate that the MFP might be influenced by the solar cycle. Following the somewhat plateaued solar maximum for SC24, the sunspots decrease again and the 17 May 2012 results show that same decrease. In terms of a 22-year cycle dependence, one could only speculate that

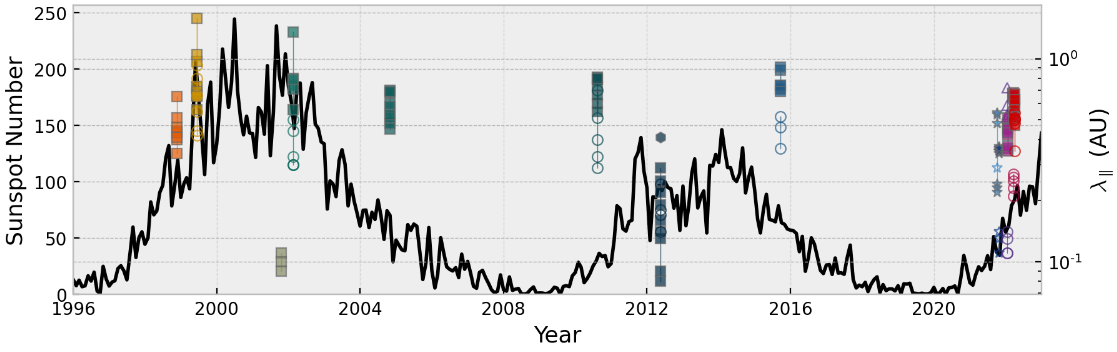

Figure 5.1: The sunspot number from 1996 to 2023 indicating the solar cycle, plotted using the SunPy package in Python (The SunPy Community et al., 2020), along with MFP values overlayed.

the upper limits of the event MFP results were lower for SC24. Without knowing the results for MFPs in solar cycles beyond the limits of the figure, it is difficult to ascertain whether there is a polarity dependence on the parallel MFP.

Other studies of solar cycle variation on the parallel MFP focus on GCR simulations using NMs, as done by Engelbrecht and Moloto (2021), Moloto and Engelbrecht (2020) and Chen and Bieber (1993). All three papers agree that the parallel MFP indicates a solar cycle dependence, while only Chen and Bieber (1993) note a solar magnetic polarity dependence. Chen and Bieber (1993), having studied a time frame of approximately 30 years, are able to show results for $\lambda_\parallel$ through most of that period. It was found that the $\lambda_\parallel$ values more than doubled when comparing the average during solar minimum with a positive polarity ($\lambda_\parallel$ = 0.8 AU) to the average during solar minimum with a negative polarity ($\lambda_\parallel$ = 2.1 AU, Chen and Bieber, 1993).

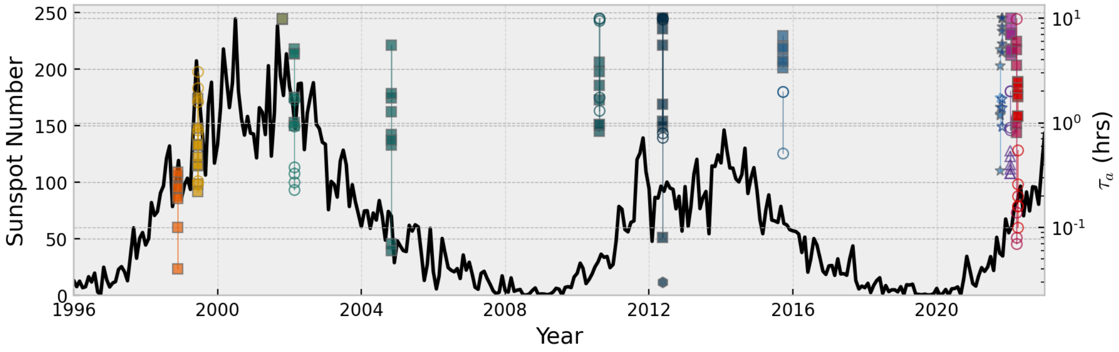

Figure 5.2: The number of sunspots indicating the solar cycle from 1996 to 2023, plotted using the SunPy package in Python (The SunPy Community et al., 2020), along with the acceleration time values overlayed.

The acceleration time results are compared to the sunspot numbers in Figure 5.2. The acceleration time results seem to follow the SC23. However, from the 2004 event onwards, there does not appear to be any pattern. More data are required to determine if there is a solar cycle dependence on the acceleration time.

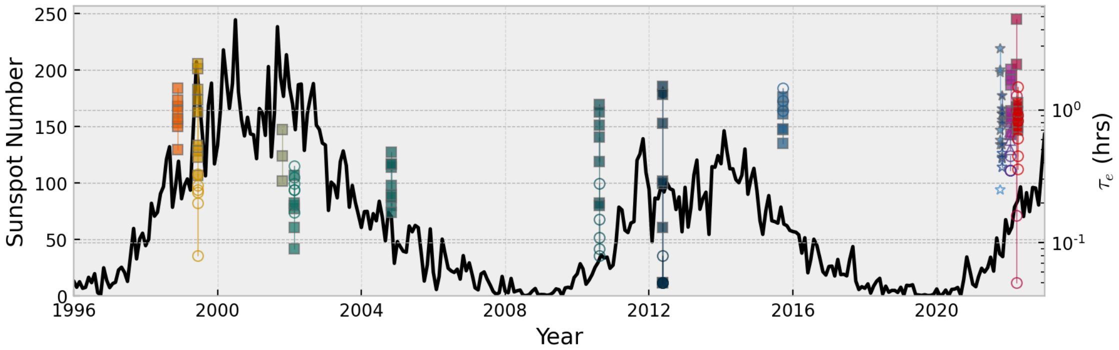

Figure 5.3: The sunspot numbers indicating the solar cycle, plotted using the SunPy package in Python (The SunPy Community et al., 2020), along with escape time values overlayed from 1996 to 2023.

The results of the escape time parameter over multiple solar cycles are shown in Figure 5.3. It could be argued that the upper limit for each event follows the same trend as the activity of the solar cycle. However, it could also be argued that the average for each event remains somewhat consistent. More data are required to determine if there is a potential solar cycle dependence on the escape time.

5.3 Energy Spectrum

Figures 5.4 and 5.5 show the energy spectrum for electrons and protons respectively. The left panels are the calculated Reid-Axford injection peak intensities and the right panels show the observed peak intensities at 1.0 AU. For each event at 1.0 AU, the maximum intensity for each energy bin is plotted as a function of that energy, removing any data sets that only contained one point and any data sets that would have resulted in a positively sloped power-law (Dresing et al., 2020).

The peak flux from the Reid-Axford injection profile is plotted using the resulting acceleration and escape times as well as the normalisation constant that was determined during the fitting process. The electron energy spectra show a slope that becomes flatter with radial distance. These results are comparable with Strauss et al. (2020) who also calculate an average spectral index for two radial distances (0.3 AU and 1.0 AU) to be $\delta = -3$. This indicates that the particles follow the same spectral shape almost entirely from their injection to 1.0 AU. According to Strauss et al. (2020), this is due to the minimal scattering.

The proton energy spectrum is seen in Figure 5.5 where the injected spectral index follows

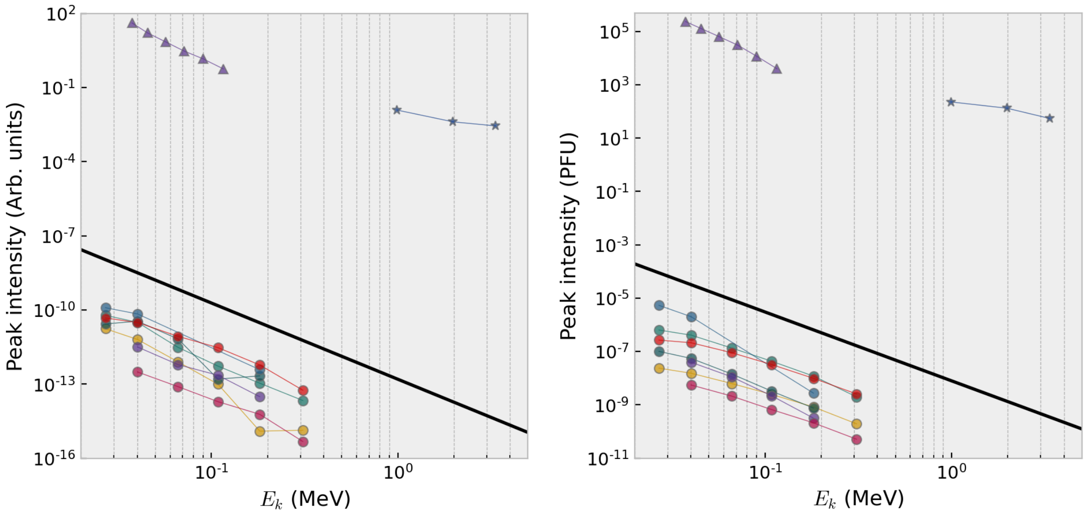

Figure 5.4: The electron energy spectrum is calculated using the peak flux of the Reid-Axford injection profile (left) in arbitrary units and observed peaks (right) in PFU as a function of energy. The average spectral index for the Reid-Axford injection profile and the observed intensity at 1.0 AU is approximately $\delta_{Sun} = -3.1$ and $\delta_{Earth} = -2.6$ respectively.

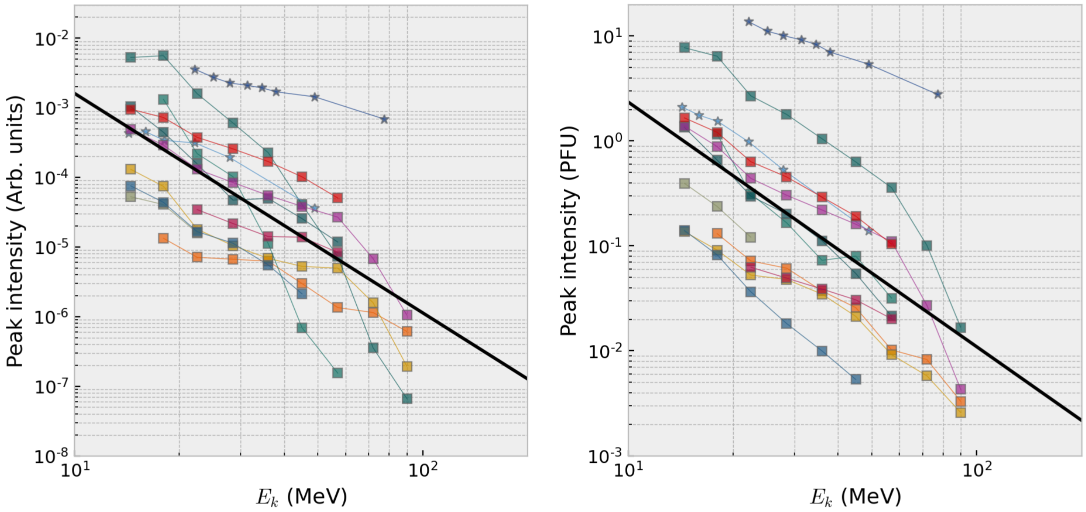

Figure 5.5: The proton peak flux energy spectrum as a function of energy for the Reid-Axford injection (left) in arbitrary units and observations (right) in PFU. The average spectral indices for the Reid-Axford model and the observations at 1.0 AU are $\delta_{Sun} = -3.2$ and $\delta_{Earth} = -2.3$, respectively.

almost the same power law seen in the electrons. However, the observed spectrum does become somewhat harder during transport.

5.4 Radial Dependence

The question arises whether there is a relation between the radial distance and level of scattering that might influence the parallel MFP. When comparing the various simulations for the components of λ and how they respond to changing conditions (such as the solar cycle), Engelbrecht and Moloto (2021) noted a radial distance dependence for $\lambda_\parallel$. It was found that the parallel MFP increases with radial distance.

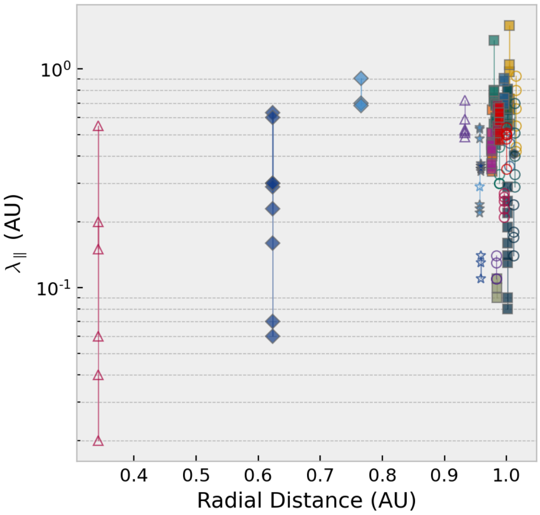

Figure 5.6: The parallel MFP results as a function of the radial distance from the Sun.

Figure 5.6 confirms these sentiments, while the Solar Orbiter data at ≈ 0.35 AU for the 21 March 2022 event (purple-red △) has a large range of MFP values, the range for this event are lower than the range for the PSP data at ≈ 0.62 AU for the 28 October 2021 event (Marian blue ◇). There is a slight trend where these ranges keep increasing with increasing radial distance, specifically in terms of the upper limit on the MFP values.

Given that the Reid-Axford time profile is defined for the inner boundary where $s = s_0$ at the Sun, there should not be any influence on the distance in the profile and thus its components. Figure 5.7 illustrates the acceleration (left panel) and escape (right panel) times for all the events at different radial distances. Without additional data, it is difficult to ascertain whether there are any trends in this comparison.

5.5 Magnetic Connection

With much emphasis placed on the importance of getting a magnetically well-connected measurement of a SEP event, it seems necessary to explore whether that connection displays an impact on the unobservable times. It is worth noting that the coordinate values provided for each event in Appendix A, and used in this investigation are not exact, and

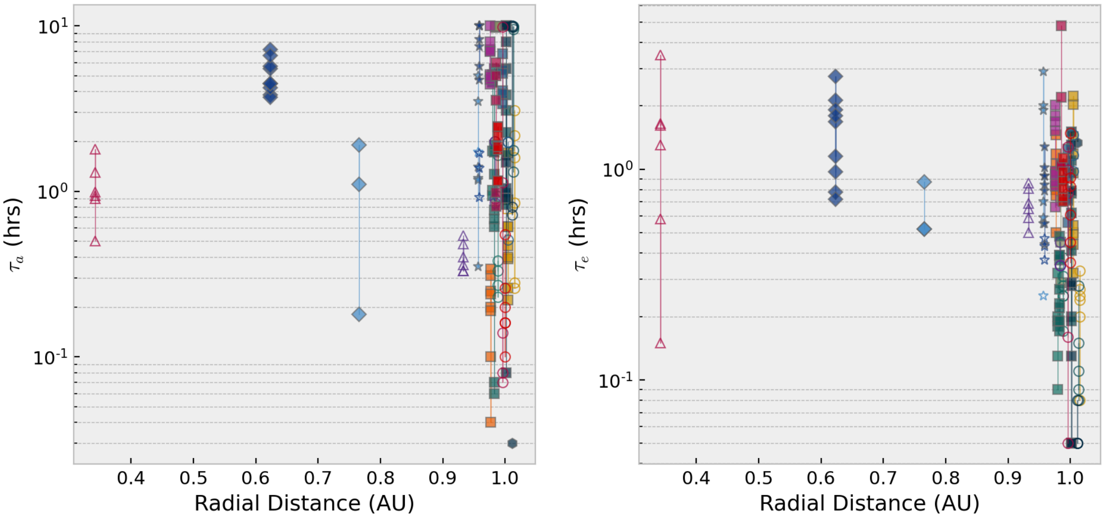

Figure 5.7: The acceleration (left) and escape (right) time results as a function of radial distance from the Sun.

should not be taken as such. The values found are taken to be the best scientific estimate of the true value assuming, for instance, a constant solar wind speed and Parker HMF. The acceleration and escape times compared to their magnetic connection are given in Figure 5.8.

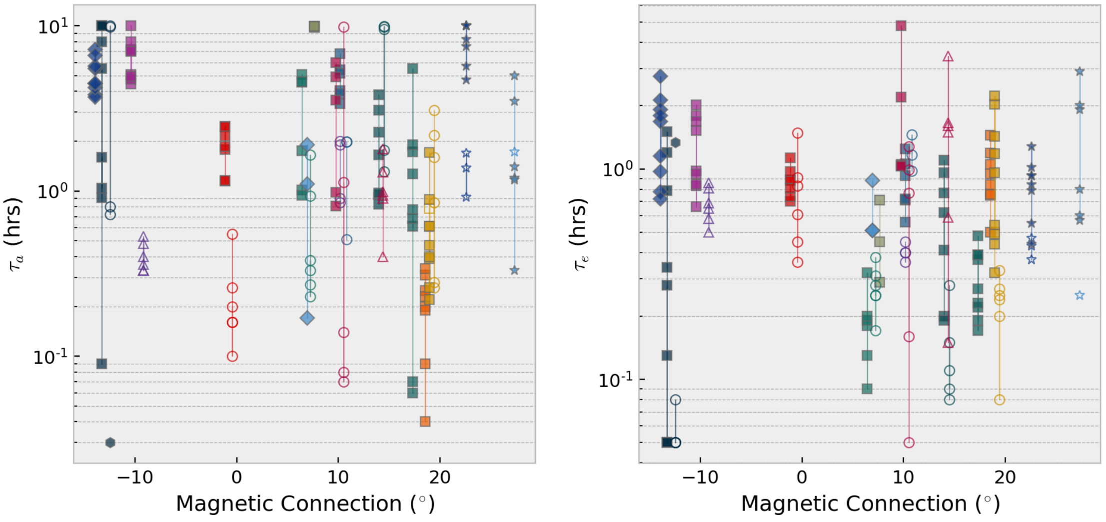

Figure 5.8: The injection times compared to the corresponding magnetic connection of the SEP event. The acceleration time is in the left panel, and the escape time is in the right panel.

Using the theory put forth by Reid (1964) that the acceleration time is the time taken for the particles to accelerate towards the tube of force, this would result in a shorter time for a closer distance to the source and longer time for a further distance to the source. While no trends stand out in Figure 5.8, the smallest τ_a values are not seen at the closest distance to the connections. The escape time (also referred to as the decay time) shows widespread results throughout the connections. More insight and data are required to determine whether the Reid-Axford times have a dependence on the magnetic connection.

5.6 Rigidity Dependence

5.6.1 Acceleration and Escape Times

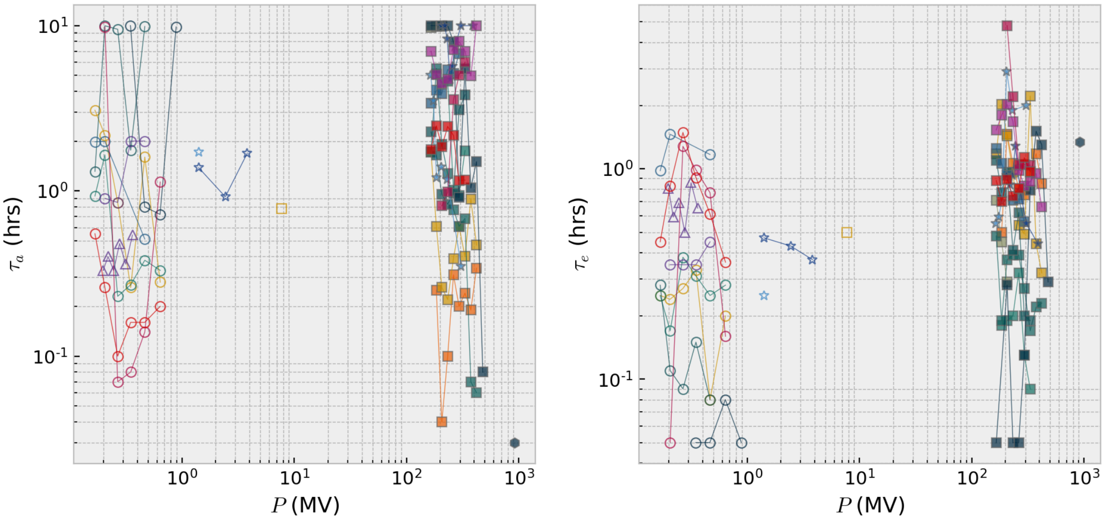

Figure 5.9: The acceleration (left) and escape (right) times as a function of rigidity.

If only Equation 3.2, the standard version of the Reid-Axford equation, is considered, then the units of the distribution function are contained almost entirely in the constant C as the exponent is unitless. Therefore, there is no reason for there to be any energy (or rigidity) dependence on the acceleration and escape times. However, the original equation by Reid (1964, Equation 3.3) includes a variable $a^2 = \frac{1}{3}v\lambda$, where the particle velocity v does depend on energy and rigidity (seen in Equation 2.4). While the conversion from Equation 3.3 to 3.2 is still unknown, there is potential for an energy dependence. The result of plotting all the τ_a and τ_e results as a function of their rigidities is seen in Figure 5.9. Isolating any of the events does not indicate a rigidity dependence at this time.

5.6.2 Parallel MFP

By following the data points in Figure 5.10 for each individual energy, a minimum $\lambda_\parallel$ is visible for each event. By following the gold circles and squares (11 June 1999 - WIND and SOHO) this minimum is $\lambda_\parallel$ = 0.4 AU and for the red markers (2 April 2022) it is about $\lambda_\parallel$ = 0.35 AU. This minimum potentially indicates the lowest MFP value possible

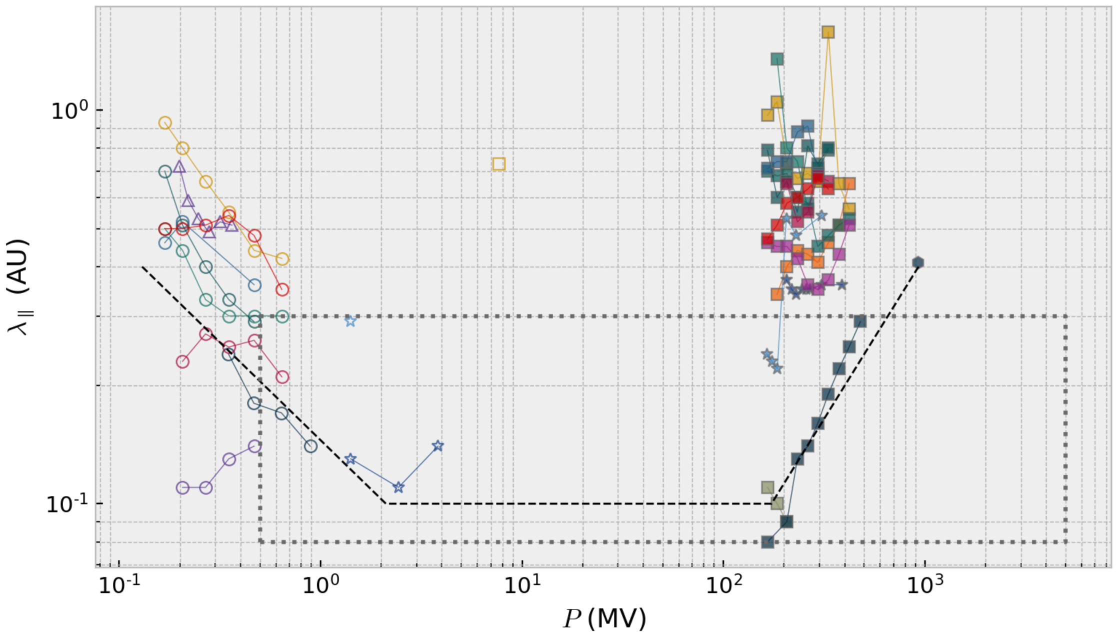

Figure 5.10: The results of the parallel MFP as a function of rigidity from the events fitted in Appendix A. Only results for a radial distance of $r \approx 1$ AU were used. Note that the two species, electrons (left) and protons (right), are separated with a wide rigidity gap of $P \approx 10 - 100$ MV. The dashed line resembling a valley shape indicates the trend found in Dröge (2000), and the box made of dotted lines indicates the Palmer (1982) consensus, both of which are discussed in Section 5.7.

for that event; the MFP of the electrons decreases to this value (with increasing rigidity) and the MFP of the protons increase from this value.

5.7 Historical Estimates

5.7.1 Dröge

Following the same procedure discussed in Chapters 3 and 4, including the use of the 1D transport model and Reid-Axford Injection, Dröge (2000) finds a similar set of free parameters as a function of energy.

All the results (Dröge, 2000, and references therein) collectively indicate a trend, seen in Figure 5.11, where for increasing rigidity the electrons decrease to a minimum and the protons increase from that same minimum (Dröge, 2000). There is also notably a clear variation between the MFP values for each event (Dröge, 2000).

This valley shape seen in Figure 5.11 is inserted into Figure 5.10 to compare the patterns

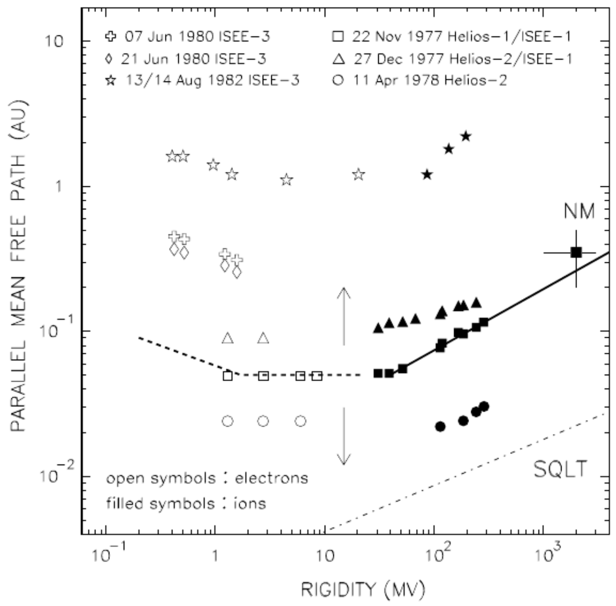

Figure 5.11: Figure, taken from Dröge (2000), depicting Dröge's results for the parallel MFP as a function of rigidity.

seen by Dröge (2000) and the trend discussed in Section 5.6.2. The 11 June 1999 and 14 August 2010 electron events measured by WIND (the gold and midnight green ○) follow this pattern and only differ by 0.15 AU. In terms of the protons, the 20 September 2015 and 2 April 2022 SOHO proton events (the medium blue and red □) show a steady increase and have a difference of 0.2 AU between them.

Given that the results of Dröge (2000) were from events recorded in the 1970s and 1980s there is an uncertainty in the continuity of the observations from different spacecraft. Plotting dozens of events using the same six magnetically connected spacecraft with the same SEP propagation model, as is done here, reduces that uncertainty significantly and still confirms the valley trend.

5.7.2 Palmer

The 'Palmer Consensus', defined by Palmer (1982), is a range of parallel MFP values within a rigidity range found by simulating particle transport for various cosmic rays (Engelbrecht et al., 2022). The consensus, seen as the dotted rectangle in Figure 5.10, does not discern between electrons and protons for rigidities from $P = 5 \times 10^{-4}$ GV to $P = 5$ GV (Palmer, 1982; Engelbrecht et al., 2022). This range, $\lambda_{\parallel} = 0.08 - 0.3$ AU, was defined using results from the 1970s, which were adjusted to standardise the results between the various models (Palmer, 1982).

This theory is revisited twice by Bieber et al. (1994) and Engelbrecht et al. (2022), both of whom were not able to recreate the same consensus with new data. Engelbrecht et al. (2022) described the consensus, having been derived from multiple results, as being unrealistic in that it included studies that neglected processes like convection and extended particle injection at the Sun which are known to influence particle transport. Bieber et al. (1994) note that only their lower-limit estimates of the parallel MFP appear to compare well with these consensus values.

Considering the MFP results found in this project as a function of rigidity in Figure 5.10, most of the data points fell outside of this consensus range.

5.8 Analytical Estimates of Theories

Bieber et al. (1994) hypothesized that the rigidity dependence on parallel MFPs appears to be different for electrons and protons. At lower rigidities the speed differences are larger, while at higher rigidities the particles are all relativistic (Bieber et al., 1994). With this understanding, a dynamical turbulence theory is postulated that includes two different assumptions of how particles resonate with turbulence: **r**andom **s**weeping (RS) and **d**amping **t**urbulence (DT) (Bieber et al., 1994; Teufel and Schlickeiser, 2002, 2003).

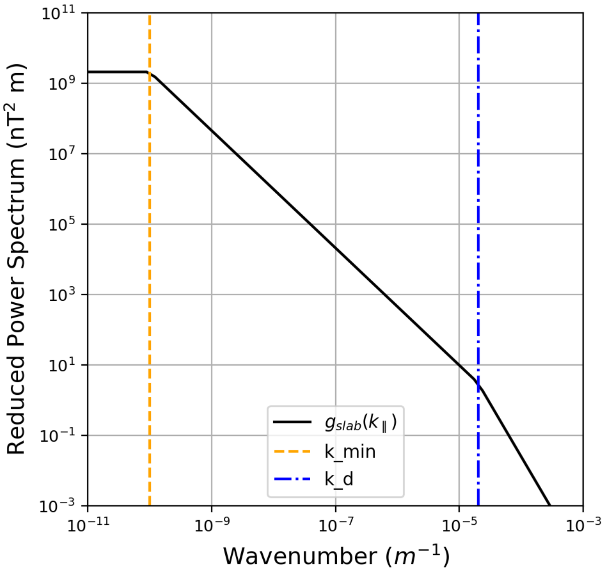

Figure 5.12: The reduced power spectrum recreated from Teufel and Schlickeiser (2002), Bieber et al. (1994), and Dröge (2003)

These two models were based on the power spectrum of the slab turbulence model seen in Figure 5.12 that consists of the piecewise function defined in Engelbrecht and Burger

(2013) to be

$$g_{slab}(k_\parallel) = \begin{cases} g_0\ k_{min}^{-s}, & \text{for } |k_\parallel| \leq k_m; \\ g_0\ |k_\parallel|^{-s}, & \text{for } k_m \leq |k_\parallel| \leq k_d; \\ g_0\ k_d^{p-s}\ |k_\parallel|^{-p}, & \text{for } |k_\parallel| \geq k_d, \end{cases} \tag{5.1}$$

where

$$g_0 = \left[s + \frac{s-p}{p-1} \left(\frac{k_{min}}{k_d} \right)^{s-1} \right]^{-1} \frac{\delta B_{slab}^2\ k_{min}^{s-1}\ (s-1)}{8\pi}. \tag{5.2}$$

The spectrum utilises $k_\parallel$ as the wavenumber with the two breaks in the spectrum at $k_{min} = 10^{-10}\ \text{m}^{-1}$ and $k_d = 2 \times 10^{-5}\ \text{m}^{-1}$. These three parts of the piecewise function correspond to the three divisions in Dröge's curve. The outcome of the models are expressions for the parallel MFP as a function of rigidity for electrons and protons separately. The expression for the parallel MFP in the RS model is given in Engelbrecht and Burger (2013) as

$$\begin{aligned} \lambda_\parallel = & \frac{3s}{\sqrt{\pi}(s-1)} \frac{R^2}{k_{min} b} \left(\frac{B_0}{\delta B_{slab}} \right)^2 \\ & \cdot \left[\frac{b}{4\sqrt{\pi}} + \left(\frac{1}{\Gamma(p/2)} + \frac{1}{\sqrt{\pi}(p-2)} \right) \frac{b^{p-1}}{Q^{p-s} R^s} + \frac{2}{\sqrt{\pi}(2-s)(4-s)} \frac{b}{R^s} \right], \end{aligned} \tag{5.3}$$

where the spectral indices are given as $s = 5/3$ and $p = 3$, $R^2 = R_L \cdot k_{min}$, $R_L = P/B_0$ is the Larmor radius, Γ is the Gamma function, $b = a/2$ where $a = \frac{v}{\alpha_d V_A}$, the background magnetic field strength at Earth is $B_0 = 4.12$ nT, the slab magnetic field is $(\delta B_{slab})^2 = 13.2\ \text{nT}^2$, and lastly, $Q = R_L \cdot k_d$. The minimum wavenumber k_{min} corresponds to the first change in slope in Figure 5.12 as shown by the orange dashed line, while k_d indicates the second slope change in blue. All values and relations used to calculate the RS and DT functions are found in Bieber et al. (1994); Engelbrecht and Burger (2013) and Engelbrecht (2008).

Alternatively, the expression in the DT model for the parallel MFP, modified from Engelbrecht and Burger (2013), is given as

$$\begin{aligned} \lambda_\parallel = & \frac{3s}{(s-1)} \frac{R^2}{k_{min} \cdot a} \left(\frac{B_0}{\delta B_{slab}} \right)^2 \\ & \cdot \left[\frac{a}{4\pi} +_2 F_1 \left(1; \frac{1}{p-1}; \frac{p}{p-1}; -\frac{\pi a}{f_1 Q} \right) \frac{a^2}{f_1 R^s Q^{3-s}} + \frac{2}{\pi(2-s)(4-s)} \frac{a}{R^s} \right] \\ & \text{where } f_1 = \frac{2}{p-2} + \frac{2}{2-s}, \end{aligned} \tag{5.4}$$

where ${}_2F_1(a, b, c; z)$ is the Gauss hypergeometric function that can be calculated using the `hyp2f1(a,b,c,z)` SciPy function (Virtanen et al., 2020). Note that for the proton $\lambda_\parallel$, the second term in the square brackets falls away in both Equations 5.3 and 5.4. Both equations do produce separate results for electrons at lower rigidities but merge at approximately $P = 2 \times 10^2$ MV.

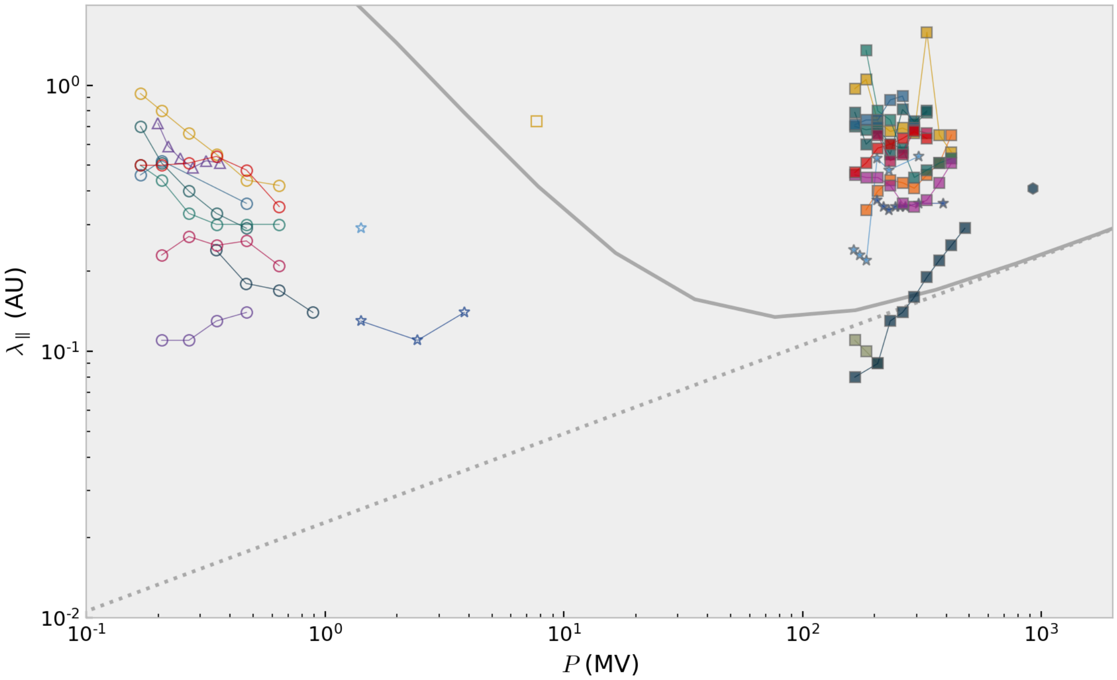

Figure 5.13: The random sweeping MFP from Teufel and Schlickeiser (2002), as expressed by Engelbrecht and Burger (2013), compared to the $\lambda_{\parallel}$ results of this project.

Figure 5.13 shows the comparison of the $\lambda_{\parallel}$ results from this project alongside the RS MFP. There exists only one instance of overlap between the data and the RS function and that is with the SOHO 17 May 2012 data (Prussian blue □) at $P \approx 300$ MV. The majority of the fitting results are not consistent with the RS function using the turbulence values from Bieber et al. (1994) and it seems unlikely to fit if there is an attempt to adjust the RS model parameters.

Figure 5.14 displays two intersections between the data and the DT model. It can be seen that by updating the 1.0 AU parameters from Bieber et al. (1994), it might be possible that the slope of the electron MFP function will increase enough to fit more event results.

Many of the values used to calculate the RS and DT functions are taken from Bieber et al. (1994) who calculated the standard conditions at 1.0 AU almost three decades before this project. There is a need to confirm that these values are still representative of the conditions at 1.0 AU with the use of modern data. Updating these conditions should not show a major impact on the final result of the model.

5.9 Summary and Conclusion

Using the results of fitting several events, this chapter compares various aspects of those results to find trends and gain insight into the propagation of SEPs. It starts with exploring

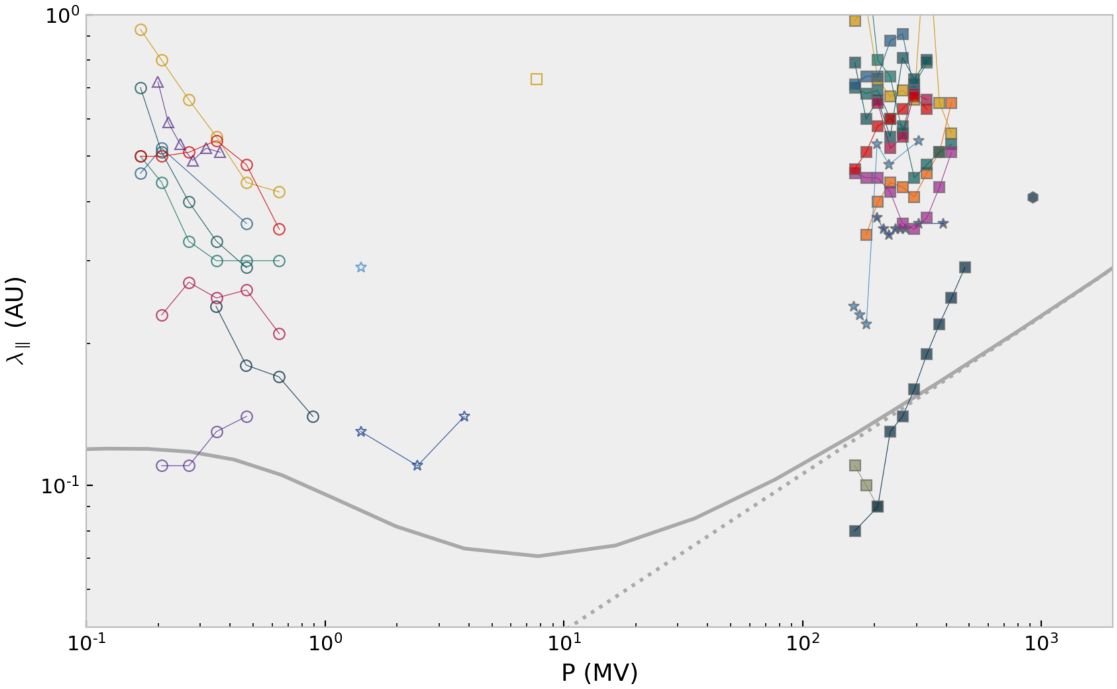

Figure 5.14: The parallel MFP results of this project compared to the dynamical turbulence MFP from Teufel and Schlickeiser (2002), as expressed by Engelbrecht and Burger (2013).

the changes in the 11- and 22-year solar cycles if the changing properties are connected to the unobservable parameters. The gaps in time during solar minimum meant that only solar maximum trends could be compared. The MFP results follow the rise and decay for SC23 as well as the lower, plateaued solar maximum for SC24 with the 17 May 2012 event. The acceleration time shows a possible moderate dependence during SC23 but this is not seen for the other solar cycles. The escape time requires more data to determine if there is a visible trend.

The energy spectrum at the Sun and 1.0 AU is then discussed, using the measured peak intensities from the observers at 1.0 AU and the calculated injection of particles at the Sun with the Reid-Axford time profile. The spectral indices for almost all the spectra are calculated to be $\delta \approx -3$, with the injected spectral index being slightly softer than the observed index.

A radial dependence is seen in the MFP but, because τ_a and τ_e should be independent of radial distance, there is no radial dependence seen for the acceleration and escape times. The parallel MFP shows an increasing average value for increasing radial distance.

The acceleration and escape times, with respect to the magnetic connection between the observing instrument and the flare site, show that the closest connections did not have the smallest τ_a values as expected based on the process described by Reid (1964). However, no further trends can be identified without more data and insight.

Comparing the acceleration and escape times to their respective rigidities does not indicate any dependence. The parallel MFP, however, shows a similar trend to what has been seen in Dröge (2000) where the profile of the electron to proton data creates a valley shape with increasing rigidity. As the rigidity increases the electrons' MFP decreases to a minimum that is different for each event, while the protons' MFP starts at that minimum and increases, causing the valley shape to form.

Most of these results did not agree with the Palmer consensus range, as seen in Figure 5.10, most likely due to these consensus values being derived from models that neglected fundamental processes and influences of SEP transport (as discussed in Engelbrecht et al., 2022).

The parallel MFP with respect to the rigidity shows a promising comparison to one of the dynamical turbulence models defined by Bieber et al. (1994) and Teufel and Schlickeiser (2002). The damping turbulence model shows a closer connection to the data that, with small fitting changes, should be very comparable.

With more data to bridge the gaps in the solar cycle, radial distances, magnetic connections, and rigidity comparisons, more defined trends should become visible.

Chapter 6

Summary and Conclusions

This research considered various potential trends in SEP transport parameters. These were found from the process of finding and fitting observations from instruments magnetically connected to the particle source.

Chapter 2 introduces a succinct interpretation of SEPs and their transport characteristics, starting with the environment they propagate through. This environment consists mainly of the HMF, forming the heliosphere, stemming from the Sun and being carried out by the solar wind, leading to the path for SEPs to travel along. This is followed by an introduction on the various cosmic rays, and how solar cosmic rays are accelerated by solar events such as solar flares and CMEs. Easing into the equations that make up particle transport, the focus is on the parallel MFP which requires the particle velocity and pitch-angle parameters. The chapter concludes with the FTE that is used in the 1D SEP transport model that is used in this dissertation.

Chapter 3 introduces the SEP transport model along with the parameters and assumptions required to use it. This includes how the model has been altered from the publically available version. These alterations include minor changes to the background values that are adjusted when normalising the simulated data. The Reid-Axford temporal profile is the injection function defined at the model's inner boundary, which adds two more unobservable parameters, namely acceleration and escape times. The R^2 goodness-of-fit statistic is used to guide the model simulations towards the best-fitting parameters, providing the result as a hypothetical percentage. A free parameter guide is created for electron and proton model simulations that indicate the influence each unobservable parameter has on the intensity of the SEPs over time. To test the fitting process, synthetic data is created using the model and incorporating noise. When finding the best fit, Figure 3.4 shows how the parameter values converge to the final result, where the top two best fits differed by only 8×10^{-5} is their R^2 statistic.

Chapter 4 illustrates the process of finding SEP events that correspond with the restrictions of the model with an example of fitting real observational data. JHelioviewer and Solar-MACH provide information on the flare and magnetic connections of the instruments for the GLE event on 28 October 2021. The time onset normalisation tool then confirms whether the observational data is objectively suitable for the fitting process, by discussing an example of when certain discontinuities leads to the full data set being manually discarded. Thereafter, the remainder of the data sets from STEREO-A and PSP that are fitted to model simulations for this event are reviewed using samples from each instrument. The chapter closes with hints of a possible radial dependency in the parallel MFP from the proton fitting results.

Chapter 5 uses the results of fitting several events (detailed in Appendix A) to explore various possible trends in SEP transport with a focus on the parallel MFP as a function of rigidity. Initially, a possible solar cycle dependence for both the 11- and 22-year solar cycles are considered, where Engelbrecht and Moloto (2021), Moloto and Engelbrecht (2020) and Chen and Bieber (1993) all note that $\lambda_{\|}$ displays a correlation to the solar cycle. There are no results presented in this dissertation that were recorded during solar minima periods so only solar maximum trends could be considered. Solar cycle 23 shows a moderate dependence for $\lambda_{\|}$ and τ_a but not τ_e. The MFP does follow the plateaued solar maximum for solar cycle 24, but further trends with any free parameter are inconclusive. The peak intensities derived from the Reid-Axford equation and the observational data allowed an energy spectra comparison from the particle injection at the flare to 1 AU. The resulting spectra are comparable with Strauss et al. (2020) where most results are approximately $\delta = -3$. The upper limit of the parallel MFP values shows a slight radial dependence from 0.3 – 1.0 AU which confirms the assumption from Dröge (2000), while the acceleration and escape times show no discernable trend. Given the emphasis on a magnetic connection in previous chapters, a brief inspection of its influence on τ_a and τ_e was necessary yet inconclusive without more insight and data. Finally, there is no clear rigidity dependence for the acceleration and escape times. However, the MFP results show a clear trend that agrees with the pattern noted by Dröge (2000), but not with the consensus discussed in Palmer (1982). This $\lambda_{\|}(P)$ result is further investigated alongside the analytical estimates initially derived by Bieber et al. (1994) and expanded on by Teufel and Schlickeiser (2002). Using the Bieber et al. (1994) input parameters for the analytical estimates, none of the analytical estimates compare well with the derived values of $\lambda_{\|}$. However, there is a promising comparison to the damping turbulence model that might be a better fit with updated model parameters. More defined trends should become discernable by fitting observational data that bridges the gaps and expands on the current boundaries in the solar cycle, radial distances, magnetic connections, and rigidity comparisons.

This dissertation serves as a guide to finding and fitting impulsive events with the 1D SEP transport model by van den Berg et al. (2020).

Appendix A

Results from Fitting Events

A.1 Solar Cycle 23

- 22 November 1998
- 11 June 1999
- 19 October 2001
- 1 November 2004

A.2 Solar Cycle 24

- 14 August 2010
- 17 May 2012 (GLE#71)
- 20 September 2015

A.3 Solar Cycle 25

- 9 October 2021
- 28 October 2021 (GLE#73)
- 18 January 2022
- 20 January 2022
- 15 February 2022
- 21 March 2022
- 2 April 2022

A.1 Solar Cycle 23

22 November 1998

22 November 1998 **10:00**		
Active region: 8384		
Flare: X3.7	(350; 28)	
Earth	0.988 AU	19°
SOHO	0.977 AU	19°

Table A.1: Event details drawn from Helioviewer and Solar-MACH for 22 November 1998.

Instrument	**Bin**	**Event Time**	E_k **(MeV)**	P **(MV)**	$\lambda_{\parallel}$ **(AU)**	τ_a **(hrs)**	τ_e **(hrs)**	R^2	**Norm.**	**Obs. Peak**
SOHO HET (p^+)	0	06:39	14.5	165.59	0.42	0.35	1.10	0.74	2.0e-4	2.0e-1
	1	06:42	18.0	184.67	0.34	0.25	0.50	0.84	1.3e-4	1.3e-1
	2	06:50	22.5	206.71	0.40	0.04	1.45	0.87	1.5e-5	7.2e-2
	3	06:50	28.5	233.01	0.43	0.09	1.05	0.89	1.9e-5	6.1e-2
	4	06:40	36.0	262.40	0.42	0.31	0.75	0.92	3.2e-5	3.7e-2
	5	06:44	45.0	294.06	0.41	0.20	0.76	0.95	1.4e-5	2.6e-2
	6	06:49	57.0	331.99	0.45	0.23	0.95	0.90	4.9e-6	1.0e-2
	7	06:49	72.0	374.57	0.51	0.19	1.19	0.95	3.2e-6	8.3e-3
	8	06:51	90.0	420.71	0.65	0.34	0.84	0.92	2.8e-6	3.3e-3
SOHO LED (e^-)	6	08:47	5.7	6.19	0.09	1.90	0.03	-0.06	7.6e2	1.4e0
	7	08:37	7.2	7.69	0.08	3.00	0.04	0.16	1.4e3	8.8e-1
	8	08:57	9.0	9.50	0.30	0.01	2.00	0.26	1.5e-5	7.3e-1

Table A.2: The results from fitting the 22 November 1998 event.

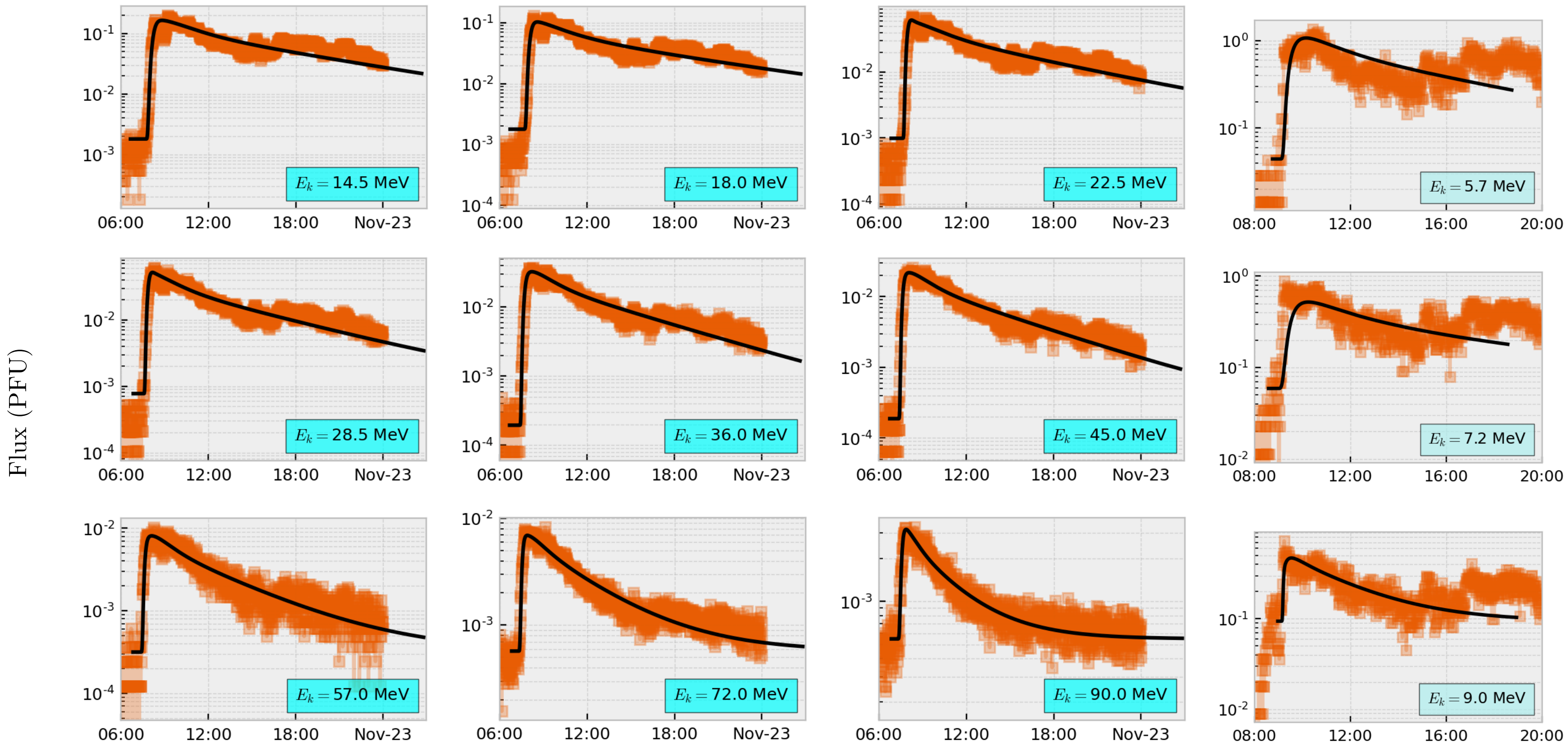

Figure A.1: The SOHO proton (first three columns) and electron (right column) results for 22 November 1998.

11 June 1999

11 June 1999 **01:00**		
Flare: C1.0	(225; -21)	
Earth	1.02 AU	19°
SOHO	1.00 AU	19°

Table A.3: Event details drawn from Helioviewer and Solar-MACH.

Instrument	**Bin**	**Event Time**	E_k **(MeV)**	P **(MV)**	$\lambda_\parallel$ **(AU)**	τ_a **(hrs)**	τ_e **(hrs)**	R^2	**Norm.**	**Obs. Peak**
SOHO HET (p^+)	0	00:28	14.5	165.59	0.97	1.71	1.18	0.95	1.7e-3	1.4e-1
	1	00:37	18.0	184.67	1.05	0.61	2.03	0.96	2.2e-4	9.1e-2
	2	00:42	22.5	206.71	0.73	0.26	1.43	0.96	4.7e-5	5.3e-2
	3	00:43	28.5	233.01	0.67	0.22	0.96	0.97	3.7e-5	4.8e-2
	4	00:41	36.0	262.40	0.69	0.39	0.54	0.97	6.5e-5	3.5e-2
	5	00:35	45.0	294.06	0.66	0.61	0.49	0.98	7.5e-5	2.1e-2
	6	00:45	57.0	331.99	1.58	0.40	2.22	0.88	1.2e-5	9.2e-3
	7	00:32	72.0	374.57	0.65	0.89	0.44	0.96	3.7e-5	5.8e-3
	8	00:33	90.0	420.71	0.56	0.47	0.32	0.89	7.0e-6	2.6e-3
SOHO LED (e^-)	5	02:38	4.5	4.98	0.28	4.90	0.14	0.79	3.7e+1	1.9e+0
	6	03:07	5.7	6.19	1.45	0.60	0.58	0.63	4.2e-3	1.3e+0
	7	02:57	7.2	7.70	0.73	0.78	0.50	0.81	2.2e-3	8.3e-1
	9	01:52	11.5	12.0	0.25	1.50	0.63	0.74	5.3e-4	2.8e-1
WIND 3DP (e^-)	0	00:05	0.03	0.17	0.93	3.07	0.25	0.94	2.0e-8	2.4e-8
	1	00:15	0.04	0.21	0.80	2.17	0.24	0.97	3.6e-9	1.5e-8
	2	00:26	0.07	0.27	0.66	0.85	0.27	0.99	7.5e-11	6.3e-9
	3	00:34	0.11	0.35	0.55	0.26	0.33	0.99	2.6e-12	2.4e-9
	4	00:28	0.18	0.47	0.44	1.60	0.08	0.99	1.6e-9	8.3e-10
	5	00:36	0.31	0.64	0.42	0.28	0.20	0.98	2.6e-13	1.9e-10
	6	00:35	0.52	0.89	0.74	1.38	0.14	0.80	7.0e-12	4.0e-11

Table A.4: The fitting results for 11 June 1999.

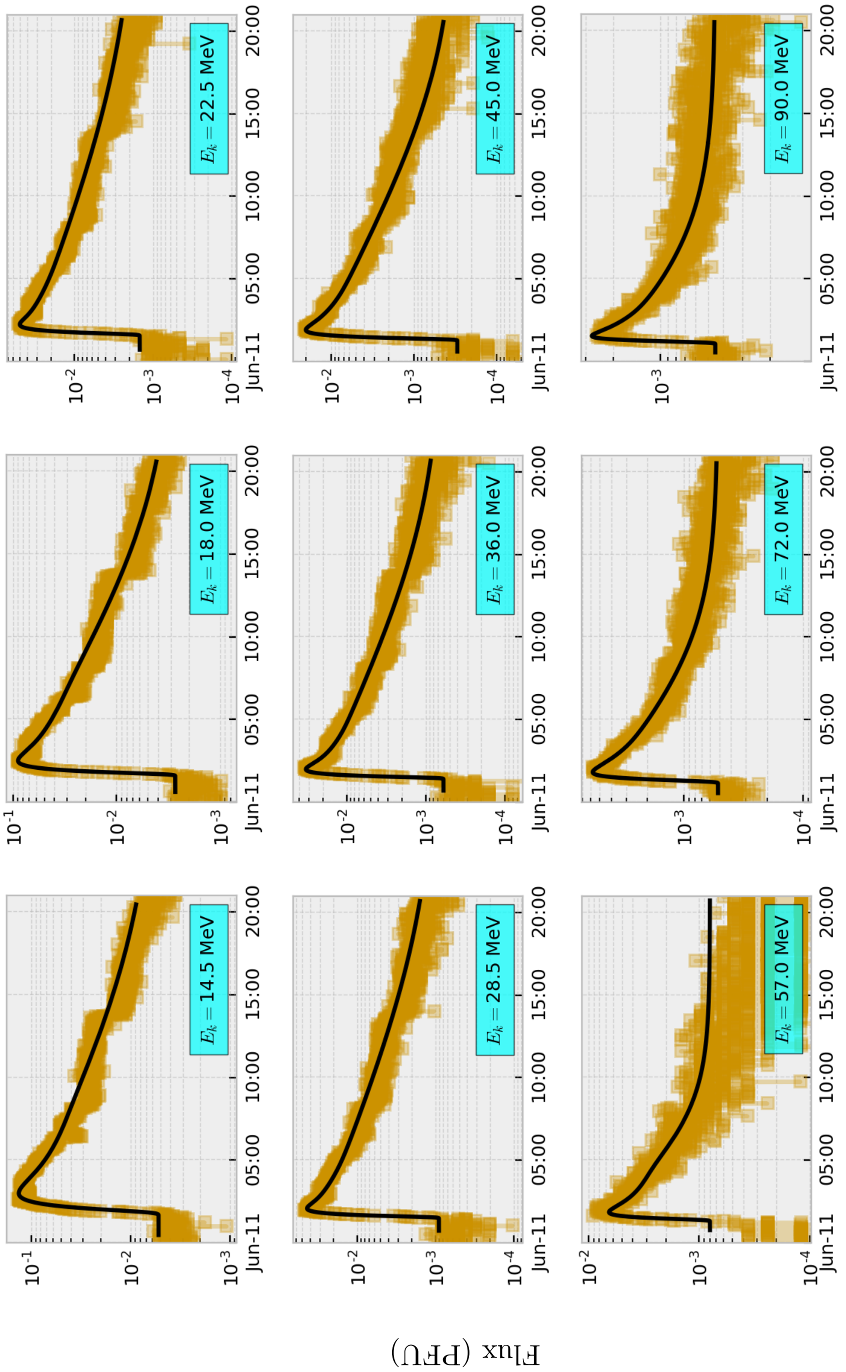

Figure A.2: The SOHO proton results for 11 June 1999.

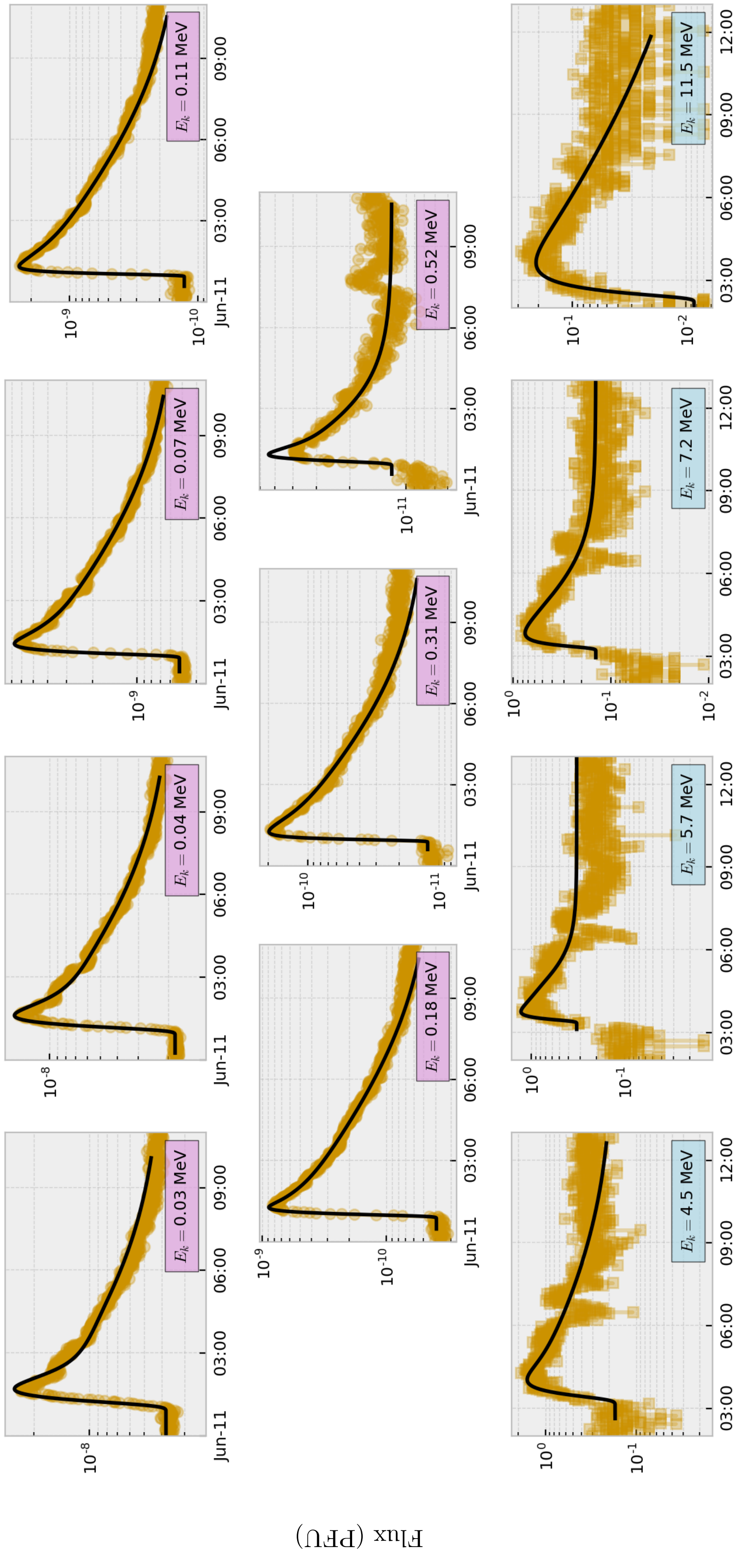

Figure A.3: The WIND (top) and SOHO (bottom) electron results for 11 June 1999.

19 October 2001

19 October 2001 **00:48**		
Active region: 9661		
Flare: X1.6	(28; -13)	
Earth	0.996 AU	8°
SOHO	0.985 AU	8°

Table A.5: Event details drawn from Helioviewer and Solar-MACH.

Instrument	**Bin**	**Event Time**	E_k **(MeV)**	P **(MV)**	$\lambda_\parallel$ **(AU)**	τ_a **(hrs)**	τ_e **(hrs)**	R^2	**Norm.**	**Obs. Peak**
SOHO HET (p^+)	0	00:38	14.5	165.6	0.11	9.75	0.71	0.82	2.3e-1	4.0e-1
	1	00:33	18.0	184.7	0.10	9.91	0.45	0.81	9.8e-1	2.4e-1
	2	00:42	22.5	206.7	0.09	9.89	0.29	0.80	4.5e+0	1.2e-1
	3	00:37	28.5	233.0	0.08	9.21	0.39	0.69	3.1e-1	7.6e-2
	4	00:48	36.0	262.4	0.07	9.78	0.16	0.67	7.1e+1	4.5e-2
	5	00:45	45.0	294.1	0.07	9.42	0.09	0.70	5.6e+3	2.8e-2
	6	00:52	57.0	332.0	0.07	9.16	0.04	0.76	5.2e+7	1.5e-2
	7	00:47	72.0	374.6	0.11	9.86	0.15	0.63	1.4e+1	5.8e-3

Table A.6: The fitting results for 19 October 2001.

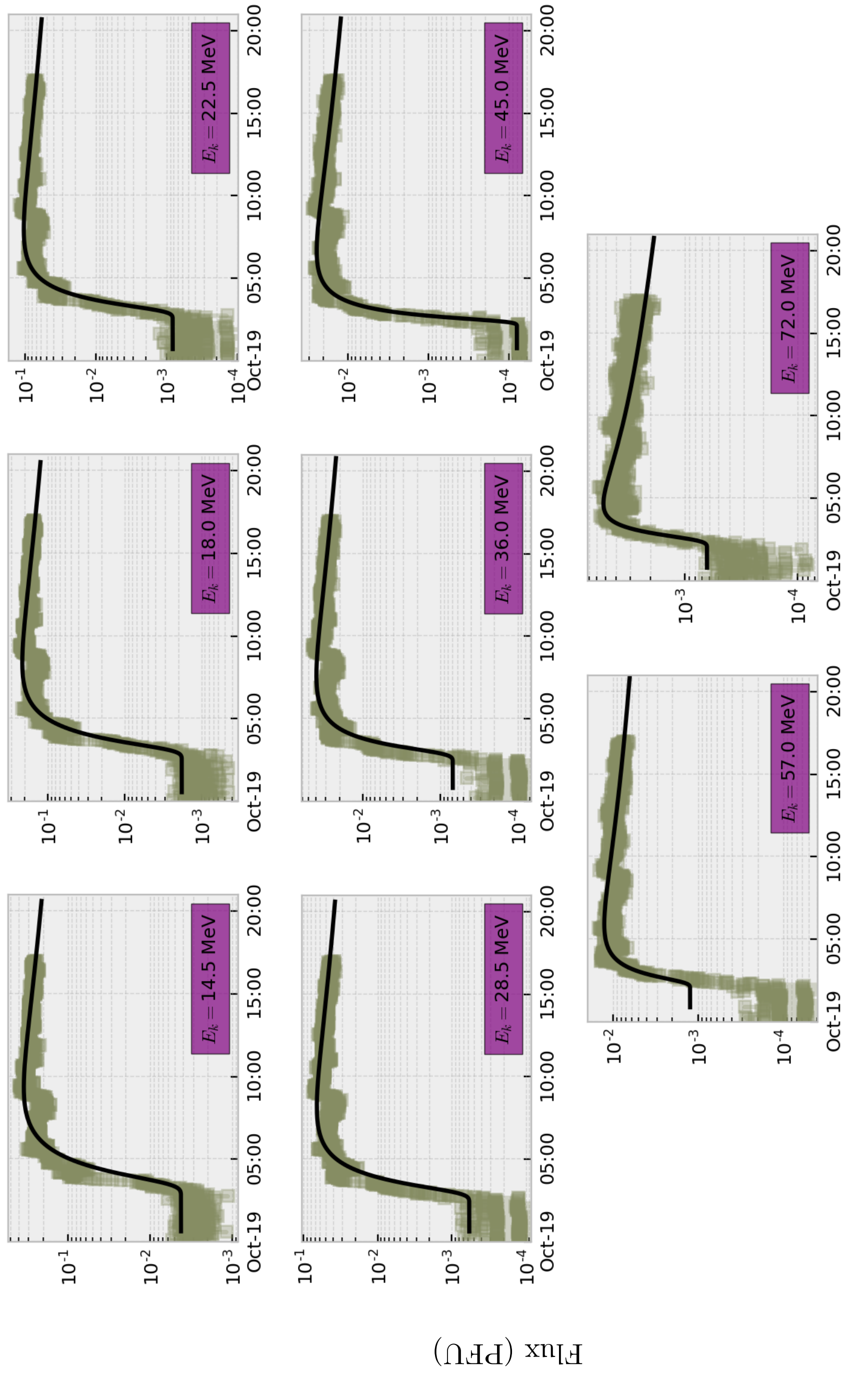

Figure A.4: The SOHO proton results for 19 October 2001.

20 February 2002

20 February 2002 **05:48**		
Active region: 9825 Flare: M5.1 (192; -11)		
Earth	0.989 AU	7°
SOHO	0.980 AU	6°

Table A.7: Event details drawn from Helioviewer and Solar-MACH.

Instrument	**Bin**	**Event Time**	E_k **(MeV)**	P **(MV)**	$\lambda_{\parallel}$ **(AU)**	τ_a **(hrs)**	τ_e **(hrs)**	R^2	**Norm.**	**Obs. Peak**
SOHO HET (p^+)	0	05:41	14.5	165.6	1.22	1.33	0.32	0.70	9.5e-2	2.3e+0
	1	05:30	18.0	184.7	1.35	5.08	0.18	0.80	5.5e+1	1.2e+0
	2	05:29	22.5	206.7	0.80	4.54	0.19	0.93	4.0e+0	3.1e-1
	3	05:30	28.5	233.0	0.74	4.60	0.20	0.93	1.5e+0	1.7e-1
	4	05:45	36.0	262.4	0.56	1.01	0.32	0.91	7.0e-4	7.3e-2
	5	05:54	45.0	294.1	0.71	0.94	0.13	0.89	3.9e-3	8.0e-2
	6	05:56	57.0	332.0	0.79	1.75	0.09	0.91	5.9e-2	3.2e-2
WIND 3DP (e^-)	0	05:27	0.03	0.17	0.50	0.93	0.25	0.81	8.3e-9	6.3e-7
	1	05:29	0.04	0.21	0.44	1.65	0.17	0.90	5.8e-8	4.1e-7
	2	05:42	0.07	0.27	0.33	0.23	0.38	0.86	5.3e-11	1.3e-7
	3	05:43	0.11	0.35	0.30	0.27	0.31	0.82	1.8e-11	4.3e-8
	4	05:45	0.18	0.47	0.30	0.38	0.25	0.84	8.6e-12	1.2e-8
	5	05:48	0.31	0.64	0.30	0.33	0.28	0.88	1.1e-12	2.0e-9
	6	06:03	0.52	0.89	0.18	0.02	0.01	0.60	2.0e-13	3.2e-10

Table A.8: The fitting results for 20 February 2002.

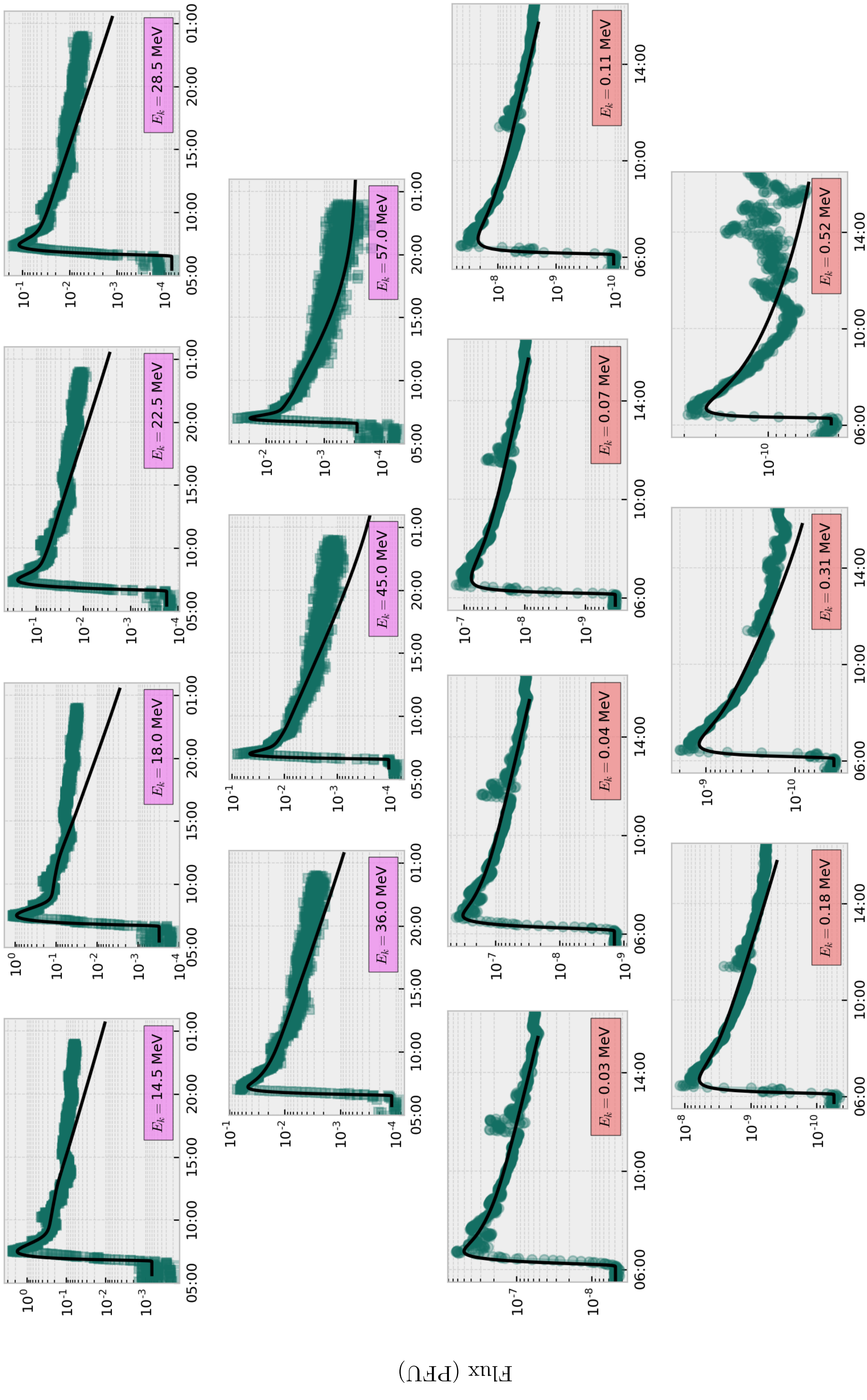

Figure A.5: The SOHO proton (top) and WIND electron (bottom) results for 20 February 2002.

1 November 2004

<table>
<tr><th colspan="3">1 November 2004
06:48</th></tr>
<tr><td colspan="3">Active region: 0687
Flare: C2.9 (138; 1)</td></tr>
<tr><td>Earth</td><td>0.992 AU</td><td>18°</td></tr>
<tr><td>SOHO</td><td>0.983 AU</td><td>17°</td></tr>
</table>

Table A.9: Event details drawn from Helioviewer and Solar-MACH.

Instrument	**Bin**	**Event Time**	E_k **(MeV)**	P **(MV)**	$\lambda_\parallel$ **(AU)**	τ_a **(hrs)**	τ_e **(hrs)**	R^2	**Norm.**	**Obs. Peak**
SOHO HET (p^+)	0	05:32	14.5	165.6	0.70	1.72	0.48	0.93	2.4e-1	7.7e+0
	1	05:23	18.0	184.7	0.68	5.50	0.19	0.96	2.6e+2	6.4e+0
	2	05:36	22.5	206.7	0.69	1.91	0.37	0.93	1.6e-1	2.7e+0
	3	05:42	28.5	233.0	0.60	1.27	0.39	0.94	2.8e-2	1.8e+0
	4	05:46	36.0	262.4	0.58	0.77	0.39	0.93	6.3e-3	1.1e+0
	5	05:48	45.0	294.1	0.45	0.61	0.27	0.96	3.0e-3	6.3e-1
	6	05:47	57.0	332.0	0.48	0.68	0.17	0.96	5.2e-3	3.6e-1
	7	05:52	72.0	374.6	0.51	0.07	0.22	0.97	3.6e-5	1.0e-1
	8	05:54	90.0	420.7	0.53	0.06	0.23	0.97	5.4e-6	1.7e-2
	9	06:03	115.0	478.6	2.04	0.11	0.59	0.37	1.2e-6	1.6e-3

Table A.10: The fitting results for 1 November 2004.

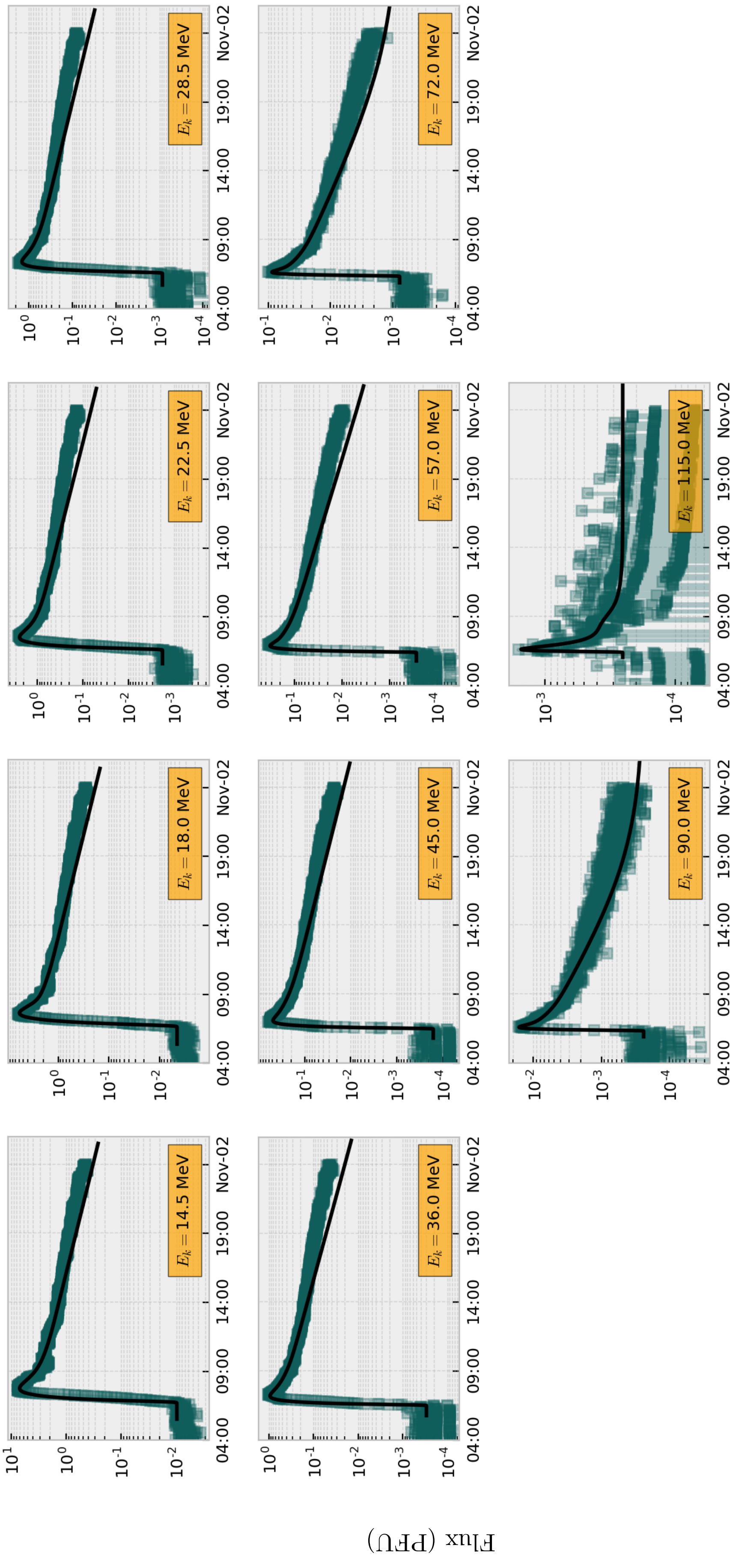

Figure A.6: The SOHO proton results for 1 November 2004.

A.2 Solar Cycle 24

14 August 2010

14 August 2010 **09:30**		
Active region: 1099		
Flare: C4.4	(345; 18)	
STEREO-A	0.962 AU	92°
Earth	1.01 AU	15°
SOHO	1.00 AU	14°

Table A.11: Event details drawn from Helioviewer and Solar-MACH.

Instrument	**Bin**	**Event Time**	E_k **(MeV)**	P **(MV)**	$\lambda_\parallel$ **(AU)**	τ_a **(hrs)**	τ_e **(hrs)**	R^2	**Norm.**	**Obs. Peak**
WIND 3DP (e^-)	0	09:42	0.03	0.17	0.70	1.31	0.28	0.85	3.6e-9	1.0e-7
	1	09:17	0.04	0.21	0.51	9.96	0.11	0.94	6.5e-3	5.5e-8
	2	09:23	0.07	0.27	0.40	9.49	0.09	0.95	5.9e-3	1.4e-8
	3	09:45	0.11	0.35	0.33	1.76	0.15	0.94	7.2e-10	3.3e-9
	4	09:26	0.18	0.47	0.29	9.86	0.08	0.91	1.1e-3	7.5e-10
	5	09:55	0.31	0.64	0.14	0.41	0.07	-0.33	1.5e-12	4.2e-10
	6	07:25	0.52	0.89	0.05	9.99	9.99	0.37	1.3e-14	6.9e-10
SOHO HET (p^+)	0	09:46	14.5	165.6	0.79	2.27	1.10	0.90	2.5e-2	1.4e+0
	1	09:51	18.0	184.7	0.60	1.65	0.77	0.90	8.5e-3	6.6e-1
	2	09:54	22.5	206.7	0.66	0.95	0.96	0.91	1.1e-3	3.0e-1
	3	10:00	28.5	233.0	0.55	0.83	0.41	0.90	1.2e-3	2.0e-1
	4	09:58	36.0	262.4	0.81	0.97	0.62	0.84	6.6e-4	1.1e-1
	5	09:52	45.0	294.1	0.73	3.08	0.20	0.88	8.3e-2	5.5e-2
	6	09:50	57.0	332.0	0.80	3.81	0.19	0.88	1.0e-1	2.1e-2

Table A.12: The fitting results for 14 August 2010.

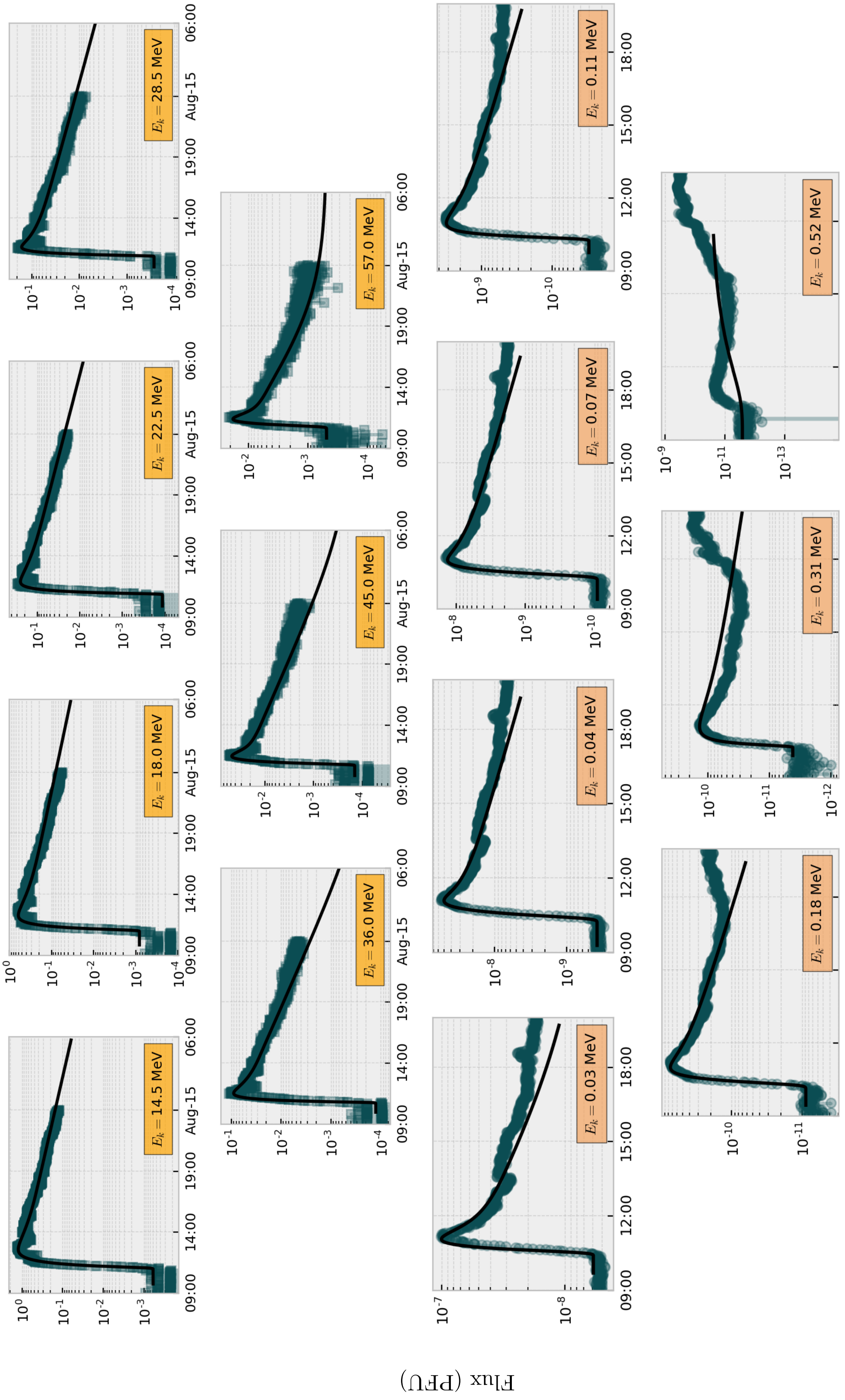

Figure A.7: The SOHO proton (top) and WIND electron (bottom) results for 14 August 2010.

17 May 2012: GLE 71

17 May 2012 **01:25**		
Active region: 1476 Flare: M5.1 (186; 11)		
STEREO-A	0.96 AU	98°
Earth	1.01 AU	-13°
SOHO	1.00 AU	-13°

Table A.13: Event details drawn from Helioviewer and Solar-MACH.

Instrument	**Bin**	**Event Time**	E_k **(MeV)**	P **(MV)**	$\lambda_\parallel$ **(AU)**	τ_a **(hrs)**	τ_e **(hrs)**	R^2	**Norm.**	**Obs. Peak**
WIND 3DP (e^-)	0	00:45	0.03	0.17	0.35	9.88	0.09	0.40	3.8e-1	4.7e-7
	1	00:54	0.04	0.21	0.32	9.81	0.06	0.59	2.7e+1	3.7e-7
	2	00:55	0.07	0.27	0.29	9.99	0.05	0.71	1.2e+2	1.4e-7
	3	00:58	0.11	0.35	0.24	9.99	0.05	0.83	3.0e+1	4.6e-8
	4	01:23	0.18	0.47	0.18	0.80	0.05	0.95	5.4e-9	1.3e-8
	5	01:24	0.31	0.64	0.17	0.72	0.08	0.97	1.5e-10	3.6e-9
	6	01:03	0.51	0.89	0.14	9.80	0.05	0.85	2.2e-1	4.0e-9
SOHO HET (p^+)	0	01:43	14.5	165.6	0.08	9.99	0.05	0.85	2.1e+89	1.9e+0
	1	02:09	18.0	184.7	0.09	2.43	0.05	0.69	5.3e+2	1.3e+0
	2	00:22	22.5	206.7	0.09	9.99	0.28	0.91	3.4e+1	6.6e-1
	3	02:01	28.5	233.0	0.13	9.97	0.05	0.90	5.7e+8	5.4e-1
	4	02:03	36.0	262.4	0.14	7.97	0.05	0.96	1.9e+7	3.9e-1
	5	02:23	45.0	294.1	0.16	0.91	0.13	0.98	1.6e-2	3.3e-1
	6	00:44	57.0	332.0	0.19	5.50	0.79	0.96	1.4e-2	2.4e-1
	7	01:07	72.0	374.6	0.22	1.04	1.51	0.96	7.3e-5	7.7e-2
	8	01:14	90.0	420.7	0.25	1.60	1.20	0.96	3.2e-5	1.7e-2
	9	01:36	115.0	478.6	0.30	0.09	0.34	0.95	1.3e-6	5.8e-3
GOES-15 (p^+)	8	01:56	375.0	918.8	0.41	0.03	1.34	0.81	1.1e-6	1.7e-2
	9	01:49	465.0	1,043.3	0.59	0.11	2.63	0.59	9.1e-7	7.7e-3
	10	01:46	605.0	1,225.2	0.26	0.80	0.05	0.63	1.1e-3	3.6e-3

Table A.14: The fitting results for 17 May 2012.

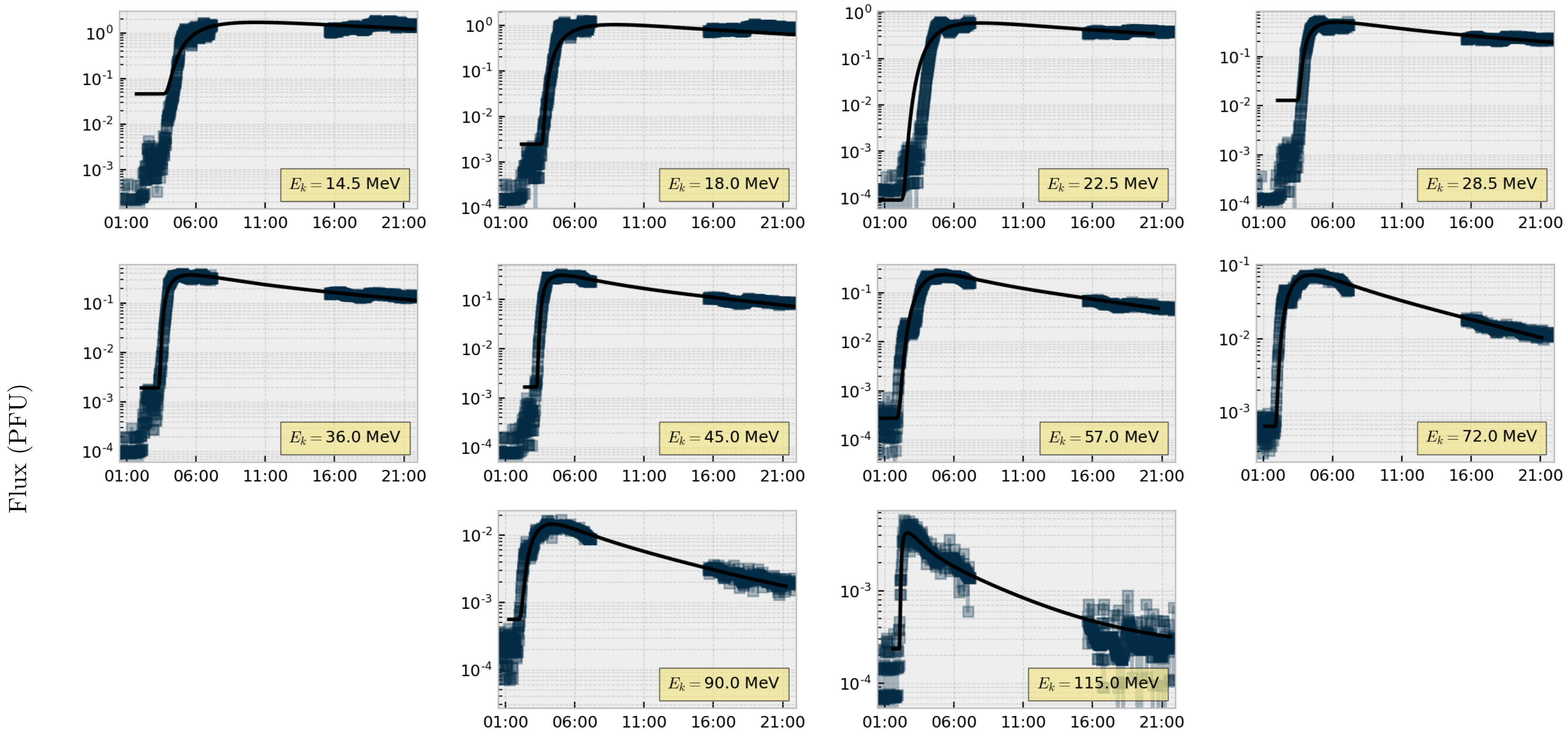

Figure A.8: The SOHO proton results for 17 May 2012.

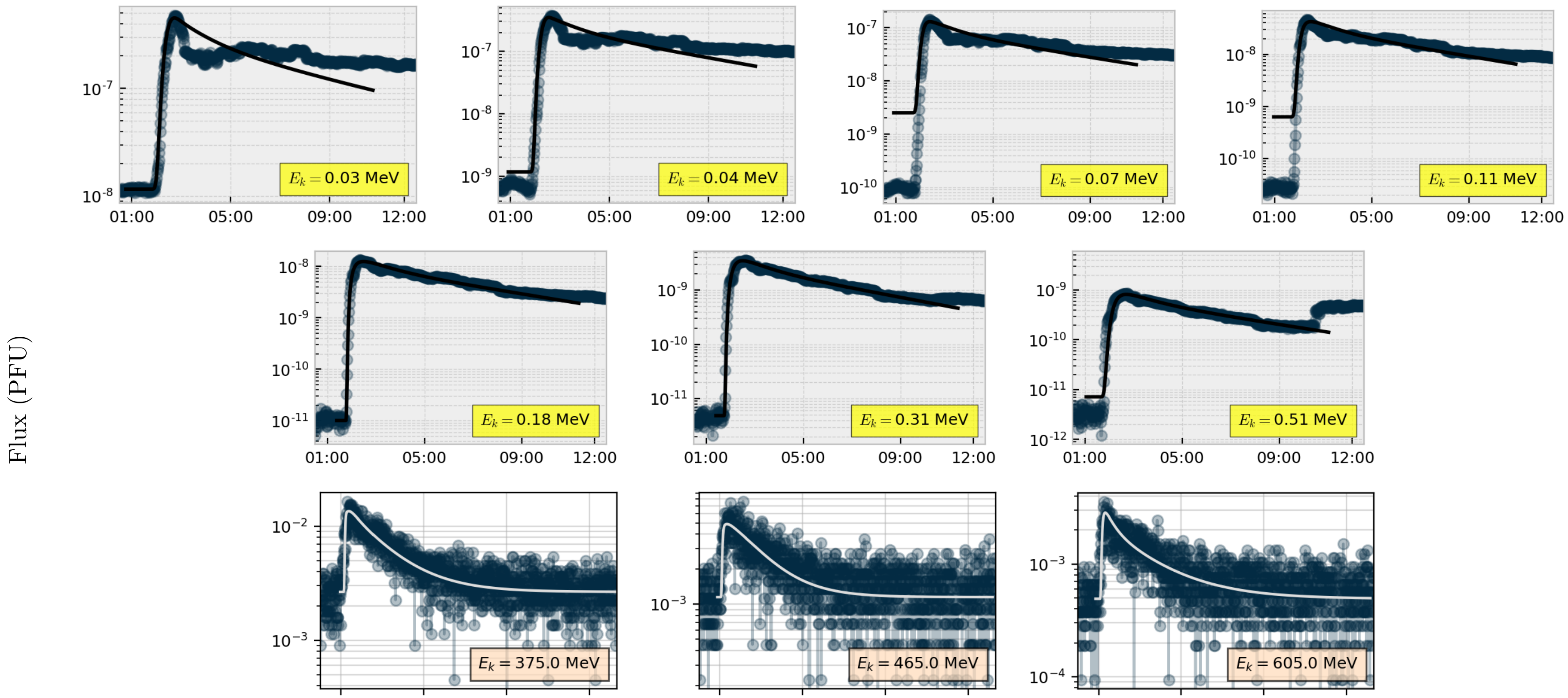

Figure A.9: The WIND electron (top) and GOES proton (bottom) results for 17 May 2012.

20 September 2015

20 September 2015 **18:00**		
Active region: 2415 Flare: M2.1 (234; -20)		
STEREO-A	0.965 AU	-162°
Earth	1.00 AU	11°
SOHO	0.996 AU	10°

Table A.15: Event details drawn from Helioviewer and Solar-MACH.

Instrument	**Bin**	**Event Time**	E_k **(MeV)**	P **(MV)**	$\lambda_\parallel$ **(AU)**	τ_a **(hrs)**	τ_e **(hrs)**	R^2	**Norm.**	**Obs. Peak**
WIND 3DP (e$^-$)	0	17:16	0.03	0.17	0.46	1.98	0.98	0.93	2.5e-9	5.3e-6
	1	17:08	0.04	0.21	0.52	1.99	1.46	0.97	9.9e-10	2.0e-6
	2	16:55	0.07	0.27	0.13	9.90	0.05	0.77	2.1e+1	6.1e-8
	4	17:42	0.18	0.47	0.36	0.51	1.17	0.94	1.5e-12	2.7e-9
	5	17:43	0.31	0.64	0.39	0.66	0.89	0.77	3.5e-13	1.1e-9
SOHO HET (p$^+$)	0	17:45	14.5	165.6	0.71	3.38	1.25	0.97	4.1e-3	1.4e-1
	1	17:41	18.0	184.7	0.74	4.06	1.06	0.98	4.4e-3	8.2e-2
	2	17:47	22.5	206.7	0.74	3.88	0.93	0.97	2.0e-3	3.7e-2
	3	17:47	28.5	233.0	0.88	5.41	0.71	0.95	5.7e-3	1.8e-2
	4	17:46	36.0	262.4	0.91	5.13	0.72	0.94	2.3e-3	1.0e-2
	5	17:28	45.0	294.1	0.69	6.76	0.56	0.92	4.4e-3	5.3e-3

Table A.16: The fitting results for 20 September 2015.

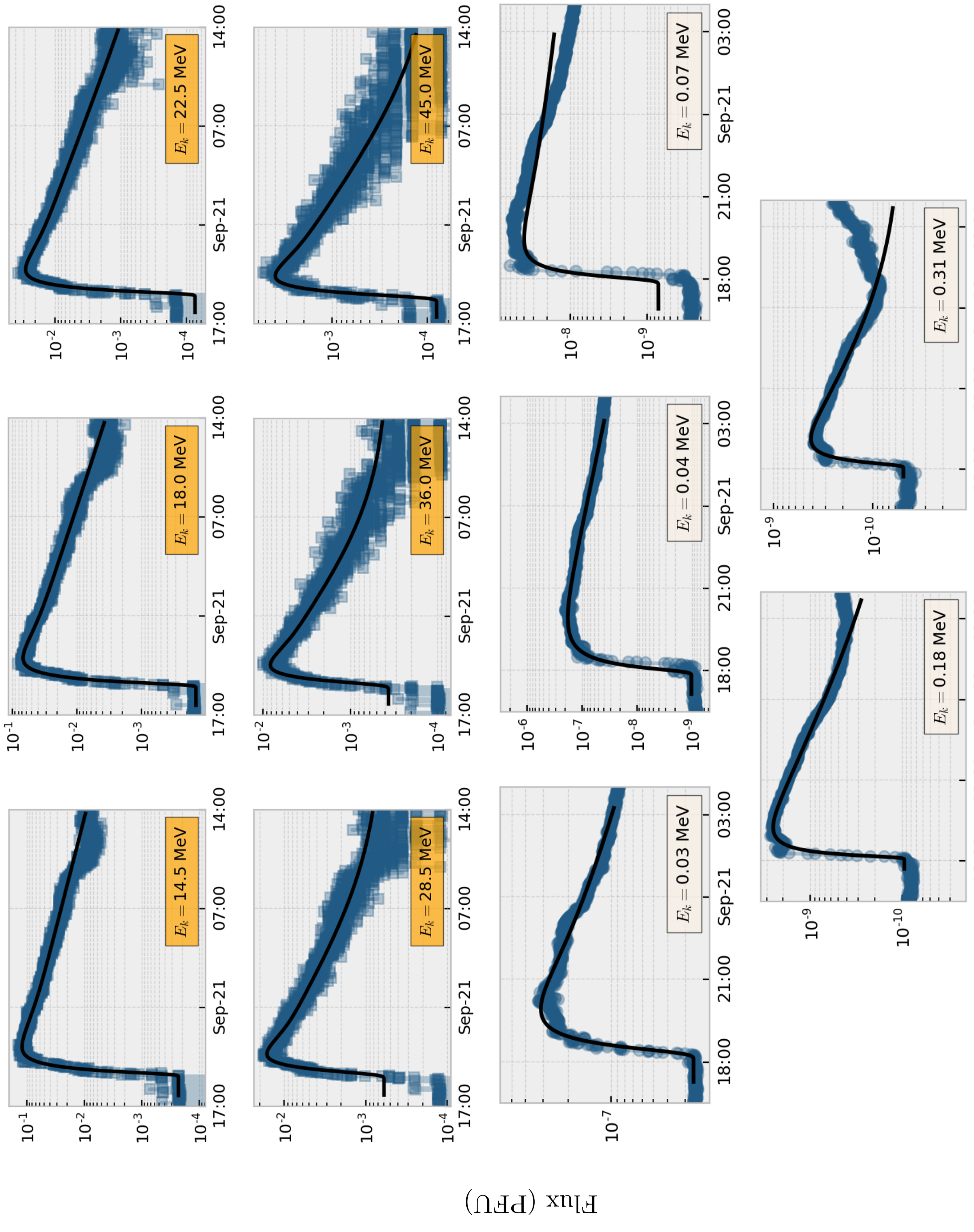

Figure A.10: The SOHO proton (top) and WIND electron (bottom) results for 20 September 2015.

A.3 Solar Cycle 25

9 October 2021

<table>
<tr><th colspan="3">9 October 2021
06:30</th></tr>
<tr><td colspan="3">Active region: 2882
Flare: M1.6 (159; 19)</td></tr>
<tr><td>STEREO-A</td><td>0.957 AU</td><td>-27°</td></tr>
<tr><td>Earth</td><td>0.999 AU</td><td>69°</td></tr>
<tr><td>SOHO</td><td>0.988 AU</td><td>68°</td></tr>
<tr><td>PSP</td><td>0.765 AU</td><td>7°</td></tr>
<tr><td>Solar Orbiter</td><td>0.679 AU</td><td>35°</td></tr>
</table>

Table A.17: Event details drawn from Helioviewer and Solar-MACH.

Instrument	Bin	Event Time	E_k (MeV)	P (MV)	$\lambda_\parallel$ (AU)	τ_a (hrs)	τ_e (hrs)	R^2	Norm.	Obs. Peak
PSP IS⊙IS (e$^-$)	1	06:48:00	0.55	0.92	0.95	0.25	2.00	0.56	1.1e-4	3.6e-1
	2	06:23:00	0.65	1.04	0.09	0.75	0.08	0.77	8.8e-3	7.2e-1
	3	06:31:00	0.77	1.18	0.10	0.03	0.60	0.77	1.0e-5	8.6e-1
	4	06:47:00	0.92	1.33	0.50	0.10	0.84	0.80	9.1e-5	8.3e-1
	5	06:39:00	1.09	1.52	0.25	0.15	0.74	0.75	3.4e-5	4.1e-1
PSP IS⊙IS (p$^+$)	2	06:53:00	10.4	139.9	0.70	0.17	0.88	0.81	4.2e-3	1.2e+1
	3	06:31:00	12.3	152.6	0.90	1.20	0.61	0.80	7.3e-2	1.2e+1
	4	06:28:00	14.7	166.6	0.89	1.70	0.52	0.80	9.5e-2	5.9e+0
	5	06:29:00	17.4	181.8	0.90	1.90	0.51	0.80	6.5e-2	2.9e+0
	6	06:38:00	20.7	198.4	0.68	1.10	0.51	0.84	9.6e-3	1.7e+0
	7	06:40:00	24.7	216.6	0.75	1.00	0.55	0.77	4.6e-3	1.1e+0
	8	06:40:00	29.3	236.5	0.48	0.95	0.42	0.72	2.4e-3	7.2e-1
	9	06:42:00	34.9	258.2	0.30	0.70	0.22	0.65	1.6e-3	4.2e-1
STEREO-A HET (e$^-$)	0	06:38:58	0.99	1.41	0.29	1.72	0.25	0.85	5.5e-2	2.5e+0
STEREO-A HET (p$^+$)	0	06:12:58	14.3	164.4	0.24	5.00	0.57	0.86	3.5e-1	2.1e+0
	1	06:19:58	16.0	174.0	0.23	3.50	0.60	0.85	7.9e-2	1.8e+0
	2	06:34:58	18.1	185.2	0.22	1.20	0.80	0.82	3.9e-3	1.5e+0
	3	06:43:58	22.2	205.3	0.53	1.40	2.90	0.85	1.8e-3	9.8e-1
	4	06:38:58	25.1	218.5	0.53	2.80	1.34	0.80	7.9e-3	7.5e-1
	5	06:48:58	27.9	230.5	0.48	1.17	1.91	0.80	1.0e-3	5.3e-1
	6	06:45:58	31.4	244.8	0.45	1.80	1.13	0.78	2.3e-3	4.7e-1
	7	06:49:58	34.6	257.2	0.55	1.10	2.00	0.74	6.0e-4	3.7e-1
	8	06:58:58	38.0	269.7	0.50	0.53	2.55	0.77	1.7e-4	2.4e-1
	9	06:59:58	49.0	307.2	0.53	0.33	2.00	0.90	8.1e-5	1.4e-1

Table A.18: The fitting results for 9 October 2021.

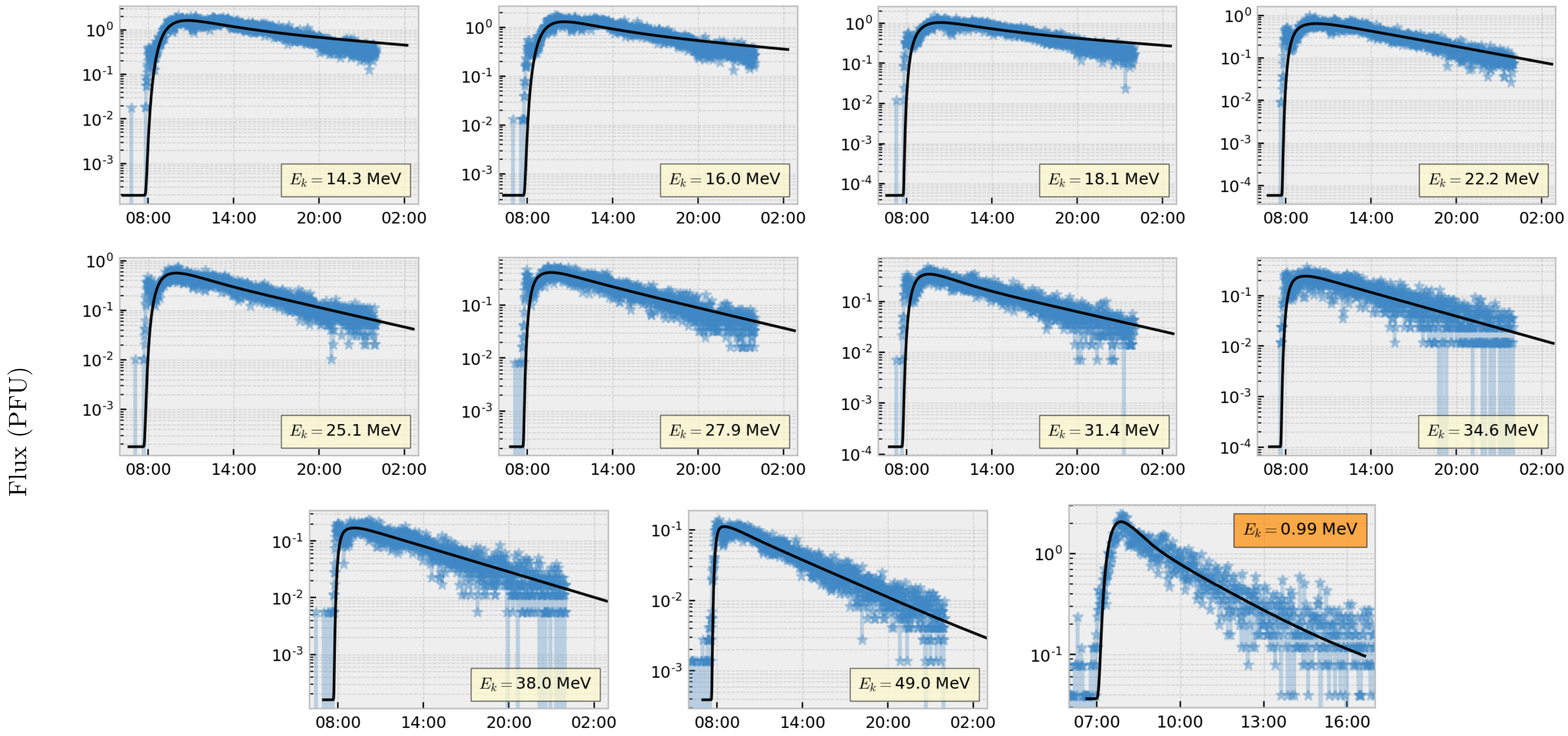

Figure A.11: The STEREO-A proton (light lemon box) and electron (orange box) results for 9 October 2021.

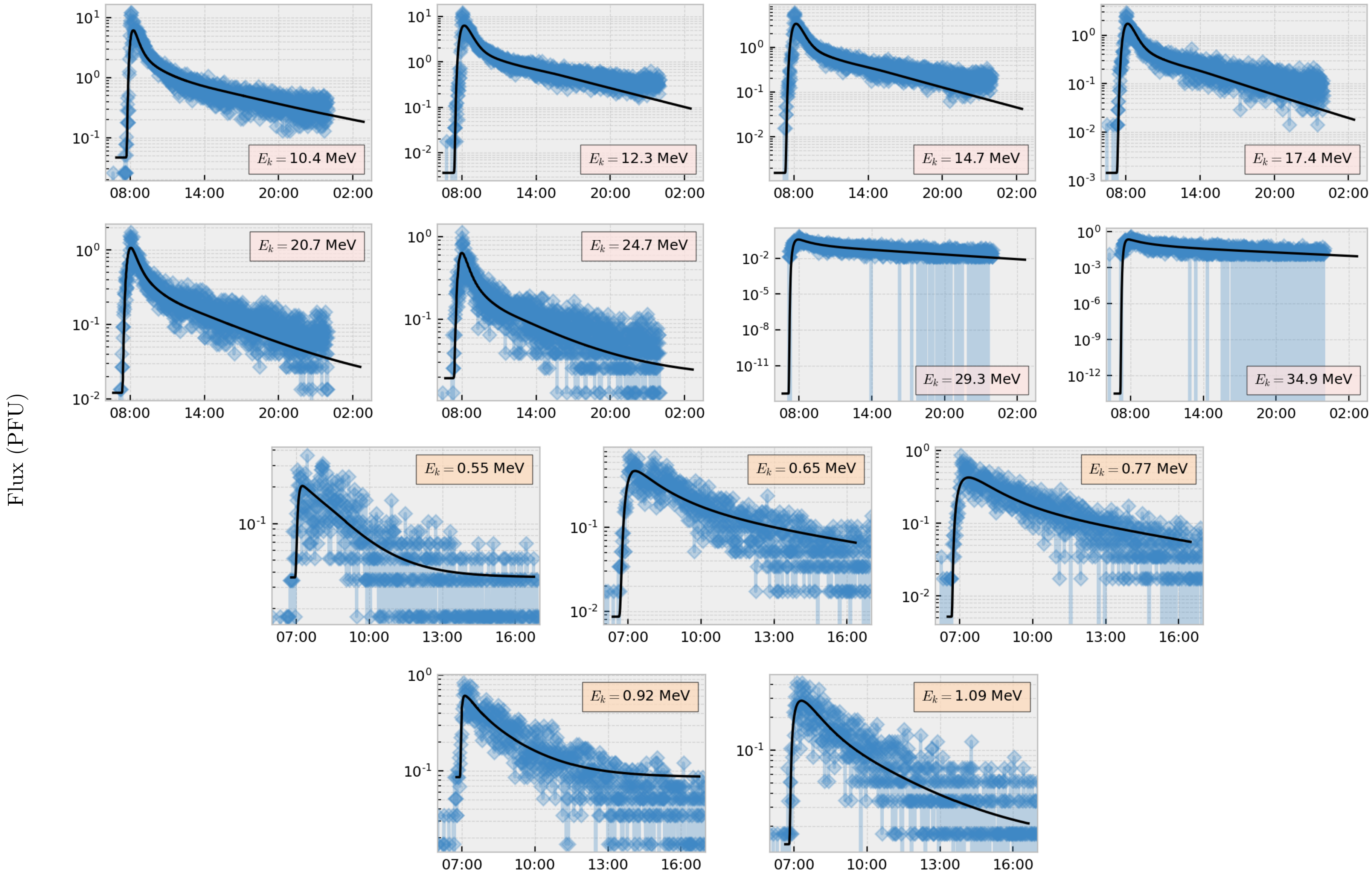

Figure A.12: The PSP proton (top) and electron (bottom) results for 9 October 2021.

28 October 2021: GLE 73

28 October 2021 **15:27**		
Active region: 2887 Flare: X1.0 (-270; -29)		
STEREO-A	0.959 AU	22°
Earth	0.993 AU	62°
SOHO	0.983 AU	62°
PSP	0.623 AU	-15°
Solar Orbiter	0.804 AU	48°

Table A.19: Event details drawn from Helioviewer and Solar-MACH.

Instrument	**Bin**	**Event Time**	E_k **(MeV)**	P **(MV)**	$\lambda_\parallel$ **(AU)**	τ_a **(hrs)**	τ_e **(hrs)**	R^2	**Norm.**	**Obs. Peak**
PSP IS⊙IS (p^+)	1	14:47:00	8.7	128.2	3.00	9.90	2.50	0.75	3.3e+2	7.2e+2
	2	14:18:00	10.4	139.9	0.08	9.69	0.82	0.78	2.5e+1	2.3e+2
	3	14:38:00	12.3	152.6	0.07	7.15	0.78	0.92	9.6e+0	2.0e+2
	4	14:49:00	14.7	166.6	0.06	3.83	0.72	0.87	1.1e+0	1.5e+2
	5	14:59:00	17.4	181.8	0.16	3.69	2.12	0.90	2.5e-1	1.1e+2
	6	15:01:00	20.7	198.4	0.30	4.22	2.76	0.91	3.9e-1	9.0e+1
	7	14:59:00	24.7	216.6	0.29	5.50	1.68	0.93	1.1e+0	8.2e+1
	8	15:04:00	29.3	236.5	0.63	5.71	1.92	0.94	2.1e+0	6.4e+1
	9	14:55:00	34.9	258.2	0.30	6.58	1.15	0.93	2.4e+0	5.4e+1
	10	15:11:00	41.5	282.1	0.60	4.46	1.79	0.93	7.2e-1	4.0e+1
	11	15:09:00	49.4	308.2	0.23	4.49	0.97	0.92	4.5e-1	3.1e+1
STEREO-A HET (e^-)	0	15:18:58	0.99	1.41	0.13	1.38	0.47	0.95	4.1e-1	2.3e+2
	1	15:19:58	1.98	2.44	0.11	0.92	0.43	0.96	1.0e-1	1.3e+2
	2	15:14:58	3.35	3.83	0.14	1.69	0.37	0.95	2.2e-1	5.5e+1
STEREO-A HET (p^+)	0	14:49:58	14.3	164.4	0.31	9.99	1.02	0.72	7.6e+0	2.1e+1
	1	14:58:58	16.0	174.0	0.30	9.99	0.89	0.78	1.0e+1	1.9e+1
	2	14:57:58	18.1	185.2	0.33	9.99	0.92	0.79	8.9e+0	1.6e+1
	3	14:56:58	22.2	205.3	0.37	9.99	0.93	0.83	7.5e+0	1.4e+1
	4	14:58:58	25.1	218.5	0.35	9.99	0.84	0.88	8.1e+0	1.1e+1
	5	14:56:58	27.9	230.5	0.34	8.29	0.93	0.91	2.5e+0	1.0e+1
	6	15:12:58	31.4	244.8	0.35	4.71	1.28	0.94	2.1e-1	9.2e+0
	7	15:08:58	34.6	257.2	0.35	5.68	1.02	0.93	4.7e-1	8.3e+0
	8	15:02:58	38.0	269.7	0.35	7.48	0.79	0.93	1.8e+0	7.0e+0
	9	14:54:58	49.0	307.2	0.36	9.97	0.55	0.92	1.6e+1	5.4e+0
	10	14:54:58	77.5	389.2	0.36	9.98	0.44	0.95	1.9e+1	2.8e+0

Table A.20: The fitting results for 28 October 2021.

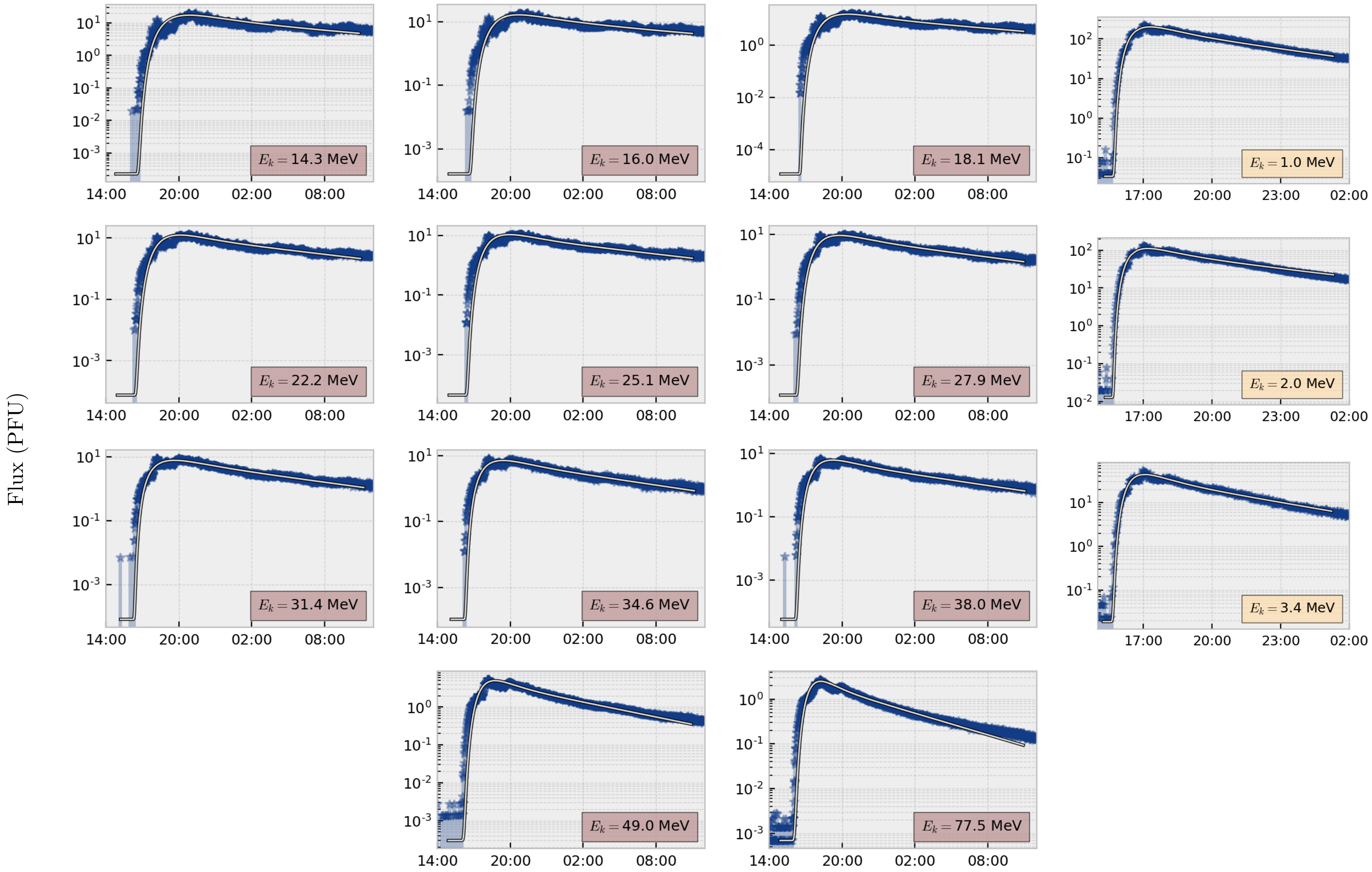

Figure A.13: The STEREO-A proton (left) and electron (right) results for 28 October 2021.

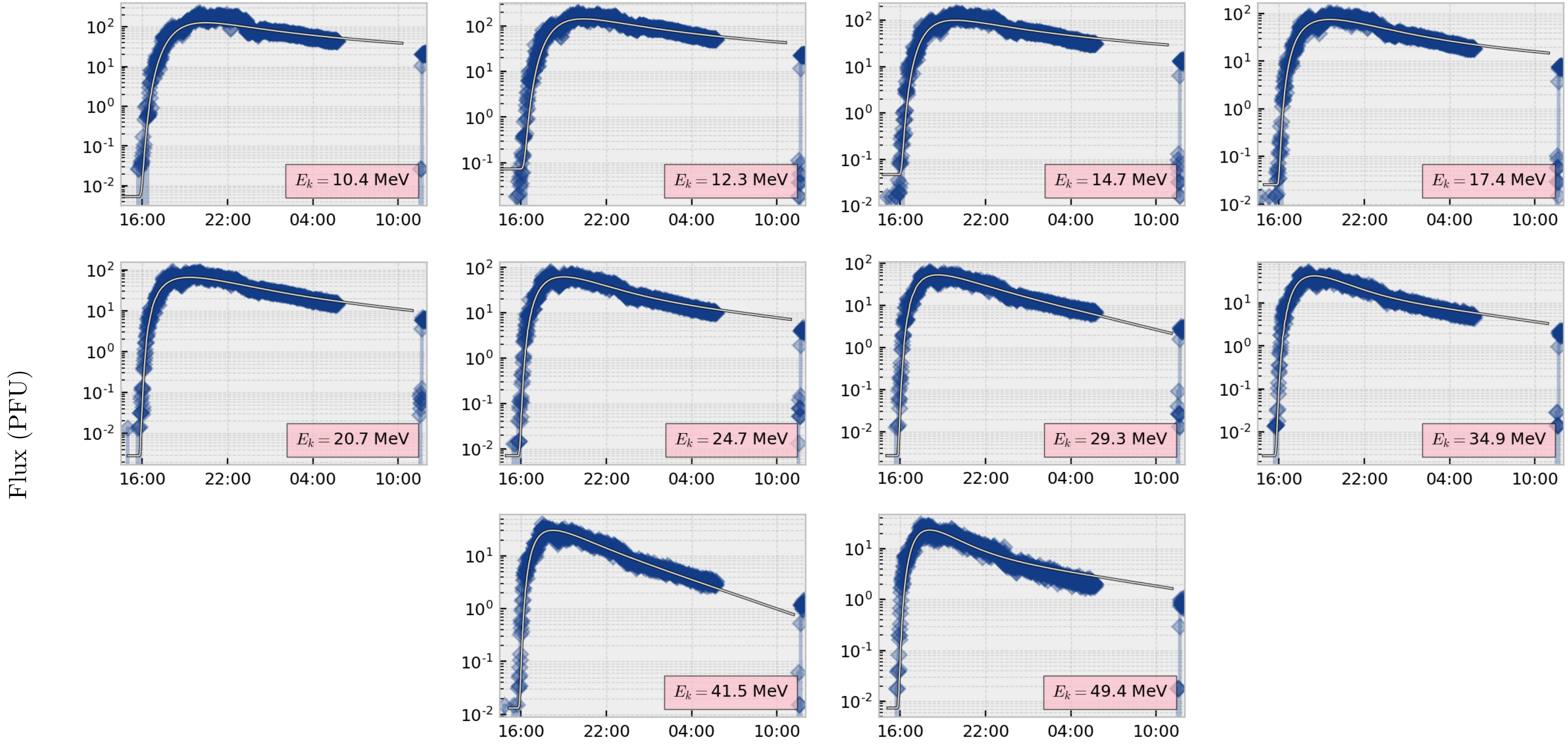

Figure A.14: The PSP proton results for 28 October 2021.

18 January 2022

18 January 2022 **11:58**		
Active region: 2929 Flare: B5.0 (323; 3)		
STEREO-A	0.966 AU	-25°
Earth	0.984 AU	10°
SOHO	0.976 AU	10°
PSP	0.739 AU	-151°
Solar Orbiter	0.933 AU	-9°

Table A.21: Event details drawn from Helioviewer and Solar-MACH.

Instrument	**Bin**	**Event Time**	E_k **(MeV)**	P **(MV)**	$\lambda_\parallel$ **(AU)**	τ_a **(hrs)**	τ_e **(hrs)**	R^2	**Norm.**	**Obs. Peak**
WIND 3DP (e^-)	0	17:33:30	0.03	0.17	0.50	0.90	0.10	-7.38	2.3e-8	1.6e-7
	1	17:09:30	0.04	0.21	0.11	0.90	0.40	0.97	9.5e-11	3.9e-8
	2	17:15:30	0.07	0.27	0.11	0.85	0.36	0.98	2.3e-11	1.1e-8
	3	17:12:30	0.11	0.35	0.13	1.90	0.40	0.99	1.8e-11	2.2e-9
	4	17:13:30	0.18	0.47	0.14	2.00	0.45	0.98	2.1e-12	3.2e-10
	5	01:57:30	0.31	0.64	0.50	0.90	0.10	-3.14	8.7e-12	1.1e-10
SolO EPT (e^-)	1	17:29:00	0.04	0.20	0.72	0.33	0.81	0.93	2.0e+2	2.4e+5
	4	17:28:00	0.05	0.22	0.59	0.40	0.58	0.95	1.3e+2	1.3e+5
	7	17:30:00	0.06	0.25	0.53	0.33	0.69	0.95	4.2e+1	6.4e+4
	10	17:29:00	0.07	0.28	0.49	0.48	0.50	0.96	3.6e+1	3.1e+4
	13	17:31:00	0.09	0.32	0.52	0.36	0.86	0.94	6.6e+0	1.2e+4
	16	17:31:00	0.12	0.36	0.51	0.53	0.65	0.94	4.5e+0	4.0e+3

Table A.22: The fitting results for 18 January 2022.

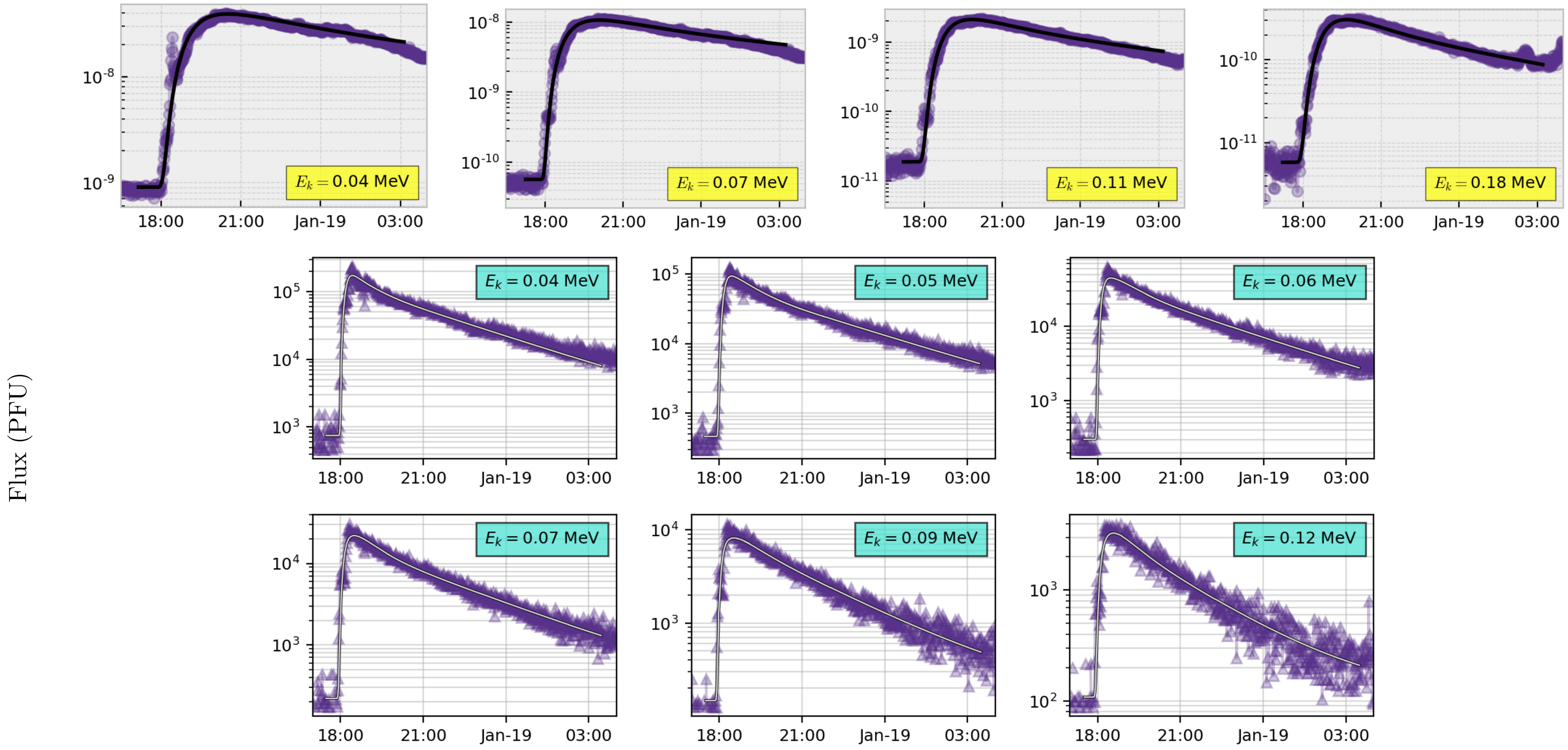

Figure A.15: The WIND electron (top) and Solar Orbiter electron (bottom) results for 18 January 2022.

20 January 2022

20 January 2022 **05:47**		
Active region: 2929 Flare: M5.5 (320; 12)		
STEREO-A	0.966 AU	-45°
Earth	0.984 AU	-10°
SOHO	0.976 AU	-10°
PSP	0.730 AU	-173°
Solar Orbiter	0.924 AU	-30°

Table A.23: Event details drawn from Helioviewer and Solar-MACH.

Instrument	**Bin**	**Event Time**	E_k **(MeV)**	P **(MV)**	$\lambda_\parallel$ **(AU)**	τ_a **(hrs)**	τ_e **(hrs)**	R^2	**Norm.**	**Obs. Peak**
SOHO HET (p^+)	0	05:18	14.5	165.6	0.46	7.00	1.53	0.92	1.1e-1	1.4e+0
	1	05:26	18.0	184.7	0.45	5.06	1.80	0.95	2.2e-2	8.9e-1
	2	05:27	22.5	206.7	0.45	4.45	2.02	0.97	6.5e-3	4.4e-1
	3	05:29	28.5	233.0	0.42	4.73	1.68	0.97	5.9e-3	3.0e-1
	4	05:20	36.0	262.4	0.36	7.15	0.98	0.97	3.0e-2	2.2e-1
	5	05:17	45.0	294.1	0.35	8.00	0.83	0.98	4.7e-2	1.6e-1
	6	05:20	57.0	332.0	0.37	7.00	0.85	0.98	1.9e-2	1.1e-1
	7	05:33	72.0	374.6	0.43	4.95	0.95	0.96	1.3e-3	2.7e-2
	8	05:13	90.0	420.7	0.51	9.99	0.66	0.91	6.4e-3	4.3e-3

Table A.24: The fitting results for 20 January 2022.

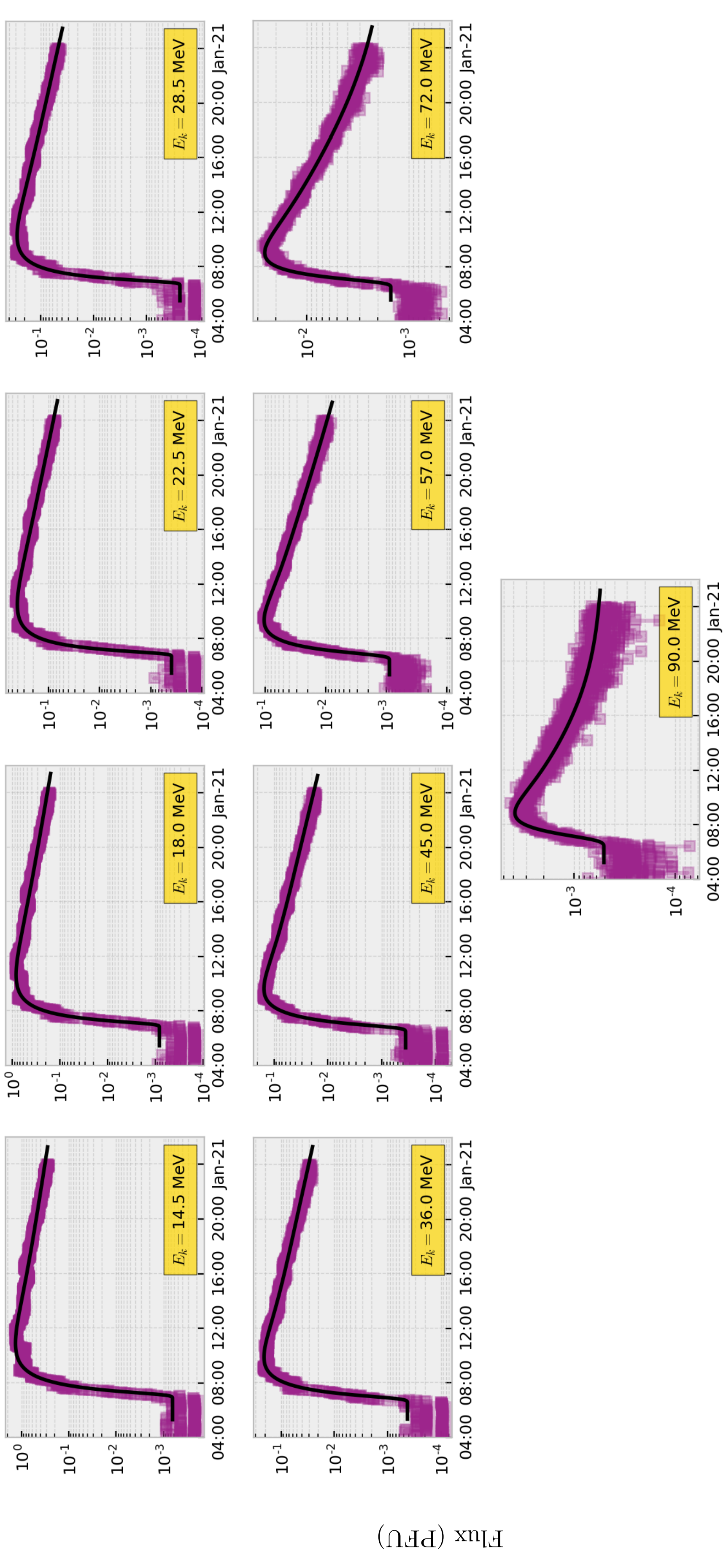

Figure A.16: The SOHO proton results for 20 January 2022

21 March 2022

21 March 2022 **05:32**		
Active region: 2974		
Flare: B4.2	(230; 16)	
STEREO-A	0.967 AU	-25°
Earth	0.996 AU	11°
SOHO	0.985 AU	10°
PSP	0.622 AU	117°
Solar Orbiter	0.342 AU	14°

Table A.25: Event details drawn from Helioviewer and Solar-MACH.

Instrument	**Bin**	**Event Time**	E_k **(MeV)**	P **(MV)**	$\lambda_\parallel$ **(AU)**	τ_a **(hrs)**	τ_e **(hrs)**	R^2	**Norm.**	**Obs. Peak**
SOHO HET (p^+)	0	06:07:30	14.5	165.6	0.37	1.83	2.20	0.62	5.6e-4	1.7e-1
	1	06:18:30	18.0	184.7	0.44	0.88	3.38	0.79	1.6e-4	1.1e-1
	2	06:25:30	22.5	206.7	0.65	0.81	4.80	0.89	9.5e-5	6.3e-2
	3	06:21:30	28.5	233.0	0.52	0.98	2.20	0.93	9.1e-5	4.9e-2
	4	05:46:30	36.0	262.4	0.55	3.55	1.05	0.95	1.1e-3	3.9e-2
	5	05:34:30	45.0	294.1	0.67	4.90	1.04	0.96	2.2e-3	3.1e-2
	6	05:08:30	57.0	332.0	0.66	6.00	1.03	0.94	2.3e-3	2.0e-2
WIND 3DP (e^-)	1	05:06:30	0.04	0.21	0.23	9.81	0.05	0.85	2.7e+0	5.5e-9
	2	05:38:30	0.07	0.27	0.27	0.07	1.28	0.84	1.8e-13	2.1e-9
	3	05:38:30	0.11	0.35	0.25	0.08	0.99	0.86	5.7e-14	6.6e-10
	4	05:38:30	0.18	0.47	0.26	0.14	0.77	0.84	2.5e-14	2.1e-10
	5	05:30:30	0.31	0.64	0.21	1.13	0.16	0.84	7.6e-13	5.1e-11
SolO EPT (e^-)	1	05:24:00	0.04	0.20	0.04	0.90	0.59	0.88	7.0e+0	4.0e+4
	4	05:15:00	0.05	0.22	0.02	1.80	0.15	0.91	3.1e+2	2.7e+4
	7	05:24:00	0.06	0.25	0.55	1.30	3.45	0.86	2.3e+1	1.6e+4
	10	05:27:00	0.07	0.28	0.15	0.94	1.61	0.86	3.0e+0	1.1e+4
	13	05:25:00	0.09	0.32	0.20	0.99	1.66	0.84	2.5e+0	5.6e+3
	16	05:29:00	0.12	0.36	0.06	0.40	1.50	0.81	1.3e-1	3.5e+3
	20	05:28:00	0.18	0.47	0.06	0.52	0.98	0.79	6.1e-2	1.0e+3

Table A.26: The fitting results for 21 March 2022.

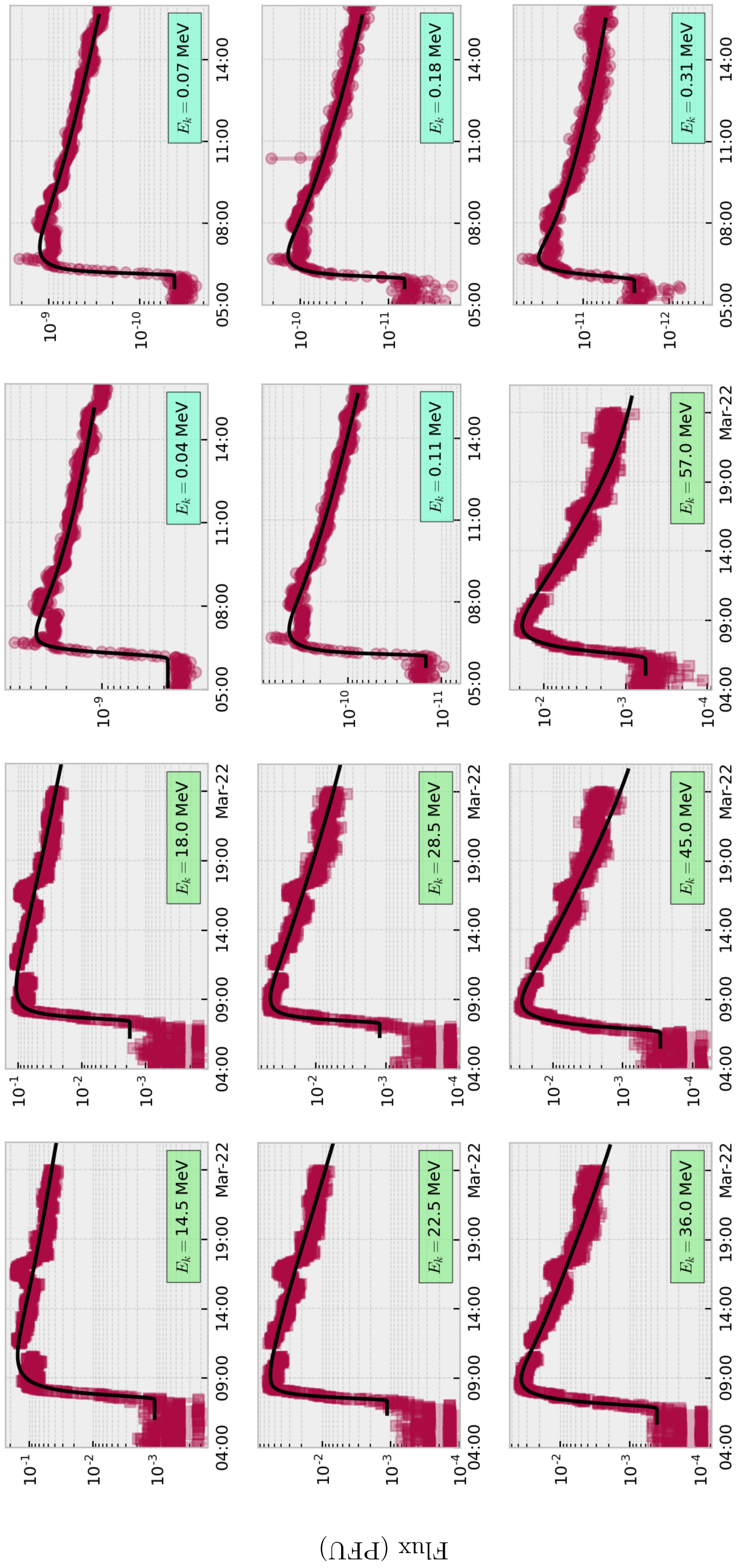

Figure A.17: The SOHO proton (left) and WIND electron (right) results for 21 March 2022.

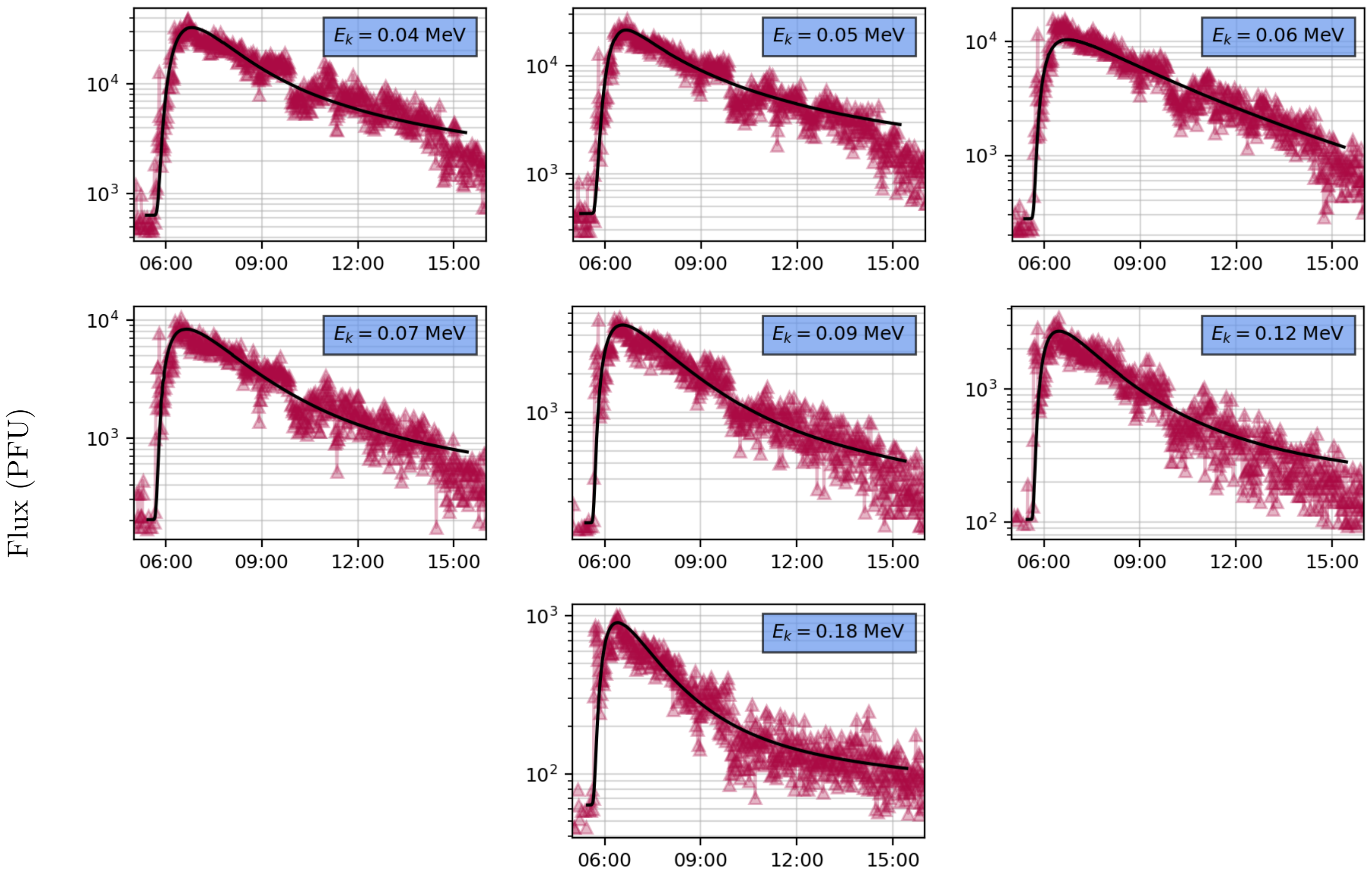

Figure A.18: The Solar Orbiter electron results for 21 March 2022.

2 April 2022

2 April 2022 **12:55**		
Active region: 2975 Flare: M4.3 (79; 11)		
STEREO-A	0.966 AU	-36°
Earth	1.000 AU	0°
SOHO	0.988 AU	-1°
PSP	0.727 AU	109°
Solar Orbiter	0.356 AU	69°

Table A.27: Event details drawn from Helioviewer and Solar-MACH.

Instrument	**Bin**	**Event Time**	E_k **(MeV)**	P **(MV)**	$\lambda_\parallel$ **(AU)**	τ_a **(hrs)**	τ_e **(hrs)**	R^2	**Norm.**	**Obs. Peak**
SOHO HET (p^+)	0	13:04:30	14.5	165.6	0.47	1.78	0.88	0.94	1.8e-2	1.7e+0
	1	13:05:30	18.0	184.7	0.51	2.47	0.70	0.97	3.6e-2	1.2e+0
	2	13:15:30	22.5	206.7	0.58	1.85	0.89	0.98	7.3e-3	6.3e-1
	3	13:13:30	28.5	233.0	0.60	2.45	0.74	0.98	1.1e-2	4.5e-1
	4	13:14:30	36.0	262.4	0.63	2.16	0.81	0.97	5.0e-3	2.9e-1
	5	13:21:30	45.0	294.1	0.67	1.15	1.13	0.97	7.8e-4	1.9e-1
	6	13:15:30	57.0	332.0	0.63	1.16	0.97	0.98	4.5e-4	1.0e-1
WIND 3DP (e^-)	0	13:02:30	0.03	0.17	0.50	0.55	0.45	0.97	7.5e-10	2.7e-7
	1	13:09:30	0.04	0.21	0.50	0.26	0.83	0.98	1.3e-10	2.1e-7
	2	13:17:30	0.07	0.27	0.51	0.10	1.49	0.96	1.8e-11	9.0e-8
	3	13:19:30	0.11	0.35	0.54	0.16	0.91	0.98	1.0e-11	3.2e-8
	4	13:21:30	0.18	0.47	0.48	0.16	0.61	0.98	3.6e-12	9.8e-9
	5	13:21:30	0.31	0.64	0.35	0.20	0.36	0.98	1.1e-12	2.5e-9
	6	13:19:30	0.52	0.89	0.18	0.94	0.04	0.39	1.1e-9	5.8e-10

Table A.28: The fitting results for 2 April 2022.

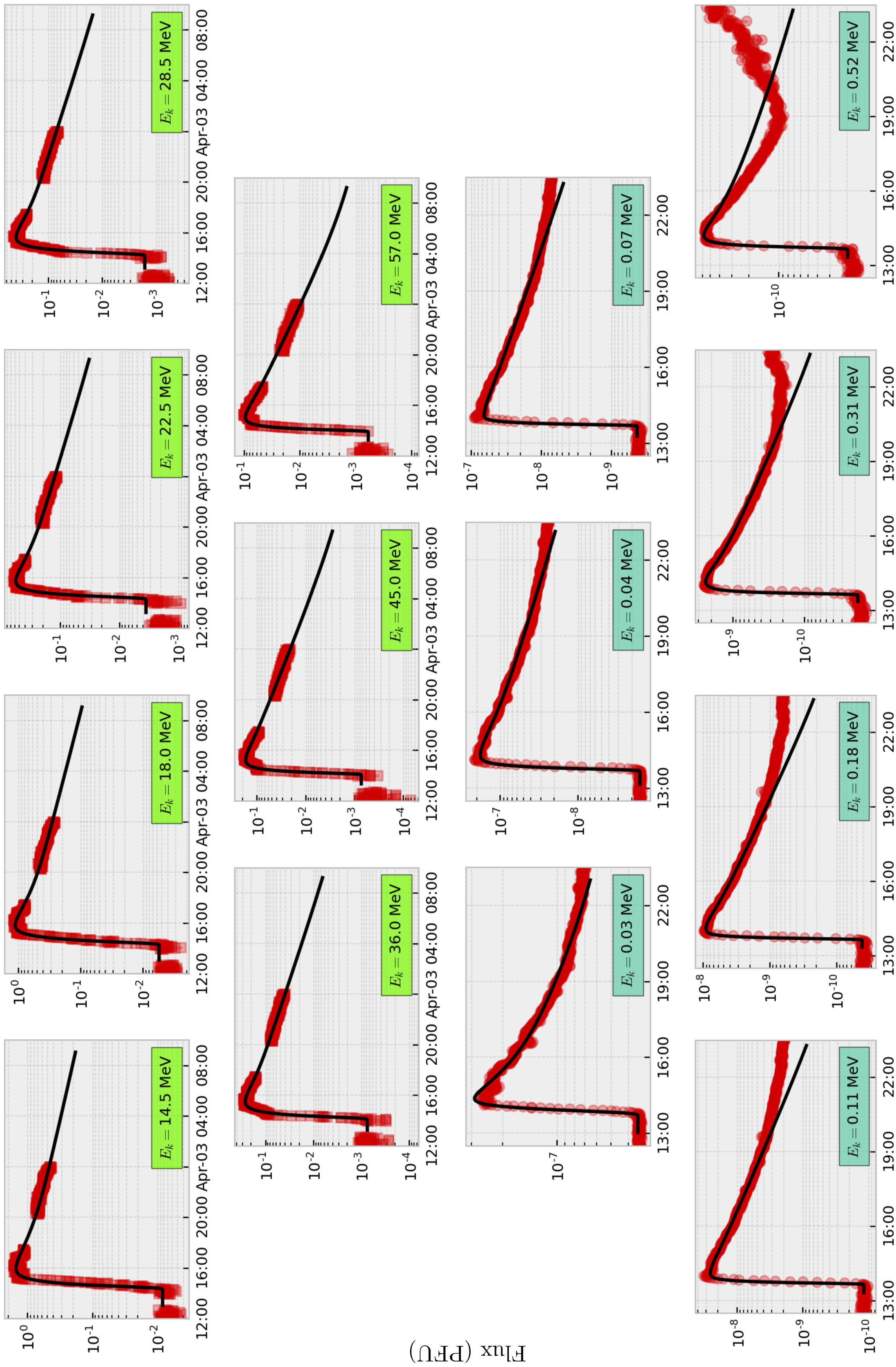

Figure A.19: The SOHO proton (top) and WIND electron (bottom) results for 2 April 2022.

Acknowledgements

I would like to acknowledge the assistance and support from the following people and institutions:

- My supervisor, Prof R. Du Toit Strauss, for his unwavering patience, immense support, and for introducing me to the life of research.
- The CSR for facilitating my inaugural research trip to our collaborators in Kiel, Germany and Athens, Greece, as well as my hosts for assisting us in our journey and providing us with their generous hospitality.
- Dr Nina Dresing and Dr Jan Gieseler for their assistance in gathering data and how to use the tools created by the SERPENTINE Project.
- Eleni Lavasa for the chaotic Skype discussions, motivation, and project 'gossip'.
- My language editor, Hettie Sieberhagen, for working late nights to help me finish.
- Mathew Holleran for his help in gathering as many resources as allowed to run simulations.
- The National Research Foundation (NRF) for financial support throughout my studies. This work is based on the research supported in part by the NRF of South Africa (Grant Number 142149). Opinions expressed and conclusions arrived at are those of the author and are not necessarily to be attributed to the NRF.
- My family and family-in-law for always driving me to succeed, but to also remember to relax from time to time.
- My friends in the CSR, including but not limited to Janie, Jonathan, Jeandre and Jabus. With special thanks to Jabus for the immeasurable sacrifices he has made to help me get here.

Jaclyn Tayla Stevens
Centre for Space Physics, North-West University

Bibliography

Achen, C. H. (1982). *Interpreting and Using Regression.* Quantitative Applications in the Social Sciences, No. 29. SAGE Publications, Inc.

Axford, W. I. (1965). Anisotropic diffusion of solar cosmic rays. *Planetary and Space Science*, 13(12):1301–1309.

Babcock, H. W. (1961). The topology of the Sun's magnetic field and the 22-year cycle. *The Astrophysical Journal*, 133:572.

Berry, W. D. and Feldman, S. (1985). *Multiple Regression in Practice.* Quantitative Applications in the Social Sciences. Sage Publications, Inc.

Bhatnagar, A. and Livingston, W. (2005). *Fundamentals of Solar Astronomy*, volume 6. World Scientific Publishing Co.

Bieber, J. W., Matthaeus, W. H., Smith, C. W., Wanner, W., Kallenrode, M. B., and Wibberenz, G. (1994). Proton and electron mean free paths: The Palmer Consensus revisited. *The Astrophysical Journal*, 420:294.

Bruno, R. and Carbone, V. (2016). *Turbulence in the Solar Wind*, volume 928. Springer.

Burlaga, L. F. (1967). Anisotropic diffusion of solar cosmic rays. *Journal of Geophysical Research*, 72:4449.

Chen, J. and Bieber, J. W. (1993). Cosmic-ray anisotropies and gradients in three dimensions. *The Astrophysical Journal*, 405:375.

Cravens, T. E. (2004). *Physics of Solar System Plasmas.* Cambridge.

Dresing, N., Effenberger, F., Gómez-Herrero, R., Heber, B., Klassen, A., Kollhoff, A., Richardson, I., and Theesen, S. (2020). Statistical results for solar energetic electron spectra observed over 12 yr with STEREO/SEPT. *The Astrophysical Journal*, 889(2):143.

Dröge, W. (1996). Energetic solar electron spectra and gamma-ray observations. In *High energy solar Physics*, volume 374 of *American Institute of Physics Conference Series*, pages 78–85.

Dröge, W. (2000). The rigidity dependence of solar particle scattering mean free paths. *The Astrophysical Journal*, 537(2):1073–1079.

Dröge, W. (2003). Solar particle transport in a dynamical quasi-linear theory. *The Astrophysical Journal*, 589(2):1027–1039.

Dröge, W., Ruffolo, D., and Khumlumlert, T. (1997). The rigidity dependence of solar electron mean free paths in the range 0.3 to 20 MV. In *International Cosmic Ray Conference*, volume 1 of *International Cosmic Ray Conference*, page 137.

Engelbrecht, N. E. (2008). *On the heliospheric diffusion tensor and its effect on 26-day recurrent cosmic-ray variations*. MSc thesis, North-West University.

Engelbrecht, N. E. and Burger, R. A. (2013). An ab initio model for the modulation of galactic cosmic-ray electrons. *The Astrophysical Journal*, 779(2):158.

Engelbrecht, N. E. and Moloto, K. D. (2021). An ab initio approach to antiproton modulation in the inner heliosphere. *The Astrophysical Journal*, 908(2):167.

Engelbrecht, N. E., Vogt, A., Herbst, K., Strauss, R. D., and Burger, R. A. (2022). Revisiting the revisited Palmer Consensus: New insights from jovian electron transport. *The Astrophysical Journal*, 929(1):8.

Forbush, S. E. (1946). Three unusual cosmic-ray increases possibly due to charged particles from the Sun. *Physical Review*, 70(9-10):771–772.

Fox, N. J., Velli, M. C., Bale, S. D., Decker, R., Driesman, A., Howard, R. A., Kasper, J. C., Kinnison, J., Kusterer, M., Lario, D., Lockwood, M. K., McComas, D. J., Raouafi, N. E., and Szabo, A. (2016). The Solar Probe Plus Mission: Humanity's first visit to our star. *Space Science Reviews*, 204(1-4):7–48.

Gieseler, J., Dresing, N., Palmroos, C., Freiherr von Forstner, J. L., Price, D. J., Vainio, R., Kouloumvakos, A., Rodríguez-García, L., Trotta, D., Génot, V., Masson, A., Roth, M., and Veronig, A. (2023). Solar-MACH: An open-source tool to analyze solar magnetic connection configurations. *Frontiers in Astronomy & Space Sciences*, 9.

Gurnett, D. A. and Bhattacharjee, A. (2017). *Introduction to Plasma Physics*. Cambridge.

Hanslmeier, A. (2002). *The NOAA Space Weather Scales*, chapter 2. Springer Netherlands.

Hasselmann, K. and Wibberenz, G. (1968). Scattering of charged particles by random electromagnetic fields. *Zeitschrift für Geophysik*, 34:353–388.

Hathaway, D. H. (2015). The solar cycle. *Living Reviews in Solar Physics*, 12(1):4.

Heita, P. K. N. (2019). *Numerical Investigation of Solar Energetic Particle Transport Between the Sun, Earth, and Mars*. MSc thesis, North-West University.

Howard, R. A., Moses, J. D., Vourlidas, A., Newmark, J. S., Socker, D. G., Plunkett, S. P., Korendyke, C. M., Cook, J. W., Hurley, A., Davila, J. M., Thompson, W. T., St Cyr, O. C., Mentzell, E., Mehalick, K., Lemen, J. R., Wuelser, J. P., Duncan, D. W., Tarbell, T. D., Wolfson, C. J., Moore, A., Harrison, R. A., Waltham, N. R., Lang, J., Davis, C. J., Eyles, C. J., Mapson-Menard, H., Simnett, G. M., Halain, J. P., Defise, J. M., Mazy, E., Rochus, P., Mercier, R., Ravet, M. F., Delmotte, F., Auchere, F., Delaboudiniere, J. P., Bothmer, V., Deutsch, W., Wang, D., Rich, N., Cooper, S., Stephens, V., Maahs, G., Baugh, R., McMullin, D., and Carter, T. (2008). Sun-Earth Connection Coronal and Heliospheric Investigation (SECCHI). *Space Science Reviews*, 136(1-4):67–115.

Hurlburt, N., Cheung, M., Schrijver, C., Chang, L., Freeland, S., Green, S., Heck, C., Jaffey, A., Kobashi, A., Schiff, D., Serafin, J., Seguin, R., Slater, G., Somani, A., and Timmons, R. (2012). Heliophysics event knowledgebase for the Solar Dynamics Observatory (SDO) and beyond. *Solar Physics*, 275(1-2):67–78.

Kaiser, M. L., Kucera, T. A., Davila, J. M., St. Cyr, O. C., Guhathakurta, M., and Christian, E. (2008). The STEREO mission: An introduction. *Space Science Reviews*, 136(1-4):5–16.

Kallenrode, M. B. (1995). Acceleration and propagation of energetic charged particles in the inner heliosphere. *Nuclear Physics B Proceedings Supplements*, 39:45–56.

Kaufmann, P., Holman, G. D., Su, Y., Gimenez de Castro, C. G., Correia, E., Fernandes, L. O. T., de Souza, R. V., Marun, A., and Pereyra, P. (2012). Unusual emissions at various energies prior to the impulsive phase of the large solar flare and coronal mass ejection of 4 November 2003. *Solar Physics*, 279(2):465–475.

Martucci, M., Laurenza, M., Benella, S., Berrilli, F., Del Moro, D., Giovannelli, L., Parmentier, A., Piersanti, M., Albrecht, G., Bartocci, S., Battiston, R., Burger, W. J., Campana, D., Carfora, L., Consolini, G., Conti, L., Contin, A., De Donato, C., De Santis, C., Follega, F. M., Iuppa, R., Lega, A., Marcelli, N., Masciantonio, G., Mergé, M., Mese, M., Oliva, A., Osteria, G., Palma, F., Panico, B., Perfetto, F., Picozza, P., Pozzato, M., Ricci, E., Ricci, M., Ricciarini, S. B., Sahnoun, Z., Scotti, V., Sotgiu, A., Sparvoli, R., Vitale, V., Zoffoli, S., and Zuccon, P. (2023). The first ground-level enhancement of solar cycle 25 as seen by the High-Energy Particle Detector (HEPD-01) on board the CSES-01 satellite. *Space Weather*, 21.

McComas, D. J., Bame, S. J., Barraclough, B. L., Feldman, W. C., Funsten, H. O., Gosling, J. T., Riley, P., Skoug, R., Balogh, A., Forsyth, R., Goldstein, B. E., and Neugebauer, M. (1998). Ulysses' return to the slow solar wind. *Geophysical Research Letters*, 25(1):1–4.

Mishev, A. L., Kocharov, L. G., Koldobskiy, S. A., Larsen, N., Riihonen, E., Vainio, R., and Usoskin, I. G. (2022). High-resolution spectral and anisotropy characteristics of solar protons during the GLE N°73 on 28 October 2021 derived with neutron-monitor data analysis. *Solar Physics*, 297(7):88.

Moloto, K. D. and Engelbrecht, N. E. (2020). A fully time-dependent ab initio cosmic-ray modulation model applied to historical cosmic-ray modulation. *The Astrophysical Journal*, 894(2):121.

Moraal, H. (2013). Cosmic-ray modulation equations. *Space Science Reviews*, 176(1-4):299–319.

Mosotho, M. G., Strauss, R. D., Nndanganeni, R. R., and van den Berg, J. P. (2021). The North-West University's high altitude radiation monitor programme. *South African Journal of Science*, 117(1/2).

Müller, D., Fleck, B., Dimitoglou, G., Caplins, B. W., Amadigwe, D. E., García Ortiz, J. P., Wamsler, B., Alexanderian, A., Hughitt, V. K., and Ireland, J. (2009). Jhelioviewer: Visualizing large sets of solar images using JPEG 2000. *Computing in Science and Engineering*, 11(5):38–47.

Müller, D., Nicula, B., Felix, S., Verstringe, F., Bourgoignie, B., Csillaghy, A., Berghmans, D., Jiggens, P., García-Ortiz, J. P., Ireland, J., Zahniy, S., and Fleck, B. (2017). Jhelioviewer: Time-dependent 3d visualisation of solar and heliospheric data. *Astronomy & Astrophysics*, 606:A10.

Palmer, I. D. (1982). Transport coefficients of low-energy cosmic rays in interplanetary space. *Reviews of Geophysics and Space Physics*, 20:335–351.

Papaioannou, A., Kouloumvakos, A., Mishev, A., Vainio, R., Usoskin, I., Herbst, K., Rouillard, A. P., Anastasiadis, A., Gieseler, J., Wimmer-Schweingruber, R., and Kühl, P. (2022). The first ground-level enhancement of solar cycle 25 on 28 October 2021. *Astronomy & Astrophysics*, 660:L5.

Parker, E. N. (1958a). Dynamics of the interplanetary gas and magnetic fields. *The Astrophysical Journal*, 128:664.

Parker, E. N. (1958b). On the variations of the primary cosmic ray intensity. In *Electromagnetic Phenomena in Cosmical Physics*, volume 6, page 420.

Pedregosa, F., Varoquaux, G., Gramfort, A., Michel, V., Thirion, B., Grisel, O., Blondel, M., Prettenhofer, P., Weiss, R., Dubourg, V., Vanderplas, J., Passos, A., Cournapeau, D., Brucher, M., Perrot, M., and Duchesnay, E. (2011). Scikit-learn: Machine learning in Python. *Journal of Machine Learning Research*, 12:2825–2830.

Pesnell, W. D., Thompson, B. J., and Chamberlin, P. C. (2012). The Solar Dynamics Observatory (SDO). *Solar Physics*, 275(1-2):3–15.

Prinsloo, P. (2016). *Acceleration of cosmic rays in the outer heliosphere.* MSc thesis, North-West University.

Reames, D. V. (1999). Particle acceleration at the Sun and in the heliosphere. *Space Science Reviews*, 90:413–491.

Reid, G. C. (1964). A diffusive model for the initial phase of a solar proton event. *Journal for Geophysical Resources*, 69(13):2659–2667.

Roelof, E. C. (1969). *Propagation of Solar Cosmic Rays in the Interplanetary Magnetic Field.* NASA Goddard Space Flight Center.

Roelof, E. C. (2015). Charged particle energization and transport in reservoirs throughout the heliosphere: 1. Solar energetic particles. In *Journal of Physics*, volume 642 of *Conference Series*.

Ruffolo, D. (1995). Effect of adiabatic deceleration on the focused transport of solar cosmic rays. *The Astrophysical Journal*, 442:861.

Sakurai, K. (1974). Energetic particles from the Sun. *Astrophysics and Space Science*, 28(2):375–519.

Steinacker, J., Dröge, W., and Schlickeiser, R. (1988). Particle acceleration in impulsive solar flares: Part one. *Solar Physics*, 115(2):313–326.

Steyn, P. (2022). *A multi-wavelength approach to solar energetic particle transport using remote sensing and in-situ observations.* PhD thesis, North-West University.

Strauss, R. D. (2013). *Modelling of cosmic ray modulation in the heliosphere by stochastic processes.* PhD thesis, North-West University.

Strauss, R. D., Dresing, N., Kollhoff, A., and Brüdern, M. (2020). On the shape of SEP electron spectra: The role of interplanetary transport. *The Astrophysical Journal*, 897(1):24.

Strauss, R. D., van den Berg, J. P., and Rankin, J. S. (2022). Cosmic-ray transport near the Sun. *The Astrophysical Journal*, 928(1):22.

Teufel, A. and Schlickeiser, R. (2002). Analytic calculation of the parallel mean free path of heliospheric cosmic rays. I. Dynamical magnetic slab turbulence and random sweeping slab turbulence. *Astronomy & Astrophysics*, 393:703–715.

Teufel, A. and Schlickeiser, R. (2003). Analytic calculation of the parallel mean free path of heliospheric cosmic rays. II. Dynamical magnetic slab turbulence and random sweeping slab turbulence with finite wave power at small wavenumbers. *Astronomy & Astrophysics*, 397:15–25.

The SunPy Community, Barnes, W. T., Bobra, M. G., Christe, S. D., Freij, N., Hayes, L. A., Ireland, J., Mumford, S., Perez-Suarez, D., Ryan, D. F., Shih, A. Y., Chanda, P., Glogowski, K., Hewett, R., Hughitt, V. K., Hill, A., Hiware, K., Inglis, A., Kirk, M. S. F., Konge, S., Mason, J. P., Maloney, S. A., Murray, S. A., Panda, A., Park, J., Pereira, T. M. D., Reardon, K., Savage, S., Sipőcz, B. M., Stansby, D., Jain, Y., Taylor, G., Yadav, T., Rajul, and Dang, T. K. (2020). The SunPy Project: Open source development and status of the version 1.0 core package. *The Astrophysical Journal*, 890:68.

Thompson, W. T. (2005). Coordinate systems for solar image data. *Astronomy & Astrophysics*, 449(2):791–803.

Ursi, A., Parmiggiani, N., Messerotti, M., Pellizzoni, A., Pittori, C., Longo, F., Verrecchia, F., Argan, A., Bulgarelli, A., Tavani, M., Tempesta, P., and D'Amico, F. (2023). The first AGILE solar flare catalog. *The Astrophysical Journal Supplement Series*, 267(1):9.

Vainio, R., Raukunen, O., Tylka, A. J., Dietrich, W. F., and Afanasiev, A. (2017). Why is solar cycle 24 an inefficient producer of high-energy particle events? *Astronomy & Astrophysics*, 604:A47.

van den Berg, J. P., Strauss, R. D., and Effenberger, F. (2020). A primer on focused solar energetic particle transport. *Space Science Reviews*, 216(8):146.

Van Rossum, G. (2020). *The Python Library Reference, release 3.8.2.* Python Software Foundation.

Virtanen, P., Gommers, R., Oliphant, T. E., Haberland, M., Reddy, T., Cournapeau, D., Burovski, E., Peterson, P., Weckesser, W., Bright, J., van der Walt, S. J., Brett, M., Wilson, J., Millman, K. J., Mayorov, N., Nelson, A. R. J., Jones, E., Kern, R., Larson, E., Carey, C. J., Polat, İ., Feng, Y., Moore, E. W., VanderPlas, J., Laxalde, D., Perktold, J., Cimrman, R., Henriksen, I., Quintero, E. A., Harris, C. R., Archibald, A. M., Ribeiro, A. H., Pedregosa, F., van Mulbregt, P., and SciPy 1.0 Contributors (2020). SciPy 1.0: Fundamental algorithms for scientific computing in python. *Nature Methods*, 17:261–272.

Wolmarans, C. (2021). *An ab initio approach to the historical modulation of cosmic rays.* MSc thesis, North-West University.

Wright, S. (1921). Correlation and causation. *Journal of Agricultural Research*, 20(7):562.